Study on lithium ion migration in the composite solid electrolyte for lithium metal batteries

Zur Erlangung des akademischen Grades eines

DOKTORS DER NATURWISSENSCHAFTEN

(Dr. rer. nat.)

der Fakultät für Chemie und Biowissenschaften

des Karlsruher Instituts für Technologie (KIT)

genehmigte

DISSERTATION

von

Master-Material Science and Engineering

Guiying Tian

aus

Tangshan (China)

KIT-Dekan: Prof. Dr. Reinhard Fischer

Referent: Prof. Dr. Helmut Ehrenberg

Korreferent: Prof. Dr. Stefano Passerini

Tag der mündlichen Prüfung: 11.12.2018

Abstract

Recently, the shortage of fossil sources, in particular crude oil, as well as environmental pollution generated by their combustion, inevitably increased a huge demand for renewable energy sources and storage systems. As a core component of mobile devices and electric vehicles, secondary batteries are expected not only to be low cost and safe, but also to possess excellent electrochemical properties including: high energy/power density and long cyclic stability. Although, in the long term, novel batteries, *e.g.*, lithium-sulfur and lithium-air, seem to be promising candidates due to their superior specific capacity, lithium-ion/metal batteries are, and will, still be considered the main energy storage device for the next decade. Currently, commercial lithium-ion batteries using liquid electrolytes (*e.g.*, LP30 (1 M $LiPF_6$ dissolved in EC/DMC 1:1 by volume) with high ionic conductivity (~10 mS cm^{-1}) at room temperature, exhibit a moderate capacity (150 Ah kg^{-1} or 250Wh kg^{-1}). However, such capacity still cannot satisfy the request for long range of electric vehicles. Severe crash and overcharge can trigger exothermic reaction and short circuit accompanied by a serious explosion. Moreover, the toxicity and leakage problems of liquid electrolytes also limit their further possibility of development in the future.

Given safety issues of the liquid electrolyte based batteries, interest in all solid state battery is rapidly increasing. The high mechanical strength of the solid electrolyte can suppress the dendrite penetration. Therefore, metallic lithium can be applied for the anode, which is favorable for high volumetric capacity. Building solid state batteries with focus of high performance of the solid electrolytes is significant. The ideal solid electrolyte is desired to display high ionic conductivity, high electrochemical and chemical stability as well as a wide electrochemical stability window. According to their main component (sulfur, oxygen and carbon), solid electrolytes are categorized into three types, the sulfide-, oxide- and polymer- electrolyte. Although showing high ionic conductivities, toxic sulfide-type solid electrolytes are highly reactive towards electrodes and moisture. Thus, electrode- and electrolyte degradation occurs, as well as resistive interphase formation. In contrast, oxide- and polymer solid electrolytes display remarkable electrochemical stability against electrodes and chemical stability on air. Thus, the research should be concentrate on oxide- and polymer solid electrolyte with acceptable ionic conductivity and compatible electrolyte/electrode interface. Therefore, this thesis focuses mainly on lithium metal batteries using solid electrolytes and lithium anode. It aims to discover not only the suitable combinations

between electrode and electrolyte, but also assembly methods for safe batteries. In this thesis, the experimental discussion contains three sections: Firstly, the garnet oxide /polyethylene oxide composite solid electrolyte. Secondly, Li^+ salt integrated crosslinking polymer/garnet oxide composite solid electrolyte and lastly, Fe-stabilized garnet/polymer hybrid solid electrolyte. Given high ionic conductivity, moderate rate capability and high cycling stability, these solid electrolytes exhibit a promising potential for practical application with improved safety in contrast to conventional lithium-ion batteries.

Zusammenfassung

In jüngster Vergangenheit ist die Nachfrage nach erneuerbaren Energiequellen enorm angestiegen. Grund dafür ist zum einen der Mangel an fossilen Brennstoffen, insbesondere Erdöl, zum anderen der voranschreitende Klimawandel, der Großteils durch die Verbrennung dieser fossilen Brennstoffe und durch die einhergehende Umweltverschmutzung verursacht wird. Folglich wird vermehrt im mobilen Anwendungsbereich, beispielsweise bei Elektrogeräten und -fahrzeugen, auf Nachhaltigkeit gesetzt. Es wird von den dort verwendeten Sekundärbatterien erwartet, dass sie nicht nur kostengünstig sind, sondern auch hervorragende elektrochemische Eigenschaften aufweisen, wie eine hohe Energie bzw. Leistungsdichte und eine lange Zyklenstabilität. Aktuelle Forschungen an Lithium-Schwefel- und Lithium-Luft-Batterien weisen zwar eine herausragende spezifische Kapazität auf, diese sind allerdings noch nicht auf dem Entwicklungsstand für die großtechnische Produktion im industriellen Maßstab angelangt. „State of the art“ sind momentan Lithium-Ionen und Metall-Batterien, die womöglich noch die nächsten Jahrzehnte am häufigsten zum Einsatz kommen werden. Gegenwärtig weisen kommerzielle Lithiumionenbatterien, die flüssige Elektrolyte beinhalten (z. B. LP30: 1 M $LiPF_6$, gelöst in EC/DMC 1:1 Volumenanteil), eine hohe Ionenleitfähigkeit (~10 mS cm^{-1}) bei Raumtemperatur und eine mäßige Kapazität (150 Ah kg^{-1} oder 250Wh kg^{-1}) auf. Dieser Kapazitätsbereich kann beispielsweise kaum die Anforderungen langer Reichweiten bei Elektrofahrzeugen erfüllen. Zudem kann eine starke Beschädigung, die etwa durch einen Autounfall verursacht wird, oder aufgrund einer Überladung der Batterie, zu exothermen Reaktionen führen und dadurch einen Kurzschluss verursachen. Dies kann im schlimmsten Fall zu schwerwiegende Explosion führen. Zudem sind die Fortschritte in diesem Gebiet wegen der Toxizität des Elektrolyts und der Gefahr, die durch das Auslaufen des Elektrolyts besteht, stark limitiert.

Angesichts dieser Sicherheitsbedenken bei Batterien auf der Basis von Flüssigelektrolyten nimmt das Interesse an allen Festkörperbatterien rasch zu. Aufgrund der hohen mechanischen Festigkeit des Feststoffelektrolyts kann die Dendritenpenetration reduziert werden. Dadurch kann metallisches Lithium für die Anode verwendet werden, was für Festkörperbatterien mit hohen Kapazitäten von großer Bedeutung ist. Der ideale Festelektrolyt soll eine hohe Ionenleitfähigkeit, eine hohe elektrochemische und chemische Stabilität, sowie ein breites elektrochemisches Fenster aufweisen. Gemäß ihren Hauptbestandteilen (Schwefel, Sauerstoff und Kohlenstoff) werden

Feststoffelektrolyte in drei Kategorien unterteilt: Sulfid-, Oxid- und Polymer-Typ. Obwohl die toxischen Sulfid-Feststoffelektrolyten hohe Ionenleitfähigkeiten zeigen, reagieren diese leicht mit den Elektroden und sind nicht feuchtigkeitsbeständig. Dadurch degradieren Elektroden und Elektrolyt leicht, wodurch hochohmsche Zwischenphasen gebildet werden. Im Gegensatz dazu zeigen oxidische und polymere Feststoffelektrolyte eine bemerkenswerte elektrochemische Stabilität gegenüber Elektroden und weisen chemische Stabilität an Luft auf. Deshalb sollte sich die Batterieforschung hauptsächlich auf Oxid-Feststoffelektrolyten und Polymer-Feststoffelektrolyten mit hoher ionischer Leitfähigkeit und kompatiblen Elektrolyt-Elektroden-Zwischenphase konzentrieren. Dementsprechend fokussiert sich diese Arbeit auf Lithium-Metall-Batterien mit Feststoffelektrolyten und Lithium-Anoden. Das Ziel ist es dabei, nicht nur die geeignete Zusammensetzung zwischen Elektrode und Elektrolyt zu untersuchen, sondern auch ein Montageverfahren für sichere Batterien zu entwickeln. Diese Thesis wird dabei in drei Abschnitte untergliedert: Der erste Teil behandelt Granatoxid/Polyethylenoxid-Verbundfeststoffelektrolyt. Der nächste befasst sich mit vernetztem Polymer/Granatoxid-Verbundfeststoffelektrolyt mit integriertem Li^+ Salz und der dritte mit einem Eisen-stabilisierten Granat/Polymer-Hybrid-Feststoffelektrolyt. Angesichts hoher Ionenleitfähigkeit, moderater Belastungsfähigkeit und hoher Zyklenstabilität zeigen diese Feststoffelektrolyte ein hohes Entwicklungspotential für praktische Anwendungen mit einer verbesserten Sicherheit gegenüber konventionellen Lithium-Ionen-Batterien.

Ich versichere hiermit, dass ich die vorliegende Dissertation selbständig und ohne unzulässige fremde Hilfe erbracht habe. Ich habe keine anderen als die angegeben Quellen und Hilfsmittel benutzt, sowie wörtliche und sinngemäße Zitate kenntlich gemacht. Die Dissertation wurde bisher an keiner anderen Hochschule oder Universität eingereicht.

Karlsruhe, 21.01.2019 Guiying Tian.

Ort,Datum Unterschrift

Content

Chapter 1 Introduction 1

Chapter 2 Fundamentals 5

2.1 Basic structure of cells 5

2.2 Thermodynamics and kinetics 8

2.3 Solid electrolytes for lithium metal batteries 9

2.3.1 Sulfide-type solid electrolytes 11

2.3.1.1 Glassy sulfide-type solid electrolytes 12

2.3.1.2 Crystalline sulfide-type solid electrolytes 13

2.3.1.3 Drawbacks of sulfide-type solid electrolytes 14

2.3.2 Oxide-type solid electrolytes 14

2.3.2.1 LISICON-type solid electrolytes 15

2.3.2.2 NASICON-type solid electrolytes 16

2.3.2.3 Perovskite-type solid electrolytes 16

2.3.2.4 Garnet-type solid electrolytes 17

2.3.3 Polymer-based solid electrolytes 17

2.4 Limitations of the solid electrolytes 19

2.5 Content of the thesis 22

Chapter 3 Experimental method 24

3.1 scanning electron microscope 24

3.2 X-ray powder diffraction 25

3.3 Pair distribution function 25

3.3 Fourier-transform infrared spectroscopy 27

3.4 Cyclic voltammetry 27

3.5 Electrochemical impedance spectroscopy 28

3.6 Galvanostatic cycling 28

3.7 Nuclear magnetic resonance 29

Chapter 4 Garnet-polymer composite solid electrolyte 30

4.1 Introduction 30

4.2 Experimental section 31

4.2.1 Preparation of the LLZ/PEO CSE film 31

4.2.2 Preparation of the $LiNi_{1/3}Co_{1/3}Mn_{1/3}O_2$ cathode 31

4.2.3 Electrochemical evaluation of the CSE film 32

4.2.4 General characterization 32

4.3 Results and discussion 33

4.3.1 The relation of wt.% *vs.* vol.% 33

4.3.2 Ionic migration 35

4.3.2.1 Li^+ concentration 37

4.3.2.2 Li^+ mobility 38

4.3.2.3 Li^+ pathway 40

4.3.3 Electrochemical performance 41

4.4 Conclusions 45

4.5 Supporting information 46

Chapter 5 Crosslinked polyglycol-garnet composite solid electrolyte 51

5.1 Introduction 51

5.2 Experimental 52

5.2.1 Preparation of composite solid electrolyte film 52

5.2.2 General characterization 52

5.2.3 Electrochemical evaluation 53

5.2.4 Battery tests 53

5.3 Results and discussion 54

5.3.1 Crosslinking preparation 54

5.3.2 Ionic conductivity 57

5.3.3 Electrochemical performance 59

5.3.4 Battery performance 62

5.4 Conclusions 65

5.5 Supporting information 66

Chapter 6 Fe stabilized $Li_7La_3Zr_2O_{12}$ solid electrolytes 68

6.1 Introduction 68

6.2 Experimental methods 69

6.2.1 Synthesis of Fe doping LLZ 69

6.2.2 Crystal characterization 70

6.2.3 General characterization 70

6.2.4 Battery tests 71

6.3 Results and discussion 71

6.3.1 Initial sintering analysis 71

6.3.2 Re-sintering analysis 75

6.3.3 Ionic conductivity 78

6.3.4 Battery performance 80

6.4 Conclusions 84

6.5 Supporting Information 85

References 90

Acknowledgments 110

Chapter 1 Introduction

Since the initial commercialization of Li ion batteries (LIBs, *e.g.*, $LiCoO_2$||carbon) by Sony Energytec Inc. in June 1991, the demand for LIBs has been sustainably increasing due to the flourishing market of laptops, cellphones, cameras and especially electric vehicles (EVs) [1–4]. For instance, because of some serious global problems caused by fuel vehicles, such as: global warming (CO_2 emission), air pollution (NO_x emission), resource exhaustion (oil consumption) and geological damage (landslide), automobile electrolysis has already become a common view [5]. On the other hand, as a result of the improvement in standard of living, tens of millions of cars are sold every year, making the automotive industry a fundamental economic sector. Considering the environmental issues and economic growth, vehicle electrification is an acceptable solution; which puts automakers under pressure [6,7]. Figure 1.1 displays a clear roadmap of the electrification of powertrains of German car manufacturers based on the glorious future of the EVs [8,9]. The sales of EVs were growing at a compound annual growth rate of ~50% from 2010 to 2016 [10]. As displayed in Figure 1.2, it is predictable that the EV sales will exceed fuel cars sales in 2040 with this steady increase. Some governments have proposed the deadline for the sale of fuel vehicles, *e.g.*, Norway (2025), Holland (2025), India (2030), California (2030), Germany (2040), France (2040), China (2040), Great Britain (2040) and Japan (2050). These deadlines are not legally enforced, but they imply the basic developing attitude and industrial ambition. In fact, the giant auto and novel automakers start to hold the technical patents and markets. With the technical development: sunlight, wind, tides, geothermal heat, biomass and nuclear power can be exploited as renewable energies for EVs. To make the best use of these sustainable energies, high efficiency and low-cost energy storage systems are crucial and mandatory. Although great achievements were obtained in the past two decades, only ~1% of the energy consumed worldwide was stored [11]. In order to satisfy the energy storage and supply for the EVs, more attention should be paid to the research on rechargeable batteries.

Nowadays, the LIBs (for BEV) and fuel cells (for PHEV) are the main energy storage devices in the EVs. As for fuel cells, they convert the chemical energy of hydrogen/methanol and oxygen directly into electrical energy through an electrochemical reaction, which exhibits high conversion efficiency (95%) and low CO_2 emission. However, it should be associated with an external circuit and power electronic interfacing to provide a stable power output. The low nominal voltage, high

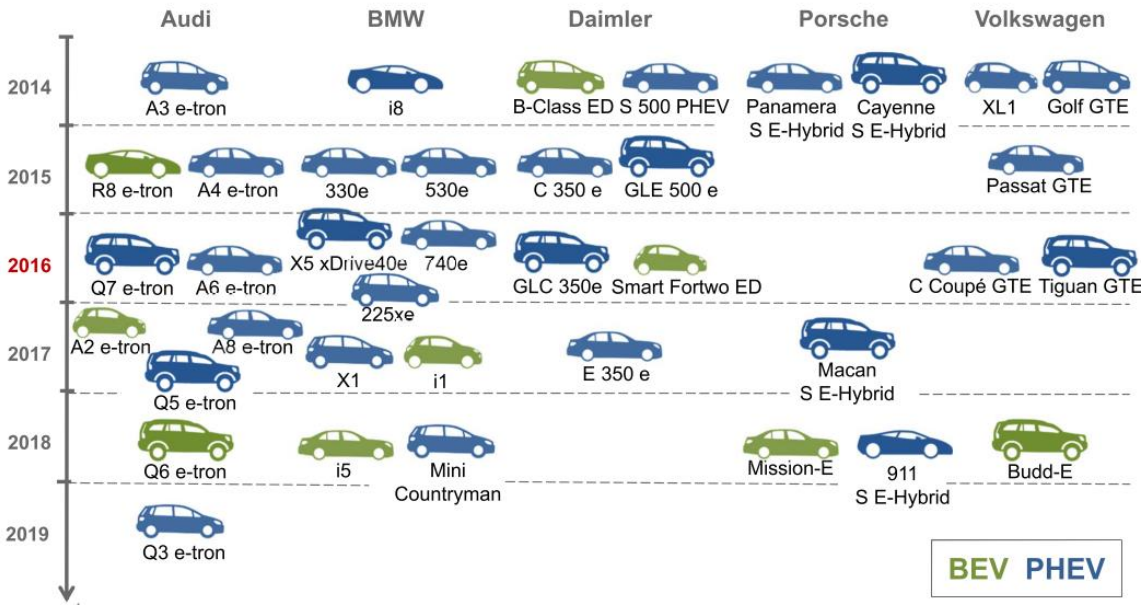

Figure 1.1. The trend in the electrification of powertrains for Germany automakers. Data from Prof. Friedrich, Horst: 2016 international conference on advanced automotive technology.

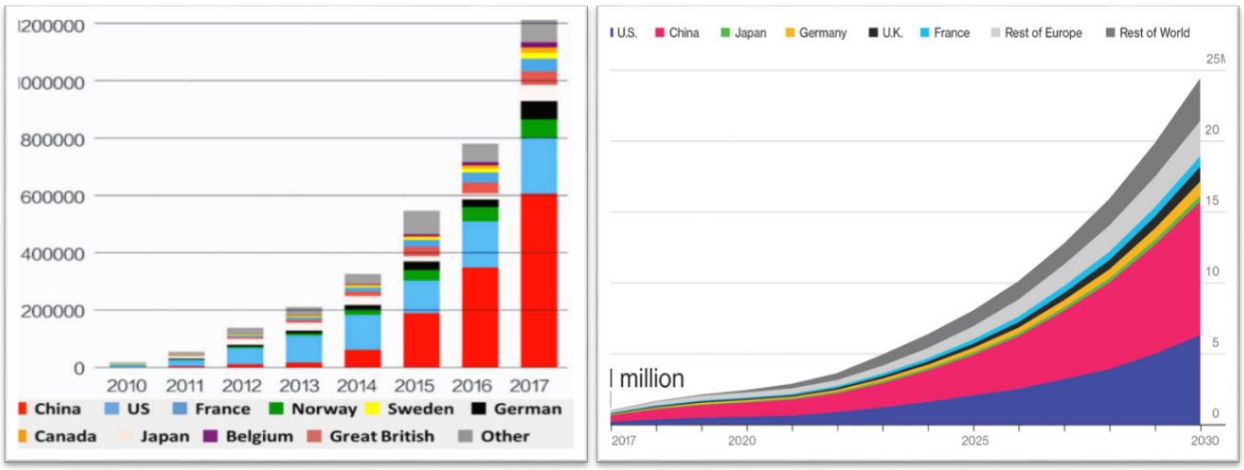

Figure 1.2. The annual EV sales in the world from 2010 to 2017, and predicted sales from 2017 to 2030. Data from EV-volume and Bloomberg New Energy Finance.

current ripple, large occupied volume, expensive catalyst and high working temperature have limited further application of fuel cells [12–14]. Long-term interdisciplinary research is required to achieve economical fuel cells. Therefore, the following review is mainly focused on historical and current achievements of LIBs, lithium metal batteries (LMBs), solid electrolytes (SEs) and related (all) solid state battery (SSBs).

Figure 1.3 displays the roadmap of commercial batteries towards to LMBs. As the lightest metal, metallic lithium as anode has the highest specific capacity (3860 mAh g^{-1} or 2061 mAh cm^{-3}) and lowest electrochemical potential (-3.04 V *vs.* standard hydrogen electrode (SHE)). In 1912, G.N.

Lewis began pioneering work with lithium batteries, and then the first disposable LMB became commercially available by the early 1970s. Attempts to apply rechargeable LMBs failed because of the inherent instability of lithium metal and its dendrite growth during charge/discharge processes. As a result, the research had to switch to LIBs in the 1980s, which later became commercial in 1991. Despite lower energy density (if compared with LMBs), LIBs display typically double capacity of the nickel-cadmium batteries. Additionally, LIBs equipped with safe precautions require low-cost maintenance due to their slight self-discharge, no lithium memory as well as tiny harm during post-decommission disposal. Since the 1990s the market scale of the LIBs grew from 2 GWh in 2000 to 134 GWh in 2017, while the price obviously dropped from 600 JPY Wh^{-1} in 2001 to 25 JPY Wh^{-1} in 2017. Although the novel batteries like lithium-air and lithium-sulfur have been ceaselessly proposed, the LIBs are still considered to be the main commercial batteries for the next decade (see Figure 1.4) [9,15].

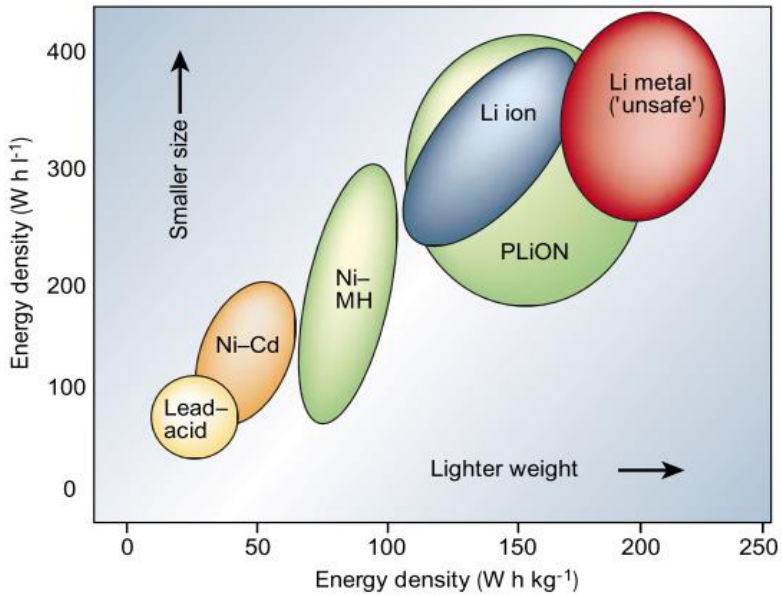

Figure 1.3. The different types of batteries in terms of volumetric and gravimetric energy density, ref. [16]*, copyright (2001).*

As a core component for mobile devices, the LIBs should possess enough electrochemical properties including: high energy density, high power density and long cycling life. They should also be of low-cost and safe. Currently, liquid electrolytes (LEs) used in LIBs are normally prepared by Li salt dissolved in organic solvents, which are intrinsically volatile, toxic and flammable. The organic LEs undergo oxidative decomposition above 4.2 V, which blocks the application of high-voltage cathodes. The separators and LEs account for 40 vol.% and 25 wt.% in the full battery, reducing the corresponding specific capacity. The application of LEs can cause short-circuit and

terrible explosion due to overheating, overcharging and lithium dendrite, and here some accidents involving the LIBs are listed in Figure 1.5. Battery safety directly influences customers' lives and their possessions. Given safety concerns encountered with LEs, SEs were proposed to eliminate the safety issues because of their intrinsic solid character [17]. Although now it is difficult to achieve highly conductive SEs which are comparable to the LEs, the commercial application of SSBs has been widely envisioned (see Figure 1.4). In order to face the unsolved problems, LMBs using SEs are mainly discussed in this thesis to broaden effective strategies for the eventual commercialization of SSBs in the near future.

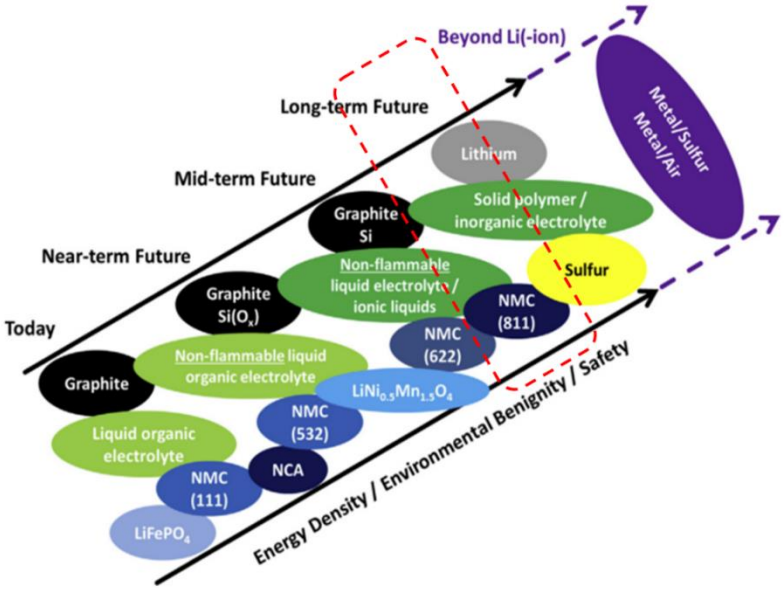

Figure 1.4. The developing trend for the LIBs with respect to the employed anode, electrolyte, and cathode materials, ref. [15]*, copyright (2018).*

Figure 1.5 Recent reports about the explosion accidents of the LIBs.

Chapter 2 Fundamentals

2.1 Basic structure of cells

In general, an EV battery pack is composed of tens of electrochemical modules via parallel connection to offer nominal voltage (~300 V). The modules consist of certain numbers of cells (1.5 V for cylindrical cell or 6 V for pouch cell) via parallel connection, series connection or series-parallel connection. As shown in Figure 2.1, a cylindrical cell is composed of cathode and anode separated by an electronic insulated separator that either is immersive in a Li^+ conductive organic solution (*i.e.*, in LIBs), or simply contacts with a Li^+ superionic conductor (*i.e.*, in LMBs) [18]. Two electrodes possess different electrochemical potentials producing a certain potential difference ($E^{\ominus}$). When they are connected via an external circuit, a generated electron flow transfers from the anode (negative electrode) to cathode (positive electrode). Spontaneously, positively charged ions migrate in the same direction within the cell to keep charge balance. Different from primary batteries, Li^+ ions can transfer back from the cathode to the anode when applying an external potential in secondary batteries, which can be reversibly charged and discharged hundreds of times until they run out of service life.

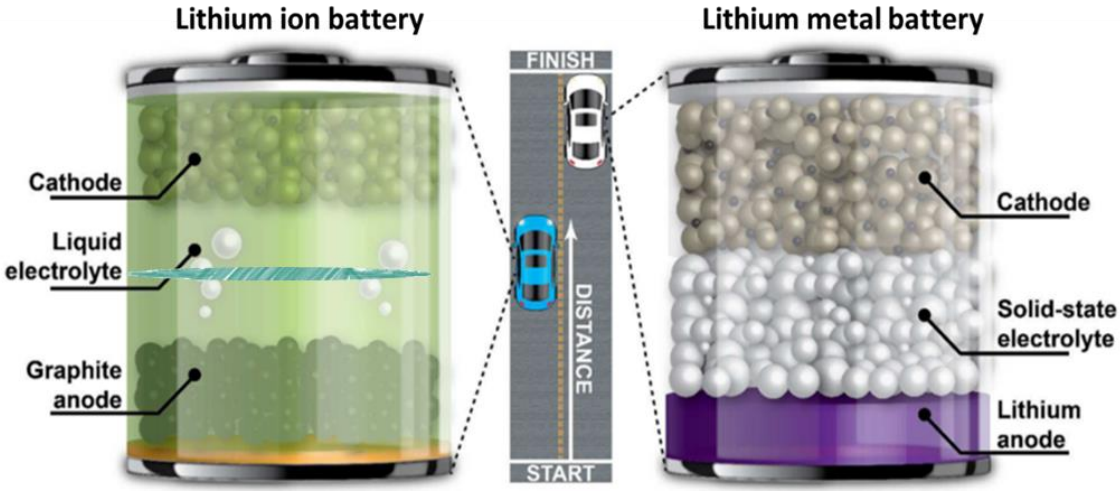

Figure 2.1. Structural illustration of the LIB and the solid state LMB, ref. [18], copyright (2017).

To better understand the content of this thesis, some terms related to batteries are listed below:

- **Cathode**: the positive electrode of the cell which accepts electrons from the external circuit during charge process (see typical cathode materials in Figure 2.2);
- **Anode**: the negative electrode of the cell which donates electrons to the external circuit during charge process (see typical anode materials in Figure 2.2);

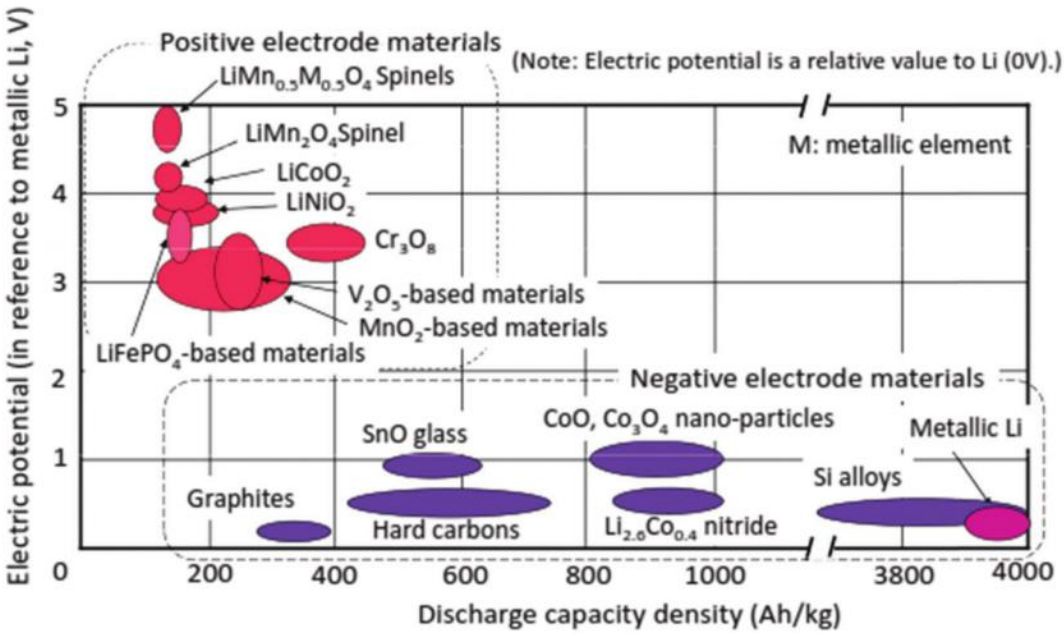

Figure 2.2. Cathode/anode materials and corresponding electrochemical performances, ref. [23], copyright (2013).

- **Electrolyte**: a mixture containing single or multiple lithium salt(s) dispersed in an organic solvent or ionic conductor, displaying enough ionic conductivity but extremely low electronic conductivity. For instance, Li^+ ion can hop from one site to another through Schottky- or Frenkel defects in Li^+ superionic conductors, or they can migrate along amorphous pathways in polymer electrolytes at high temperature (HT);
- **Specific capacity** (C, mAh g^{-1}): the charges per unit of mass of an active material. It can be calculated through $C = It/m$, where I is the current applied, t is the time of charge/discharge, m is the mass of active material, respectively. The theoretical specific capacity is given by $C = nF/M$, where n is the number of electrons transferred during the redox reaction, F is the Faraday constant (96485.3 C mol^{-1}), M is the molar weight of the active material, respectively;
- **C-rate**: a 1C rate means that a cell discharges (or charges) to a theoretical capacity in 1 h; by the same token, nC rate requires the discharge (or charge) time of 1/n h, which is usually used to represent current density (A g^{-1}) during charge/discharge;
- **Carrier mobility**: it is used to characterize the ion migration rate from one site to another through ionic conductors in the presence of an electric field. There is an analogous quantity with respect to the holes of solid crystals, called hole mobility in SEs;

- **Ionic conductivity** (σ, S cm^{-1}): a coefficient that can characterize the ionic conductive property of material. It is influenced by the charge carrier concentration n and the ionic mobility μ according to $\sigma = nze\mu$, where z is the number of electrons delivered per charge carrier and e is the charge of electron. On the other hand, the ionic conductivity σ is expressed as the inverse of resistivity (ρ), *i.e.*, $\sigma = 1/\rho = l/RA$, where l, A and R are the electrode thickness (cm), electrode surface area (cm^2) and resistance (Ω), respectively;
- **Diffusion coefficient** (D, cm^2 s^{-1}): based on Nernst-Einstein relationship, the diffusion coefficient is expressed as $D = \mu kT/ez = kT\sigma/n(ez)^2$, where μ is the ionic mobility, and k is the Boltzmann constant (1.380648 × 10^{-23} J K^{-1}, which is equal to the gas constant (R = 8.31446 J·mol^{-1}·K^{-1}) ÷ Avogadro constant (N_A = 6.02 × 10^{23} mol^{-1}) , and T is the absolute temperature (T, K);
- **Coulombic (Faradaic) efficiency**: the ratio of charge to discharge/charge durations. It is primarily less than 100 % due to the charge loss in irreversible side reactions;
- **Activation energy** (E_a, eV (J mol^{-1})): ions require minimum energy for ion to jump out of potential well and hop from one position to another. Two transport models are used to quantify the activation energy as stated below:
- **Arrhenius model** is most suitable for the first behavior of ion migration withth fixed crystal lattices, as shown in Eq. 2.1 and 2.2, where σ_0 is the pre-exponential factor, k is Boltzmann constant, E_a is the activation energy, σ is overall conductivity at a given absolute temperature (T, K), respectively;

$$\sigma = \sigma_0 \exp(-E_a/kT) \quad (Eq.\ 2.1)$$

$$\ln(\sigma) = \ln(\sigma_0) - E_a/kT \quad (Eq.\ 2.2)$$

- **Vogel–Tammann–Fulchermodel (VTF) model** is preferable for ion migration in host materials with free volume, *e.g.*, polymer electrolytes. In Eq. 2.3, σ_0 is a pre-exponential factor related to the number of charge carriers, T_0 is an idealized temperature corresponding to zero configuration entropy, which is normally 50 K lower than the glass transition temperature (T_g) of the polymer matrix, E_a is the activation energy related to polymer segmental motion, k is Boltzmann constant, and T is the given absolute temperature (T, K). A factor of $T^{-1/2}$ is often included in the pre-exponential constant σ_0 in the VTF equation for entirely reproducible trends [19]. One issue that needs to be

addressed is that when inorganic fillers and Li salts are mixed in the polymer matrix, the T_g can increase, because the impeded chain movement results in the coordination of Li^+ by ether oxygen and filler geometrical constraint [20]. On the contrary, the temperature can determine polymer segmental motion according to the free-volume model. This VTF model can separate the effects of carrier concentration and segmental motion on ionic conductivity at given T.

$$\sigma = \sigma_0 T^{-1/2} \exp(-E_a/k(T - T_0) \quad (Eq.\ 2.3)$$

$$log_{10}(\sigma T^{1/2}) = log_{10}\,\sigma_0 - 0.43(E_a/(k(T - T_0)) \quad (Eq.\ 2.4)$$

2.2 Thermodynamics and kinetics

Gibbs free energy as the "available energy" in a redox system was proposed in the 1870's by Josiah Willard Gibbs. Given that rechargeable batteries involve the reversible ion charge/discharge, the possibility of spontaneous reactions is calculated based on Gibbs free energy (G, J) as stated in Eq. 2.8, which is the sum of its enthalpy (H, J), and entropy (S, J K^{-1}) times the reaction temperature (T, K) of the system:

$$G = H - TS \quad (Eq.\ 2.8)$$

Spontaneous reactions are considered to be natural processes without any external action towards it, when the change of G during reactions (ΔG) is negative. Otherwise, it is a nonspontaneous reaction, which needs supplies of extra energy. In a chemical reaction involving the changes in thermodynamic quantities, a variation of standard free energy is stated as follows (see Eq. 2.9):

$$\Delta G = \Delta H - T\Delta S \quad (Eq.\ 2.9)$$

In a rechargeable battery, the maximum energy (E_{max}) available for the spontaneous electrochemical reaction can be given as ΔG at RT and calculated by Nernst Equation (Eq. 2.10), where F is the Faraday constant, $E^{\ominus}_{MF}$ is the standard potential difference, $E^{\ominus}_{anode}$ and $E^{\ominus}_{cathode}$ are the standard potential at the anode and the cathode, respectively:

$$E_{max} = \Delta_r G_m = -zFE^{\ominus}_{MF} = -zF(E^{\ominus}_{cathode} - E^{\ominus}_{anode}) \quad (Eq.\ 2.10)$$

$$\Delta G^{\ominus}_{MF} = -zFE^{\ominus}_{MF} \quad (Eq.\ 2.11)$$

when $E^{\ominus}_{MF}$ is positive, the reaction is spontaneous. In fact, the ΔG under non-standard conditions can be described as $\Delta G^{\ominus}_{MF}$ via $\Delta G = \Delta G^{\ominus}_{MF} + RTlnQ$; when redox reaction proceeds, cell

potential gradually decreases until the reaction reaches equilibrium, namely $\Delta G = 0$ when the equilibrium constant $Q = K_{eq}$ ($T = 298$ K):

$$logK_{eq.} = nE_{MF}^{\ominus}/0.0592\text{V} \quad (Eq.\,2.12)$$

This conclusion fits Le Châtlier's Principle, when an equilibrium system changes, the system minimizes this change by shifting the equilibrium in the opposite direction. Herein when $logK_{eq.} > 0$, $E_{MF}^{\ominus} > 0$, it is a spontaneous reaction. In fact, the discharge (charge) voltage should be lower (higher) than the theoretical equilibrium voltage when the spontaneous currents go through the electrode. This is due to kinetic limitations of charge transfer including physical-, chemical- and electrochemical factors: the activation polarization of charge-transfer at electrode/electrolyte interface; the ohm polarization of the interface resistance of individual components; the concentration polarization of mass transport close to the interface. These limitations can strongly influence the ionic migration in bulk electrolyte and around the interfaces. To achieve high-performance rechargeable batteries, one must consider both thermodynamic and kinetic factors for ion transfer in full battery.

2.3 Solid electrolytes for lithium metal batteries

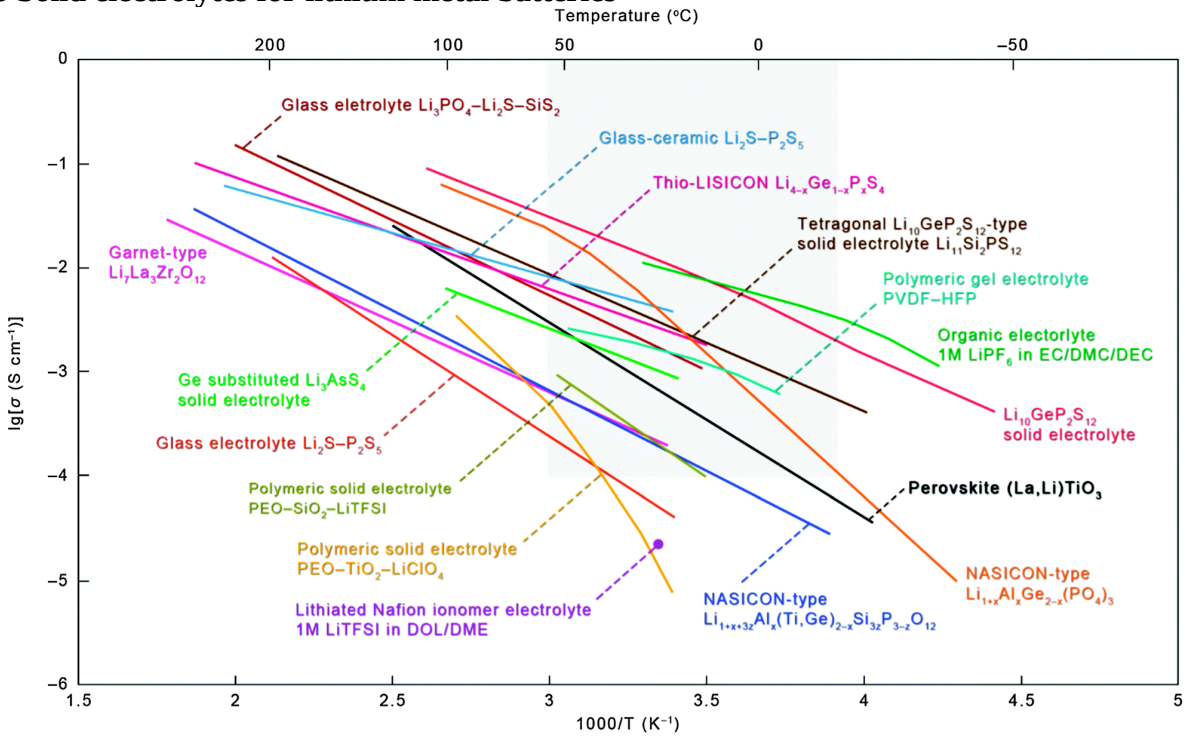

Figure 2.3. Ionic conductivity of various SEs as a function of temperature, ref. [21]*, copyright (2011).*

In the last 200 years, the battery research was mainly focused on LE systems in terms of high ion conductivity. However, side reactions between electrode and organic LE can exacerbate solid electrolyte interphase (SEI) with growing resistance [22]. Furthermore, the uncontrolled growth of lithium dendrite using LEs can lead to short-circuit during charge/discharge, especially at low temperature and high C-rate. To finally solve this safety issue, SSBs using SEs are proposed due to the following advantages [23–25]:

- high safety, SEs exhibit superior properties including high mechanical strength, no threat of dendrite penetration, non-flammable, non-corrosive, non-volatile and leakage-free;
- high transport number, only Li^+ ions are mobile in SEs (theoretically close to 1 in crystal SEs);
- high energy density, a wide electrochemical window of the SEs allows the application of high-voltage cathodes and Li metal anode; a thin SE layer is enough to replace the traditional LE and separator, which account for nearly 40 vol.% and 25 wt.% of the battery; and stable SSBs can also reduce battery management devices;
- high flexibility, especially for the polymer electrolyte;
- high chemical stability, especially for the polymer- and oxide electrolytes.

Therefore, replacing LEs with SEs can not only overcome the intrinsic problems of LEs, but also offer possibilities of new battery system development. Based on recent reports, crystal/glassy sulfide and crystal garnet oxide can provide high ionic conductivities (see Figure 2.3 and Table 2.1). Nevertheless it is difficult to achieve the same order of magnitudes as LP30 (ionic conductivity of ~10^{-2} S cm^{-1} at RT), because of the poor interface contact in the SEs [25]. In general, the core issue of the SSB development lies in the low conductivity itself, and the secondary issue is the optimization of interface properties.

Building SSBs with performance-oriented SEs is of great importance. To understand the background of the state-of-art SEs and their ion-transport mechanisms, a brief review will be presented here. In 1833, Michael Faraday found ionic conduction in the heated Ag_2S and PbF_2 [26]. Efforts to incorporate SEs, *i.e.*, $Na_2O{\cdot}11Al_2O_3$, Ag_4KI and $RbAgI_4$, into batteries can be traced to the 1960s [27,28]. In 1973, the discovery of ionic transport in a polymer material, *e.g.*, polyethylene oxide (PEO), widened the material scope of SEs [29]. Currently, Bolloré in France, Sakti3 in the United States and Toyota in Japan hold many patents of the SSB technology, which represent the

three developing directions of the SEs: polymers, oxides and sulfides. In addition, Samsung in Korea focuses on the sulfide electrolyte system, and CATL in China is also developing polymer electrolyte system. Since the 1990s thin-film battery using $Li_{3.3}PO_{3.9}N_{0.17}$ (LiPON) has been commercialized [28], methods like pulsed laser deposition, radio frequency magnetron sputtering and spark plasma sintering have been explored for the thin-film batteries. However, these high-cost methods can only be applied in microelectronic devices, but not in large energy output [30–32]. In contrast, the bulk-type SSBs with massive loading mass and high energy density are more appropriate for EV applications (see Figure 2.4). Therefore, bulk-type batteries using SEs are mainly discussed in this thesis.

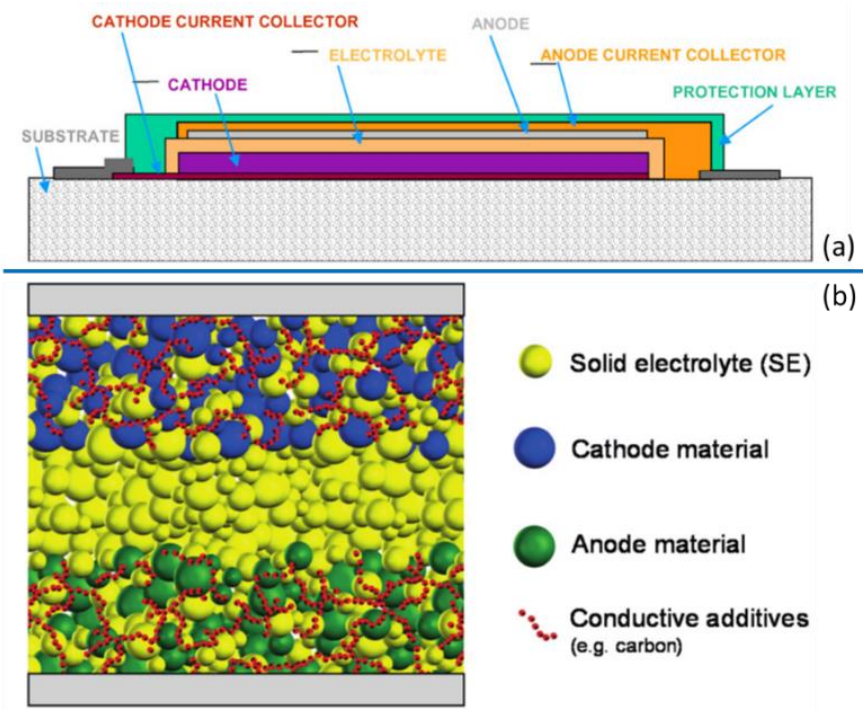

Figure 2.4. Schematic diagram of thin film battery (a) and bulk-type battery (b), refs. [27,33]*, copyright (2008/2015).*

2.3.1 Sulfide-type solid electrolytes

Among the SEs, sulfide-type SEs display relatively high conductivities of 10^{-4} ~ 10^{-2} S cm^{-1} at RT, *e.g.*, $Li_{10}GeP_2S_{12}$ displays higher conductivity than that of LP30, because the sulfur atoms possess large atomic radius and they are easy to be polarized [34]. For example, the conductivity of lithium phosphorus oxysulfide (LiPOS) is higher than that of LiPON [35]. Sulfide-type SEs are classified into four groups according to their chemical compositions, namely thiophosphates, halide thiophosphates, sulfide without phosphorus, and glassy sulfide electrolytes (see Figure 2.5). The

soft sulfide-type SEs are easily deformed, because their Young's modulus is between the ceramics oxide and organic polymers, inducing their low grain-boundary resistance when applying high-pressure compressing [36]. Therefore, sulfide-type SEs are considered to be the competitive candidates to replace LEs, ultimately fabricating high-performance batteries [19].

Table 2.1. Comparison of various SEs for Li^+ ion, ref. [25], copyright (2017).

Type	Materials	Conductivity ($S\,cm^{-1}$)	Advantages	Disadvantages
Oxide	Perovskite $Li_{3.3}La_{0.56}TiO_3$, NASICON $LiTi_2(PO_4)_3$, LISICON $Li_{14}Zn(GeO_4)_4$ and garnet $Li_7La_3Zr_2O_{12}$	10^{-5}–10^{-3}	• High chemical and electrochemical stability • High mechanical strength • High electrochemical oxidation voltage	• Non-flexible • Expensive large-scale production
Sulfide	Li_2S–P_2S_5, Li_2S–P_2S_5–MS_x	10^{-7}–10^{-3}	• High conductivity • Good mechanical strength and mechanical flexibility • Low grain-boundary resistance	• Low oxidation stability • Sensitive to moisture • Poor compatibility with cathode materials
Hydride	$LiBH_4$, $LiBH_4$–LiX (X = Cl, Br or I), $LiBH_4$–$LiNH_2$, $LiNH_2$, Li_3AlH_6 and Li_2NH	10^{-7}–10^{-4}	• Low grain-boundary resistance • Stable with lithium metal • Good mechanical strength and mechanical flexibility	• Sensitive to moisture • Poor compatibility with cathode materials
Halide	LiI, spinel Li_2ZnI_4 and anti-perovskite Li_3OCl	10^{-8}–10^{-5}	• Stable with lithium metal • Good mechanical strength and mechanical flexibility	• Sensitive to moisture • Low oxidation voltage • Low conductivity
Borate or phosphate	$Li_2B_4O_7$, Li_3PO_4 and Li_2O–B_2O_3–P_2O_5	10^{-7}–10^{-6}	• Facile manufacturing process • Good manufacturing reproducibility • Good durability	• Relatively low conductivity
Thin film	LiPON	10^{-6}	• Stable with lithium metal • Stable with cathode materials	• Expensive large-scale production
Polymer	PEO	10^{-4} (65–78 °C)	• Stable with lithium metal • Flexible • Easy to produce a large-area membrane • Low shear modulus	• Limited thermal stability • Low oxidation voltage (<4 V)

LiPON, lithium phosphorus oxynitride; LISICON, lithium superionic conductor; NASICON, sodium superionic conductor; PEO, poly(ethylene oxide).

2.3.1.1 Glassy sulfide-type solid electrolytes

In 1981, B_2S_3-Li_2S was firstly prepared via mechanical milling, and research into sulfide-type SEs started in 1986 with the Li_2S–SiS_2, and then glassy sulfide-type SEs (Li_2S-B_2S_3-LiI, Li_2S-P_2S_5-LiI, Li_2S-SiS_2-LiI and Li_2S-GeS_2) were intensively studied [37,38]. Such sulfide-type SEs are isotropic ionic conductors, meaning no grain boundary resistance. Generally speaking, the ionic conductivity of glassy sulfide decreases with their crystallization, but the opposite trend was observed in the $Li_7P_3S_{11}$, due to its highly conductive nanocrystalline phase. In addition, partial crystallization of glassy $Li_2S{\cdot}P_2S_5$ with heat-treatment at 200~300 °C can increase the conductivity to ~10^{-3} S cm^{-1} [39,40]. Glass-crystal SEs, $xLi_2S{\cdot}(1\text{-}x)P_2S_5$ with x = 0.7~0.8 has been extensively

considered an optimal structure for high conductivity, where Li^+ prefers to migrate along zigzag routes in the open space between P_2S_7 ditetrahedra and slightly distorted PS_4 tetrahedra in $Li_7P_3S_{11}$ [41]. Moreover, $75Li_2S{\cdot}25P_2S_5$ displays a relatively higher moisture stability due to the PS_4^{3-} ion.

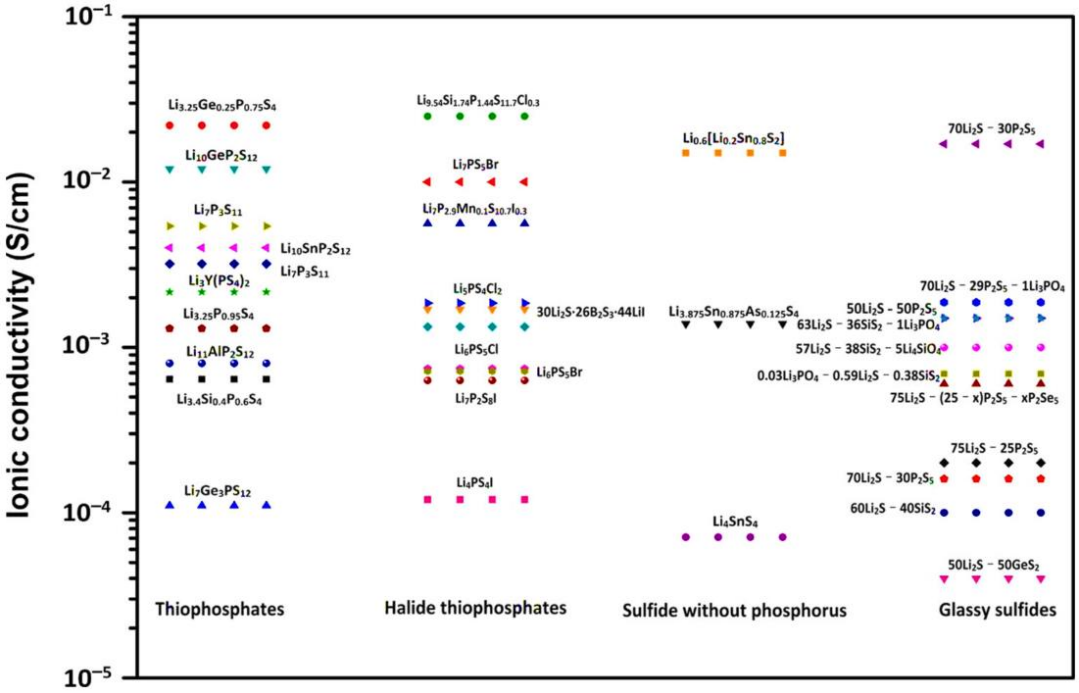

Figure 2.5. Reported ionic conductivities of SE materials at RT, including thiophosphates, halide thiophosphates, sulfides without phosphorus, and glassy sulfides, ref. [24]*, copyright (2017).*

2.3.1.2 Crystalline sulfide-type solid electrolytes

In 2001, thio-LISICON ($Li_{3.25}Ge_{0.25}P_{0.75}S_4$) was first reported with extremely high ionic conductivity at RT [34]; then the next breakthrough was made on $Li_{10}GeP_2S_{12}$ reported by Kamaya Noriaki et al. [21]. These two SEs are based on the concept of aliovalent substitution with the same chemical formula: $Li_{4-x}Ge_{1-x}P_xS_4$, where x = 3/4 for thio-LISICON and x = 2/3 for LGPS. The aliovalent substitution can create vacancies or interstitials (ionic compensation), which serves as fast Li^+ pathways [42]. First-principles study of the $Li_{10}GeP_2S_{12}$ confirms that fast ionic conduction occurs in three dimensions (4×10^{-2} S cm^{-1} in the *c*-direction and 9×10^{-4} S cm^{-1} in the *ab* plane). In addition, body-centered cubic anion lattices in $Li_{10}GeP_2S_{12}$ and $Li_7P_3S_{11}$ are suitable for Li^+ diffusion between interconnected tetrahedral sites [43,44]. Inspired by LGPS, abundant Si, Sn, Al and Zn were used to replace the expensive Ge and to enhance chemical moisture stability [45]. Moreover, crystalline halide thiophosphates (Li_6PS_5X, X = Cl, Br, I) exhibit high conductivities of

10^{-4}~10^{-3} S cm^{-1} at 25 °C, and halogen doping can improve electrochemical stable window of sulfide SEs up to ~10 V *vs.* Li/Li^+ [24,46,47].

2.3.1.3 Drawbacks of sulfide-type solid electrolytes

Sulfide-type SEs have their own drawbacks, such as expensive raw materials (*e.g.* Ge and Li_2S), poor thermal stability, high reactivity with moisture (generating toxic H_2S gas) and lithium [31]. The electrochemical stability of electrolytes is important for long durability and high rate capability. Given the poor electrochemical stability, an artificial passivation layer is necessary for sulfide-type SEs. Therefore, some additives like Li_2O, LiI, FeS, CaO and Li_xMO_2 (M = Co, Ni, and Mn) were incorporated into $Li_2S{\cdot}P_2S_5$ to suppress the generation of H_2S [48,49]. In the lab, high-cost Li alloy (*e.g.*, Li-In and Li-Al) was used as a counter/reference electrode to restrain side reactions.

The practical application of sulfide SEs was also limited by their narrow electrochemical window. Ge in LGPS can be reduced at a low potential of 0.6 V *vs.* Li/Li^+ due to its narrow band gap [50]. Moreover, the SE decomposition and elemental migration can occur at the electrolyte/electrode interface, restricting the Li^+ conduction [51]. The interface growth of $Li_7P_3S_{11}$ consisting of the Li_2S and Li_3P can obviously enlarge resistance during longtime cycling [52]. However, SEI layers formed with respect to $Li_7P_3S_{11}$ and Li_6PS_5X (X = Cl, Br) are Li^+ conductive but electron nonconductive, which can prevent further side reactions [53].

2.3.2 Oxide-type solid electrolytes

Lithium superionic conductor (LISICON)-structured Li_4SiO_4-Li_3PO_4, the sodium superionic conductor (NASICON)-structured $Li_{1.3}Al_{0.3}Ti_{1.7}PO_4)_3$ (LATP), the garnet-structured $Li_7La_3Zr_2O_{12}$ (LLZ), and the perovskite-structured $Li_{3x}La_{2/3-2x}\square_{1/3-2x}TiO_3$ ($0<x<0.16$) (LLT) are intensively studied as oxide-type electrolytes, displaying relatively low conductivities in the range of 10^{-6} ~10^{-3} S cm^{-1} at RT. The Li^+ migration mechanisms of oxide-type SEs are summarized in Figure 2.6, where Li^+ ions have to overcome the local bottleneck which requires higher activation energy and favorable pathway in crystal lattice. Compared to sulfide-type SEs which must be handled in the glovebox, oxide-type SEs can be handled in the dry-air due to their higher stability, which makes it facile to prepare oxide-type SEs and to assemble SSBs. On the other hand, oxide-type SE powders need to be shaped into compressed pellets, for which high-temperature sintering is always

needed since that cold pressing is not enough to produce a close contact between the ceramic particles for favorable Li^+ conduction. It is noteworthy that the intrinsically brittle and rigid pellets are still difficult to be integrated into full batteries.

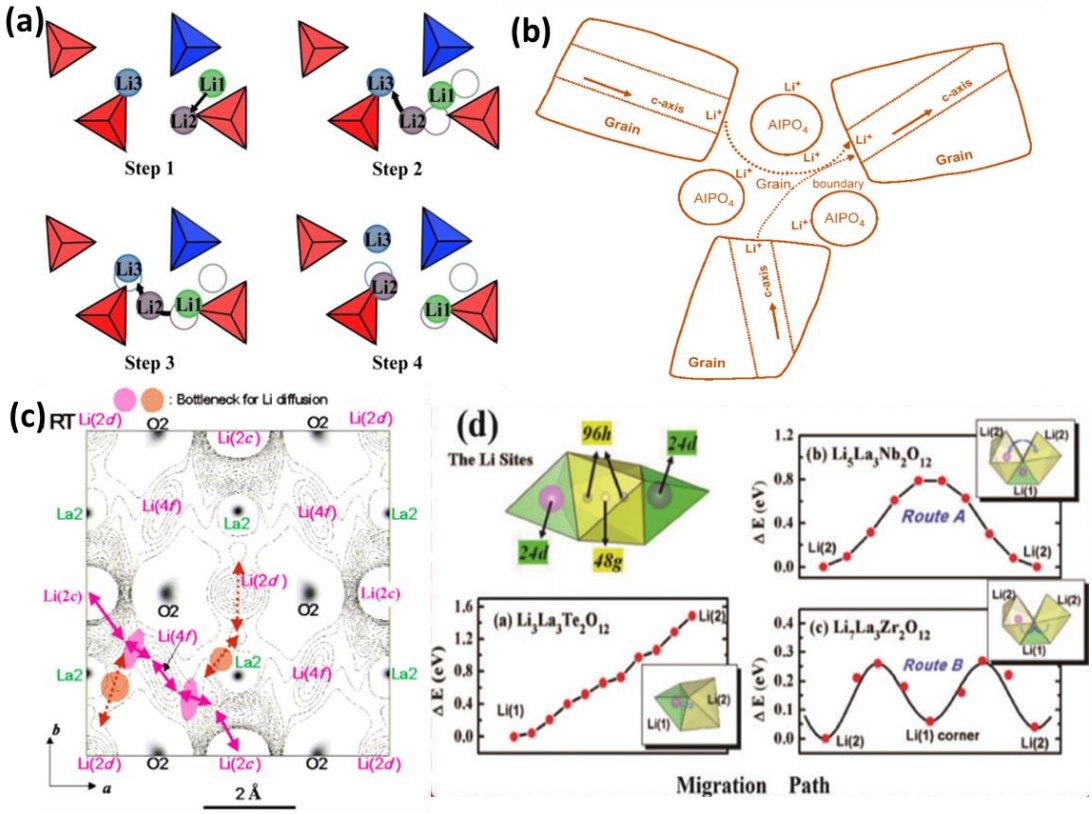

Figure 2.6. a) MD simulation of Li^+ positions in $Li_{3.5}Si_{0.5}P_{0.5}O_4$ showing the cooperative interstitial mechanism: the migrating interstitial Li^+ (green) displaces another Li^+ (purple) toward a neighbour site, leading to further Li^+ (blue) migration (PO_4, red; SiO_4, blue), ref. [54]*, copyright (2015). b) Schematic image of Li^+ transport through the voids of LAGP based on space charge mechanism, ref.* [55]*, copyright (2009). c) Schematic representation of scattering amplitude distribution in La_2–O_2 layer of $La_{0.62}Li_{0.16}TiO_3$ at RT, ref.* [56]*, copyright (2006). d) Li sites and two predominant mechanisms of Li migration in garnet LLZ, ref.* [57]*, copyright (2011).*

2.3.2.1 LISICON-type solid electrolytes

In 1978, the LISICON-type SE $Li1_4Zn(GeO_4)_4$ was reported with a conductivity of 0.13 S cm^{-1} at 300 ℃ [58]. Then the same structure of Li_4SiO_4–γLi_3PO_4 with MO_4-based tetrahedral (M = Si or P) units and Li–O polyhedra was considered a Li^+ solid solvent. Whether there is a single solid-solution phase or two distinct crystal phases in Li_4SiO_4–γLi_3PO_4 is still unclear [59]. High ionic conductivity is ascribed to numerous Li interstitials based on the cooperative interstitial mechanism (see Figure 2.6a) [54]. LISICON-type electrolytes can work at high temperature due to their high

thermal/chemical stability and near-zero vapor pressure [60]. However, the low ionic conductivity at RT (10^{-7} S cm^{-1}) and poor stability with Li anode limit the further application [61].

2.3.2.2 NASICON-type solid electrolytes

In 1976, Goodenough *et al.* reported the NASICON-type $Na_{1+x}Zr_2P_{3-x}Si_xO_{12}$ through partial substitution of P with Si in $NaM_2(PO_4)_3$ structure (M = Ge, Ti or Zr) [62]. The typical NASICON framework consists of corner-sharing PO_4 tetrahedra and MO_6 octahedra. When Na^+ located at interstitial sites were replaced by Li^+, the NASICON structure turned into a Li^+ conductor [58,63]. Due to the small ionic radius (0.53 Å), partial substitution of Ti with Al in $LiTi_2(PO_4)_3$ and Ge in $LiGe_2(PO_4)_3$ can produce $Li_{1+x}Al_xTi_{2-x}(PO_4)_3$ (LATP) and $Li_{1+x}Al_xGe_{2-x}(PO_4)_3$ (LAGP), respectively, both exhibiting higher conductivities than the original compounds at RT, *e.g.*, 6.21×10^{-4} S cm^{-1} for $Li_{1.4}Al_{0.4}Ti_{1.6}(PO_4)_3$, while ~$10^{-2}$ S cm^{-1} for $Li_{1.5}Al_{0.5}Ge_{1.5}(PO_4)_3$ [64,65]. Because glass–ceramics SEs are heterogeneous polycrystals, space charge effect can occur at voids or gaps due to the large interface- and grain resistances, where local uncompensated charges can accumulate or deplete on a dielectric surface in a heterogeneous NASICON-type SE [66]. However, some undetermined controversy about the space-charge mechanism still exists. Analogous to the Li_2O dielectric phase, $AlPO_4$ can adsorb mobile Li^+ ions and then desorb them at a specific temperature, thus improving ionic conductivity (see Figure 2.6b) [55]. However, Ti^{4+} in LATP is easy to be reduced by metallic Li, and high-cost Ge element in LAGP is also not economical [67].

2.3.2.3 Perovskite-type solid electrolytes

Perovskite-structure $Li_{3x}La_{2/3-x}TiO_3$ (LLT) was prepared with aliovalent substitution of Li^+ and La^{3+}. Such substitution results in more vacancies, allowing fast migration of Li^+ based on the defect-type mechanism to achieve a high bulk ionic conductivity of ~10^{-3} S cm^{-1} at RT [64,68,69]. Perovskite-type SEs are composed of double subcells with La-rich (La ions and vacancies alternated along the *c*-axis) and La-deficient (only disordered vacancies along the *c*-axis) phases arranged alternately. As shown in Figure 2.6c, Li^+ located on 2c, 2d and 4f sites of the La_2–O_2 layer can migrate along the 2c–4f–2c diffusion path (pink arrows) or 2c–2d–2c diffusion path (orange dashed arrows) [56]. Therefore, the ionic conductivity of perovskite-type SEs relies on the contents of Li, La and vacancies, since the cation size and bottleneck can directly determine the migration pathways. Additionally, optimal quenching process and sintering atmosphere can enhance

conductivity by decreasing the size of microdomains and interface resistance [61]. Similarly to LATP, Ti^{4+} in $Li_{3x}La_{2/3-x}TiO_3$ can be reduced into Ti^{3+} when directly contacting with metallic Li, generating an electron/ion conductive interphase and leading to short circuit.

2.3.2.4 Garnet-type solid electrolytes

Since 2007, Ramaswamy *et al.* proposed the concept of garnet-type LLZ [70]. Excellent properties including high ionic conductivity, superior thermal and chemical stability are found in this Li stuffed SE, where the 'stuffed' means its relatively high Li content (7Li pfu) compared to other garnet materials (*e. g.*, $Li_3La_3M_2O_{12}$ (M = Te, Nb) [71], $Li_5La_3M_2O_{12}$ (M = Nb, Ta) [57], $Li_5La_3Sb_2O_{12}$/$Li_6SrLa_2Sb_2O_{12}$ [72], $Li_6La_2MTa_2O_{12}$ (M = Sr, Ba) [73]). The increase of Li content in garnet structure from 3Li pfu to 7Li pfu can facilitate Li^+ migration through low-energy pathways for high ionic conductivity [74,75]. 7.5Li pfu is the upper limit in the $Li_xB_2C_3O_{12}$ garnet-type SEs, and the optimal ionic conductivity is obtained at around 6.4Li pfu [75,76]. LLZ shows two crystalline phases: tetragonal (space group $I41/acd$) and cubic (space groups centric $Ia\bar{3}d$ and acentric $I\bar{4}3d$) [77–79]. Importantly, the cubic phase exhibits two orders of magnitude larger conductivity comparing to the tetragonal phase at RT, which was proved by both experiment results [70,80,81] and simulations [82,83]. This is because the cubic phase contains disordered tetrahedral and octahedral Li^+ sites, and its high symmetry structure can increase vacancy content. In addition, self-diffusion of Li^+ in LLZ solid phase is controlled by two factors: (1) the restriction imposed on occupied site-to-site interatomic separation; (2) the unstable residence of Li^+ at the 24d site, which can induce neighbors Li reconfiguration to accommodate the initial movement (see Figure 2.6d) [82,83]. High mobility in octahedral sites is caused by static repulsion of the short Li–Li distance, rather than dynamic processes. Additionally, phase stability of the garnet-type SEs relies on an internal structural strain and Li^+ content in the sublattice. They have a wide electrochemical stability windows (≥ 6 V *vs.* Li/Li^+), and high stability against metallic Li [66,84]. It is also noteworthy that garnet-type SEs firstly react with H_2O, and then possibly with CO_2, which makes it better to handle the electrolytes in a superdry air to ensure the insulation from moisture.

2.3.3 Polymer-based solid electrolytes

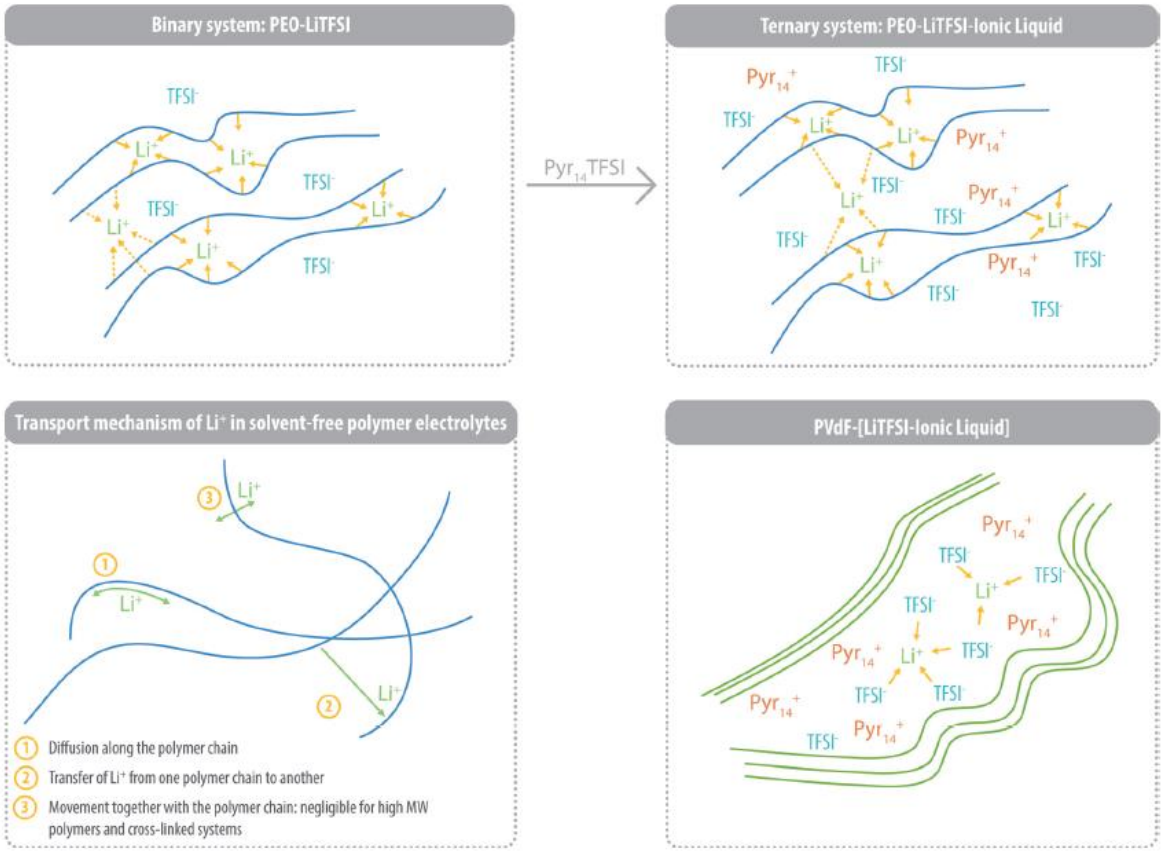

Figure 2.7. Schematic of the conduction mechanism in the PSEs: a) Li^+ ion coordination, ref. [85]*, b) active polymers (e.g., PEO), ref.* [86]*. c) Li^+ ion coordination, ref.* [87]*. d) inactive polymers (e.g., PVdF), ref.* [88]*, copyright (2015).*

Polymer-based SEs (PSEs) are normally composed of Li salt(s) dissolved in polymer matrix. In 1975, Wright *et al.* firstly found ion conduction in PEO-alkali metal salt complex [89]. Similarly to PEO, poly(acrylonitrile) (PAN), poly(vinyl chloride) (PVC), poly(vinylidene fluoride) (PVDF), poly(methylmethacrylate) (PMMA) and poly(vinylidene fluoride)-hexafluoropropylene (PVDF-HFP) have been studied as PSE matrixes [90]. When considering the Li^+ solvation, strong complexing coordination induced by oxygen atom is found in ether, carbonates, esters and ketones groups. Recent studies confirmed that Li^+ prefers to coordinate with glycol ether, especially the one of suitable length showing a high ionic conductivity [91,92]. Due to the high donor number to trap Li^+ ions, high dielectric constant and strong Li^+ solvating ability, PEO is intensively studied as polymer electrolytes. The ionized salts are selected to bond polar groups of polymers, forming four to six coordination bonds with Li^+ based on the Lewis-base theory. Therefore, mobile ions dissociate and hop along polymer segmental via the propelling dynamic motion in free volume space [85,93]. Additionally, ionic diffusion is much faster than the segmental relaxation, which

means that ionic conductivity is not associated with polymer segmental relaxation [94]. Although high conductivity found in some crystalline complex [86], most studies confirmed that ion transport occurs in the amorphous phase above T_g, because the crystalline regions can block ion migration [85]. The conduction mechanisms in the various PSEs are depicted in Figure 2.7.

In contrast to LEs and gel electrolytes, PSEs are stable below 80 °C. The major issue for PSEs is their low ionic conductivity (10^{-6} ~ 10^{-4} S cm^{-1} at elevated temperature), because PSEs cannot provide enough mobile Li^+ and surface contact with the electrode. Direct casting PSEs on top of the electrode surface can increase the contact surface area, but it is difficult for the macromolecules to penetrate into the small pores of the electrodes. When the PSE films solidify during *in situ* casting via copolymerization or solvent-evaporation, the shrink force will separate electrode and current collector, resulting in a terrible interface contact. Therefore, how to improve sufficient contact is a challenge for SPE application.

To improve conductivity, some inorganic fillers are incorporated into PEO, forming a sort of amorphous matrix of Li salts, called composite solid electrolyte (CSE), which serves not only as a support for matrix to improve mechanical properties, but also restricts the recrystallization of polymer chains [95–98]. Different from dead Li^+ fillers like SiO_2 [99], TiO_2 [100] and Al_2O_3 [101], active Li^+ fillers, *i.e.*, LLZ [102,103], LLT [68] and LATP [104], also involve conduction process and induce additional conductivity [105]. The synergistic effect of active fillers and polymer electrolytes can maximize their mechanical strengths and wettability to solve the inherent problems [106]. Recently, CSEs have been tremendously researched, and the optimal engineering of CSEs is attractive to high-performance SSBs.

2.4 Limitations of the solid electrolytes

As mentioned above, all the SEs have their advantages and disadvantages (as summarized in Figure 2.8). For commercial application in the future, SEs should possess the following comprehensive properties [42]:

- High ionic conductivity at RT with low polarization effects;
- Low interfacial resistance with negligible electronic conductivity;
- Wide electrochemical window above 5.0 V with high electrochemical stability;
- Low thermal expansion coefficients and high chemical stability with electrodes, especially Li anode;

- Sufficient polarizable carriers and hosts;
- Low cost, facile synthesis, and environmentally-friendly assembly.

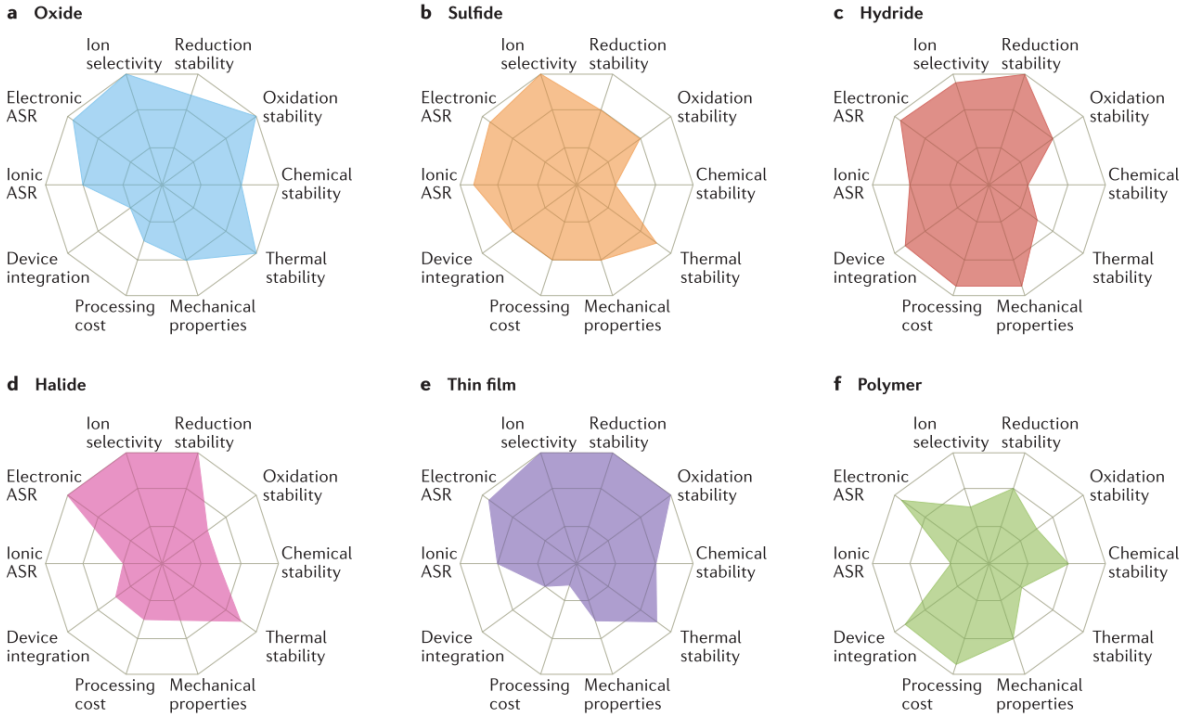

Figure 2.8. Performance of different solid electrolyte materials. Radar plots of the performance properties of oxide-type SEs (a), sulfide-type SEs (b), hydride-type SEs (c), halide-type SEs (d), thin-film electrolytes (e) and PSEs (f). ASR, area-specific resistance, ref. [25]*, copyright (2017).*

Currently, CSE has been commercialized in the bulk-type battery. i.e., Bolloré Group in France, and SSBs just started to be commercialized, and some patience is still advised. Because CSEs are heterogeneous mixtures of solid phases, a modification by homogeneous or heterogeneous doping can improve their ionic conductivity [108]. The homogeneous doping involves uniform dissolution of a certain amount of aliovalent dopant in the bulk of the ionic conductor in order to increase the concentration of mobile Li+, according to bulk defect equilibrium; the heterogeneous doping involves mixing the second phase with limited solid solubility and the formation of defect concentration in the proximity of interfaces [109]. The deviations from the local electrical neutrality (space charges) are a consequence of point defect equilibrium at interfaces. Apart from the improvement of the electrical properties, the development of conductivity and ionic transference number can also be improved. The calculation of the conductivity of a two-phase mixture, e.g., an ionic conductor/matrix composite, requires the simplification of the distribution

topology, because there is a complex superposition of various transport pathways through both bulk and interfaces.

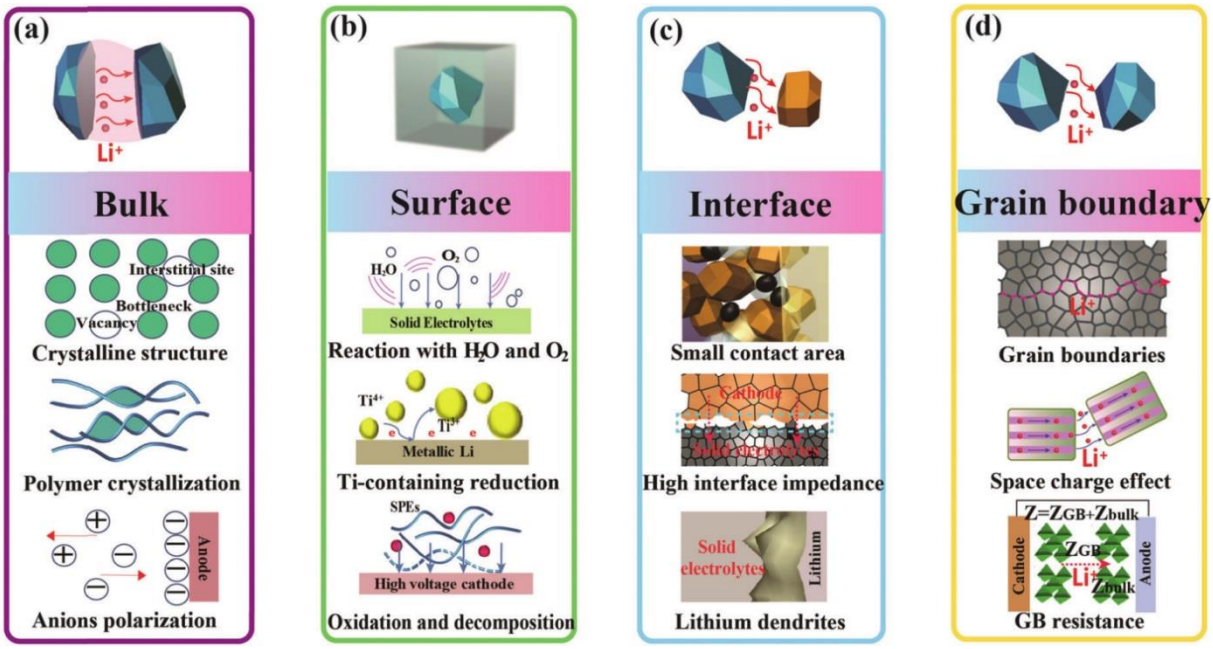

Figure 2.9. Schematic diagram of four type resistances: bulk resistance (a), surface resistance (b), interface resistance (c) and grain boundary resistance (d), ref. [61]*, copyright (2016).*

In the space charge mechanism, ions can be trapped at the interface of ceramic SE, the counter ions are then accumulated in the adjacent space charge regions. Driving force is the chemical affinity of the second phase to the trapped ion, and the space charge layer is a natural extension of volume defect thermodynamics [107]. In the complementary percolation mechanism, two thresholds of filler exist in the CSE [108][109]: below the first threshold the space charge regions are isolated in the matrix and do not contribute to ionic conductivity enhancement effectively. The conductivity increases drastically with further increase in filler content, here it is the first threshold. After enlarging volume fractions of fillers, conduction paths are disrupted by the second phase, where the second threshold is achieved.

Interfaces play an important role in ionic transportation of polyphase electrolytes. Interfaces can work as either transport pathways or barriers, given their modified core structure. As we know, the low ionic conductivity is the major obstacle for commercial applications of SEs. It originates from their poor wettability and high interface resistance with electrodes. In Figure 2.9, four types of resistances can be observed: bulk resistance, surface resistance, interface resistance and grain boundary resistance [65]. In detail, the bulk resistance is not a limiting factor of ion migration.

When exposed to air or moisture, side-reactions occur on the surface of sulfide-type and oxide-type SEs [110]. The electrochemical reduction of Ti^{4+} to Ti^{3+} in LATP and LLT also occurs during contact with metallic lithium [111]. These side-reactions account for the formation of resistive surface and the increase of surface resistance. The interface resistance between SEs and electrodes is ascribed to the poor wettability and varied thermal expansion during longtime cycling, especially for crystalline materials [112]. It is notable that surface inhomogeneity can disturb the current distribution and accelerate the growth of Li dendrite [113]. Grain boundaries can greatly block ion migration especially in oxide-type SEs, resulting in a large grain boundary resistance, while the softer sulfide-type SEs display relatively higher ionic conductivity due to their deformability [23].

2.5 Content of the thesis

Despite massive efforts devoted to improving the SEs, some issues like low ionic conductivity still block their commercialization [61,94]. Therefore, further attempts to find the optimal SEs and battery configurations were performed and discussed in the thesis.

In the first part, garnet fillers are incorporated into PEO matrix as a sort of amorphous solvent. The synergistic effect associated with garnet and polymer electrolytes can maximize the mechanical strengths and wettability. An empirical equation is proposed to simulate the relationship between volume fraction and weight fraction, and 6.71 vol.% (37.50 wt.%) LLZ dispersed in PEO-$LiClO_4$ matrix shows a great improvement in ionic conductivity (~1.56×10^{-4} S cm^{-1} at 45 °C), thermal stability (≥ 355 °C) and cycling reversibility (≥ 950 h). The results indicate that Li^+ migration pathways rely on the LLZ fraction and amorphous phase in the CSE. A passivation layer formed between solid electrolyte and electrodes can reduce interface resistance and contribute to reversible Li storage and dendrite-free cycling. The CSE was also assembled with NCM cathode and Li anode for the SSB, delivering an intermediate capacity of ~120 mAh g^{-1} at C/25 and at 45 °C.

In the second part, given the strong lithium solvation and coordination between Li^+ and ether oxygen, PEO was widely utilized as the matrix of the CSEs; but ionic transfer is limited in the semicrystalline domains. Thus, a crosslinked glycol was constructed by Bisphenol A and glyme block polymer to substitute PEO matrix with improved amorphous content and free volume, which can provide sufficient Li^+ pathways through the polymer, working as Li^+ carriers and separators.

The crosslinked matrix has excellent contact and affinity with electrodes, exhibiting high chemical stability, high ionic conductivity, and superior electrochemical performance.

In the third part, the cubic LLZ phase has high free energy due to short Li–Li distances, which can destabilize the cubic phase at RT. In order to achieve a stable cubic phase, a series of Fe_2O_3 doped LLZs are prepared via solid-state reaction. The results confirm that Fe^{3+} doping can decrease the sintering temperature for the cubic phase and repress Li loss. The particle size of LLZ grains can suddenly grow above 1030 ℃. 0.16 Fe per formula unit (pfu) doping is the most suitable to stabilize the cubic phase during high-temperature (HT) sintering and to obtain high total ionic conductivity (1.99×10^{-5} S cm^{-1} at 45 °C). In combination with a soft PSE, the assembled SSBs demonstrated a sufficient wettability and a moderate specific capacity.

Chapter 3 Experimental method

3.1 scanning electron microscope

The scanning electron microscope (SEM) machine normally consists of three components: a vacuum system, an electron beam system, and an imaging system, as depicted in Figure 3.1. An SEM produces images by scanning the sample surface with a focused beam of electrons in a raster scan pattern. Then the primary electrons interact with specimen atoms, producing the secondary electrons ejected from the *K*-shell (< 50 eV) of the atoms close to the sample surface, with reflected/back-scattered electrons, characteristic X-rays and cathodoluminescence. Because the secondary electrons contain information about the sample's surface topography and composition, the beam's position combined with the detected signal is mostly used to produce a high-resolution image (less than 1 nm in size).

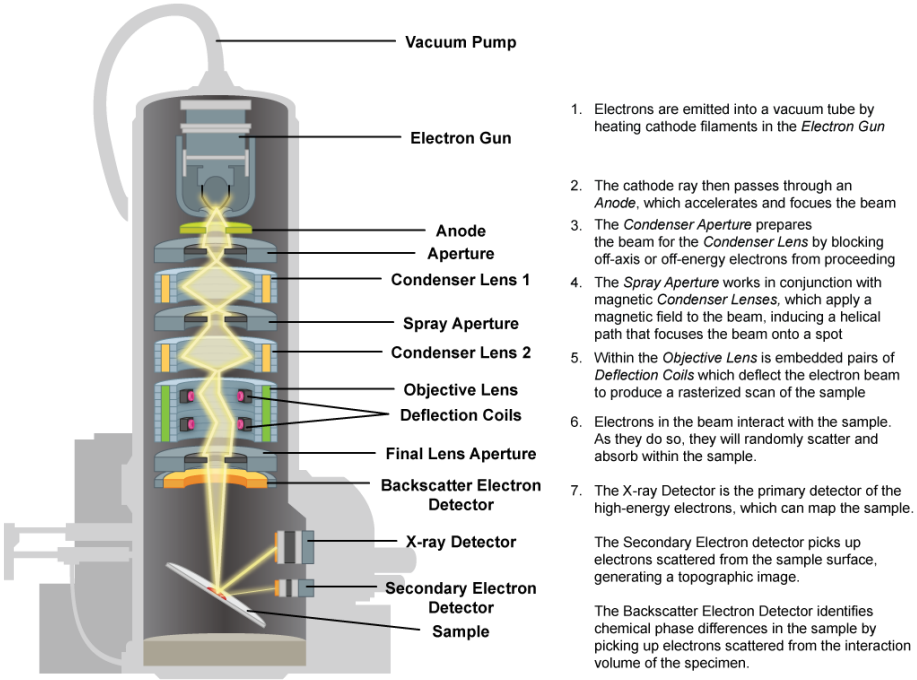

Figure 3.1. Schematic setup of an SEM. Scanning Electron Microscope Mechanism. Open access under Aleia Kim, http:|aleiakim.com/.

When the electron beam hits the sample and transfers part of its energy to the atoms of the sample. This energy can be used by the electrons of the atoms to “jump” to an energy shell with higher energy or be knocked-off from the atom. The released characteristic X-rays has energy which is characteristic of the energy difference between these two shells. It depends on the atomic unique number, therefore X-rays are a “fingerprint” of each element and can be used to identify the type

of elements in a sample. In this thesis, the morphology of samples was investigated by a Zeiss Supra 55 SEM and a Zeiss Merlin SEM. To determine the elemental distribution of samples, energy-dispersive X-ray spectroscopy (EDX) were taken with a Bruker XFlash (60 mm^2) detector.

3.2 X-ray powder diffraction

X-ray powder diffraction (XRD) is a rapid analytical technique for phase identification of a crystalline material with information about unit cell structure. The monochromatic X-rays are generated by a cathode ray tube, filtered to produce monochromatic radiation, collimated to concentrate, and directed toward the crystal, producing scattered beams loaded a detector, these beams make a diffraction pattern of spot rings; the strengths and angles of these beams are recorded, satisfying Bragg's Law ($n\lambda = 2d\ sin\ \theta$, see Figure 3.2). This law relates the wavelength of electromagnetic radiation to the diffraction angle and lattice spacing in a crystalline sample. These detected diffracted X-rays are processed and calculated. By scanning the sample through a range of 2θ angles, all possible diffraction directions of the lattice should be attained due to the random orientation of the powder sample. Conversion of the diffraction peaks to d-spacings allows identification of the crystal due to its unique *d*-spacing.

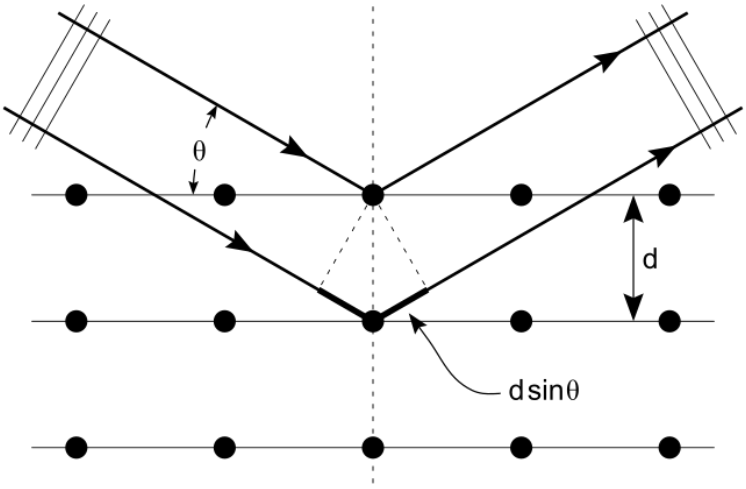

Figure 3.2. Geometry for the interference of a wave scattered from two atoms.

There are two major X-ray sources in this thesis. One is in-house X-ray powder diffractometer, which bombards a metal target (Mo $K_{\alpha 1}$ radiation (λ=0.70932 Å) or Co K_{α} radiation (λ=1.78896 Å)) with high-energy electrons to generate X-rays; the other one is the usage of the synchrotron radiation X-ray (Petra III, DESY in Hamburg).

3.3 Pair distribution function

Bragg law can theoretically and experimentally reveal their microscopic arrangement in crystal materials. However, one prerequisite for Bragg law is the periodicity of the structure. When the particles are nanosized (only over a few nanometers) or amorphous, Bragg law is not available, and this can be explained by Scherrer equation ($\tau = K\lambda/(\beta cos\theta)$, τ is the mean size of the ordered crystalline domains, K is a dimensionless shape factor, λ is the X-ray wavelength, β is the line broadening at half the maximum intensity (FWHM), θ is the Bragg angle). In contrast, the pair distribution function (PDF) is a powerful method that yields structural information at the nanoscale to determine all the atomic positions at the short, medium or long-range order of materials. The method can be applied to crystalline and amorphous solid material as well as to liquids. In the PDF analysis, XRD data is analyzed by the reduced structure factor, F(Q) = Q[S(Q)-1], and is converted by Fourier transform of the scattering intensity to a reduced pair distribution function according to Eq. 3.1 through a PDFgetx2 software [114]:

$$G(r) = 4\pi r[\rho(r) - \rho 0] = \frac{2}{\pi}\int_0^\infty Q[S(Q) - 1]\sin(Qr)dQ \qquad \text{(Eq. 3.1)}$$

where ρ(r) is the atomic pair density, ρ0 is the average atomic number density, r is the interatomic distance, S(Q) is the total scattering function and Q is the momentum transfer vector [115].

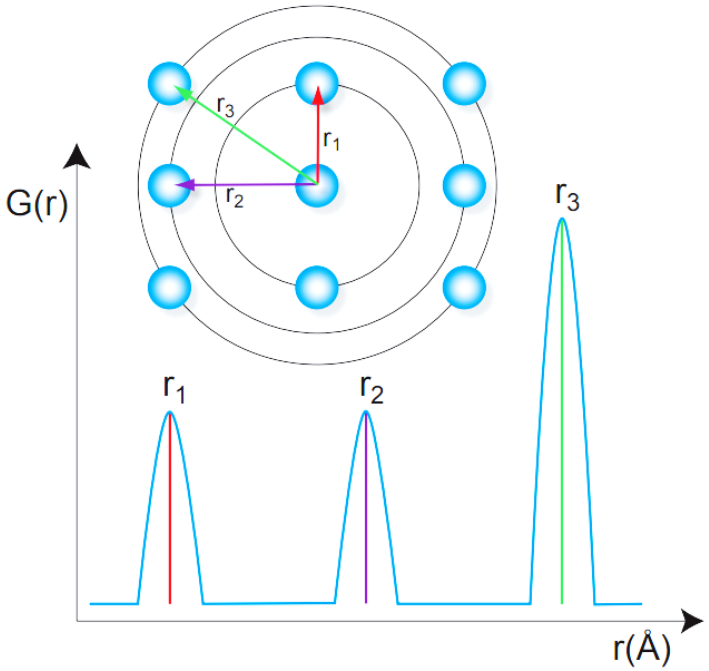

Figure 3.3. The principle of the PDF: inter-atomic distances r_i cause maxima in the PDF G(r). The area below the peaks corresponds to the number of neighbors, scaled by the scattering power of the respective atoms (sources: Bruker AXS GmbH).

Instrument dependent parameters, *i.e.*, Q_{damp} and Q_{broad}, were determined by fitting the *ex-situ* PDF data of LaB_6 standard. The PDF data were optimized to span a wide Q-range (~24 Å), as

required for quantitative analysis with high real-space resolution. Total X-ray scattering diffraction (T-XRD) data of the samples were collected at the beamline P02.2 PETRA III (DESY, Hamburg). A two-dimensional image of the T-XRD was subjected to geometrically corrected integration and reduced to one dimensional XRD patterns. In order to discuss detail local structure, PDF fitting analysis was performed via PDFgui software to get G_{calc} (r) and to match the G_{trunc} (r) [116].

3.3 Fourier-transform infrared spectroscopy

Fourier-transform infrared spectroscopy (FTIR) is an analytical technique used to identify functional groups via an infrared spectrum of absorption or emission from the sample. An infrared spectrum is commonly obtained by passing infrared radiation through the sample and determining what fraction of the incident radiation is absorbe with a particular energy. Different functional groups in a molecule can bend, stretch or wag at certain frequencies, the molecule will absorb the infrared radiation only if the frequency of the incident radiation matches the specific frequency of the functional group. Therefore, absorption bands in IR spectra enable to determine the present functional groups. In this work, a Bruker Tensor 27 Fourier transform infrared spectroscopy (FT-IR) spectrometer was used to collect data from 4000 ~ 400 cm^{-1}.

3.4 Cyclic voltammetry

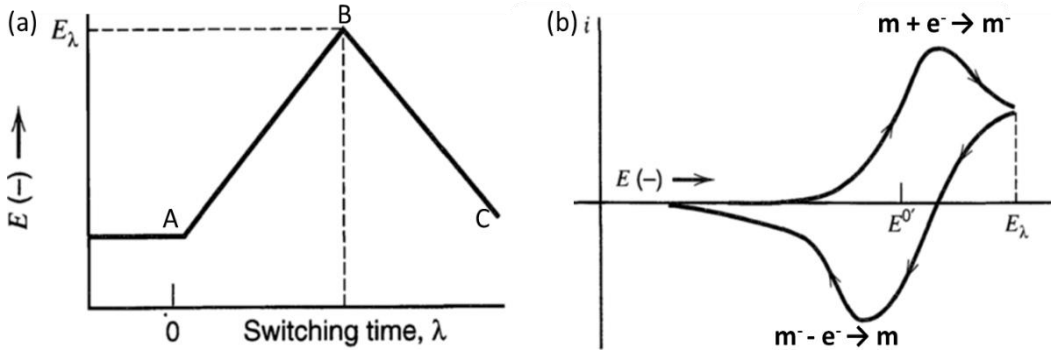

Figure 3.4. (a) The electrode potential ramps linearly vs. time in cyclical states, (b) a typical cyclic voltammogram.

Cyclic voltammetry (CV) is a type of potentiodynamic electrochemical scan. It is generally used to investigate the electrochemical redox reaction of an electrode. The potential of the working electrode is measured against a reference electrode which maintains a constant potential, and the applied potential produces an excitation signal (oxidation or reduction current peaks). The cathodic current (i_{pc}) can be estimated when the cathodic potential scan (e_{pc}) goes towards negative direction, where the reduction occurs ($m + e^- \rightarrow m^-$). Figure 3.4 shows a typical reduction occurring from A to B where the potential scans positively, and a reverse oxidation from B to C where the potential

scans negatively. The slope of the excitation signal gives the scan rate. Linear sweep voltammetry is similar to the cyclic voltammetry technique, but the scanning on the electrode is not inverted afterward. It is often used to test the electrochemical stability windows of the electrodes.

3.5 Electrochemical impedance spectroscopy

Electrochemical impedance spectroscopy (EIS) is an experimental method of characterizing electrochemical systems excited by a small amplitude *ac* sinusoidal signal of potential over a range of frequencies (10^6~10^{-2} Hz). Since the amplitude of the excitation signal is small enough for the system in the (quasi-)equilibrium state, EIS method can effectively evaluate the capacitive behavior, charge transfer, and ion diffusion. The EIS data are normally expressed graphically in Bode plot or Nyquist plot (Figure 3.5), and actual EIS response can be modeled as a network of passive electrical circuit elements, namely equivalent circuit. Each element, *i.e.*, Warburg impedance, constant phase element, resistor, and capacitor in the equivalent circuit should correspond to some specific electrochemical activity.

For example, resistance is often a significant factor in a cell, which depends on the ionic concentration, ion species, working temperature, and surface geometry. The total conductivity σ_t was calculated based on the equation $\sigma_t = l/A \bullet R_t$, where l, A and R_t are the average thickness (cm), surface area (cm^2) and total resistance (Ω) of the electrode, respectively.

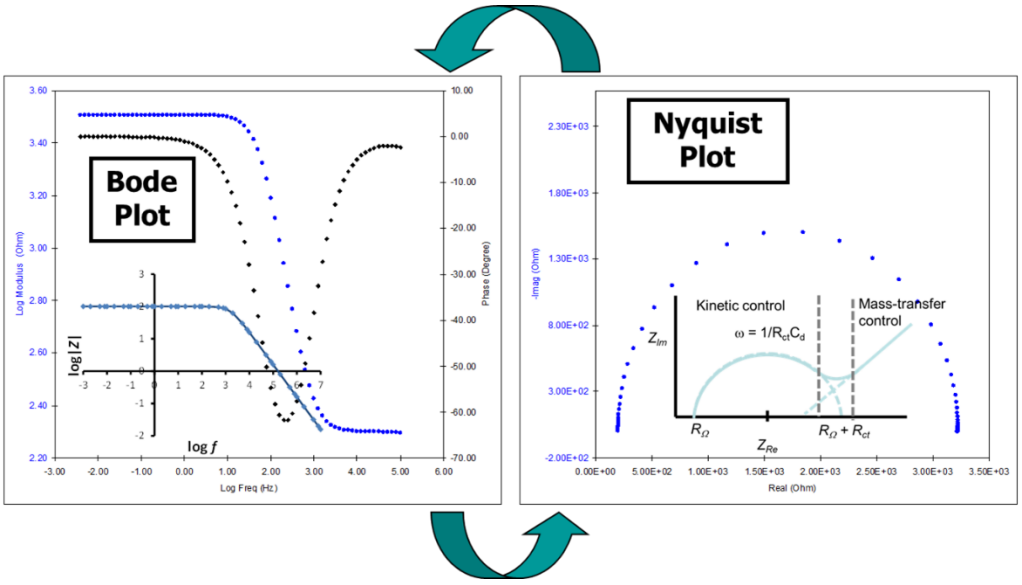

Figure 3.5. EIS response of ac frequency in an electrochemists Bode and Nyquist diagram.

3.6 Galvanostatic cycling

The galvanostatic cycling technique is widely applied for energy storage characterization. In the galvanostatic mode, a controlled current density (A g^{-1}) is applied between the working electrode and the counter electrode, and the generating potential between the working electrode and reference electrode is monitored. In a two-electrode system, the potential is measured across the full cell, which responds to contribution from the electrode/electrolyte interface and the electrode itself. Therefore, the electrochemical capacity behavior of the whole cell is under investigation.

In this thesis, all cells were built in an argon-filled glovebox (MB200, Mbraun GmbH) and aged for 2 h prior to measuring cells kept in a climate chamber (M53, Binder GmbH). All the electrochemical tests were performed utilizing a multichannel potentiostat system (VMP3, Bio-Logic).

3.7 Nuclear magnetic resonance

For nuclear magnetic resonance (NMR) measurements a sample is placed in a magnetic field while the nuclei of the sample absorb and re-emit electromagnetic radiation. This energy is at a specific resonance frequency which depends on the strength of the magnetic field and the magnetic properties of the atoms. All isotopes that contain an odd number of protons and/or neutrons have an intrinsic magnetic moment and angular momentum, while all nuclides with even numbers have total spin of zero. The most generally studied nuclei are ^{1}H, ^{6}Li and ^{13}C with high-field NMR spectroscopy.

The relaxation describes signals deteriorate with time, that gradually becomes weaker and broader, suggesting that the NMR signal arises from the over-population of an excited state. In other words, relaxation describes how quickly spins "forget" the direction in which they are oriented. A set of basic pulsed field gradient (PFG)-NMR sequences are provided for active nuclei, along with their corresponding echo attenuations, the nuclear magnetic moment will align along the direction of this field. The usual way to conduct the diffusion experiment is to fix the durations and to vary the applied magnetic field gradients, so that the reduction of the NMR echo signal will be constant due to transverse and longitudinal relaxation processes. In this thesis, PFG-NMR spectra were measured on a Bruker Avance 300 MHz spectrometer equipped with a Diff 50 probe, which produces pulsed-field gradients up to 3000 G cm^{-1}.

Chapter 4 Garnet-polymer composite solid electrolyte

4.1 Introduction

Safety is a major concern for commercial batteries, because dendrite penetration, severe crash, and overcharge may trigger exothermic reactions which can cause fire or explosion. To improve the safety properties, solid electrolytes (SEs) and solid state batteries (SSBs) were proposed to replace the polymer separators/liquid electrolytes [117–120]. Moreover, SEs enable high-voltage cathodes, metallic lithium anode and series-packing, which enhance overall energy density [16,121]. With the number of studies growing rapidly, researchers have realized that the major challenge of SSBs is low ionic conductivity due to high interface resistance at room temperature (RT) [25,122]. In general, SEs fall into three categories according to the backbone elements: oxide, sulfide and polymer. Compared to highly reactive sulfide-based electrolytes, Li-rich garnet oxide $Li_7La_3Zr_2O_{12}$ (LLZ) is remarkably stable in contrast with a Li anode. Further garnet type electrolytes possess high bulk conductivity (~10^{-4} S cm^{-1} at RT), low cost (*e.g.*, no Ge), wide potential window (> 5 V *vs.* Li/Li^+) and superior thermal stability [123–126]. However, intrinsically brittle garnet pellets are difficult to integrate into full batteries [30,122,127,128].

Due to its high donor number to trap Li^+ ions, high dielectric constant and strong Li^+ solvating ability, PEO is also intensively studied to be used in polymer electrolytes, but polymer electrolytes are associated with some problems such as: low conductivities (10^{-6} ~10^{-8} S cm^{-1} at RT), low ionic transfer number (0.2 ~ 0.5), unwanted chemical reaction with electrodes, and poor mechanical strength that cannot impede dendrite penetration [129–131]. To solve these issues, active fillers were incorporated into the PEO matrix, and different from the inert fillers (*i.e.*, TiO_2, SiO_2 and Al_2O_3), active fillers (*i.e.*, super ion conductors) can not only improve mechanical stability, but also offer extra Li sources [95–98]. The interaction of PEO with the filler can also improve mechanical strength and wettability of Li anode [106]. Thus, the optimal engineering of composite solid electrolytes (CSEs) is an effective strategy that may lead to high-performance SSBs, but it lacks the study on the optimal thresholds based on percolation mechanism.

Herein, in order to find the correlations between ion migration and the composite phase in the CSEs, rigid-flexible CSEs with varying LLZ contents (0 ~ 64.24vol.%/93.75 wt.%) were prepared via the gel-casting method. X-ray powder diffraction (XRD), scanning electron microscopy (SEM),

cyclic voltammetry (CV) and lithium striping/plating cycling were used to characterize the CSE films. The motion of charge carriers in the amorphous phase was examined through electrochemical impedance spectroscopy (EIS) and pulsed-field gradient-nuclear magnetic resonance (PFG-NMR). A $LiNi_{1/3}Co_{1/3}Mn_{1/3}O_2$|CSE|Li full cell was assembled to evaluate cycling performance and resistance evaluation, and the information gained in this study is useful for further structural modification of lithium-metal batteries.

4.2 Experimental section

4.2.1 Preparation of the LLZ/PEO CSE film

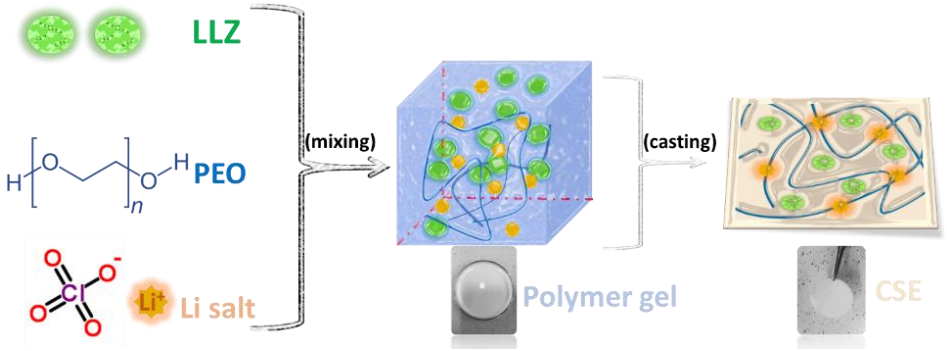

Figure 4.1. Preparation schematic of the CSE film via the gel-casting process.

Figure 4.1 depicts a typical gel-casting preparation, commercial LLZ powder (particle size: 743±194 nm, NEI Corporation, phase purity shown in Figure 4.S1), PEO powder ($M_w = 5\times10^6$, Sigma-Aldrich) and $LiClO_4$ (purity ≥ 99.9 wt.%, Aldrich, (EO)/Li^+ = 8 in molar) were stepwise added in Dimethylcarbonate (DMC, gel chromatography purity ≥ 99.0%, Merck KGaA) and stirred at 1200 rpm for 12 h at 80 ℃. After degassing, the gel was cast into a watch glass (ϕ70 mm). After evaporating the solvent, the films were dissolved in DMC again to repeat the casting process. The as-obtained CSE films were labeled LP*x*, *x* refers to LLZ content (wt.%) in the CSEs. For comparison, a pure PEO film without any additive was also prepared in the same process.

4.2.2 Preparation of the $LiNi_{1/3}Co_{1/3}Mn_{1/3}O_2$ cathode

$LiNi_{1/3}Co_{1/3}Mn_{1/3}O_2$ (NCM) was prepared by a hydroxide co-precipitation method described by Hua *et al.* [132]. Firstly, a solution containing Ni, Co, Mn ions at a molar ratio of 1:1:1 was pumped into a reactor, and 4 M NaOH and 10 M $NH_3{\cdot}H_2O$ solutions were synchronously added to the reactor remaining at a stable pH value of around 11.5. The co-precipitation reaction was controlled at 52 ℃ under nitrogen atmosphere. The collected precipitate was washed and dried at 110 ℃ for 12 h. The resultant powder was mixed with Li_2CO_3 and calcined at 850 ℃ for 12 h to obtain the

NCM material (phase purity shown in Figure 4.S2). Afterwards, homogeneous cathode slurry was prepared by mixing NCM powder, polyvinylidene difluoride (R6020/1001, Solvay), carbon black (Super-C65, Timcal Ltd.) and LLZ at a weight ratio of 8: 1: 0.8: 0.2. The slurry was coated on Al foil using a laboratory coater (Erichsen GmbH), following drying at 80 ℃ and cutting into ϕ12 mm disks.

4.2.3 Electrochemical evaluation of the CSE film

A CSE film (ϕ12 mm) sandwiched between two stainless steel cylinders (SSs) was assembled into Swagelok® cells. The EIS tests were carried out for ionic conductivity over a frequency range of 10^{-1}~10^{6} Hz in sinus amplitude of 10 mV at the cooling- and heating process (55 °C→5 °C→55 °C). The impedance spectra were fitted using ZsimpWin software (Ametek. Inc.), and the total conductivity σ_t was calculated based on the equation $\sigma_t = l/(A \cdot R_t)$, where l, A and R_t are the average thickness (cm), electrode area (cm^2) and total resistance (Ω) of the CSE film, respectively. Linear sweep voltammetry from 2.0 V *vs.* Li/Li^+ was performed at a scan rate of 1 mV s^{-1} in Swagelok® cells (glassy carbon|CSE|Li) to determine the electrochemical stable window. Galvanostatic stripping/plating using Li symmetrical cells was also performed at current densities of 10 μA cm^{-2} for 10 h, 20 μA cm^{-2} for 5 h, 50 μA cm^{-2} for 2 h and 10 μA cm^{-2} for 5 h to investigate Li^+ solubility in the CSE film. The cathode foil (ϕ12 mm), CSE film (ϕ16 mm) and Li foil (ϕ12 mm, Alfa Aesar) were assembled into a CR2032 cell under the pressure of 9.5 MPa, labeled PLP*x*, *x* refers to LLZ content (wt.%). All cells were built in an argon-filled glovebox (MB200, Mbraun GmbH) and aged in an oven at 80 ℃ to ensure cell parts were closely packed. Prior to measuring the cells kept in a climate chamber (M53, Binder GmbH) at the setting temperature for 30 min. Except for EIS measurement, the electrochemical tests were performed at 45 °C utilizing a multichannel potentiostat (VMP3, Bio-Logic) at 2.5~4.3 V (vs. Li/Li^+). For comparison of assembling method, as-prepared hybrid gel as stated in Section 4.2.1 was directly coated on the NCM foil and then assembled into a full cell, labeled CLP*x*.

4.2.4 General characterization

X-ray diffraction (XRD) was carried out using an STOE STADI P X-ray powder diffractometer equipped with a Mythen1K detector, and Cu $K_{\alpha 1}$ radiation (λ=1.54056 Å) or Co K_α radiation (λ=1.78896 Å) to characterize the crystalline structure. In order to determine the distribution of garnet fillers embedded in the PEO matrix, CSE films were in advance polished for 9 h by a triple

ion-beam cutter system (EM TIC-3X, Leica-Microsystems) using argon as working gas to obtain a smooth cross section. The morphology of as-polished samples was investigated by a scanning electron microscope (SEM, Supra 55, Zeiss GmbH). To determine the elemental distribution in the CLP electrode, energy-dispersive X-ray spectroscopy (EDX) data was taken with a Bruker XFlash (60 mm^2) detector combined with a Zeiss Merlin SEM. Thermogravimetry (TG) and differential scanning calorimetry (DSC) data were collected through an STA 449C Netzsch analyzer from 35 ℃ to 800 ℃ at a heating rate of 5 ℃ min^{-1} under argon flow (42 mL min^{-1}). Raman measurement was performed with a Raman spectrometer (LabRam Evolution HR, HORIBA Jobin Yvon) using 632 nm laser excitation with a power of 10 mW.

PFG-NMR spectra were measured on a Bruker Avance 300 MHz spectrometer equipped with a Diff 50 probe, which produces pulsed-field gradients up to 3000 G cm^{-1}. A stimulated-echo pulse sequence in combination with bipolar gradients was used to observe the echo damping as a function of gradient strength. The duration of the π/2 and π pulses varied from 27 ℃ to 57 ℃. Recycle delays in the range of 1~2.5 s were chosen on the basis of the T_1 measurement results. All delay times during each PFG-NMR experiment were kept constant, whereas the gradient amplitude was varied to cause the signal decay, then the influence of relaxation on the echo decay was eliminated. The optimal values for the gradient duration δ and the diffusion time Δ were determined to be 3~3.5 and 100~150 ms, respectively. In total 16 points were acquired to form each diffusion decay, and each point was sampled with 64 scans.

4.3 Results and discussion

4.3.1 The relation of wt.% *vs.* vol.%

Since Li^+ ions prefer to go through the amorphous PEO phase, rather than crystalline phase alone [133,134], thus enough LLZ fillers dispersed in the PEO matrix can form sufficient long-range Li^+ pathways via percolation effect. Generally speaking, the amount of LLZ fillers is dosed gravimetrically and expressed as mass ratio when discussing filler contents. This is because the mass ratio is easy to calculate by respective raw components. However, it lacks of direct correlation between certain properties of the CSEs and mass ratio of fillers. Weakly bonded Li^+ ions creep along flexible polymer chains in the amorphous phase during cycling [135,136]. Therefore, ionic conductivities of physical blended CSEs should correlate with volume ratio of fillers [137]. In order to find the relationship between mass ratio (wt.%, $R_{(m.LLZ)}$) and volume ratio (vol.%, $R_{(v.LLZ)}$),

typical cross-sectional overviews of CSE films (LP6.25, LP37.5 and LP68.75) were shown in Figure 4.2, where the polymer phase appears dark, whereas the white areas correspond to the embedded LLZ fillers. The higher the LLZ content, the wider the distributtion of the filler, with neither voids nor gaps being observed around the fillers.

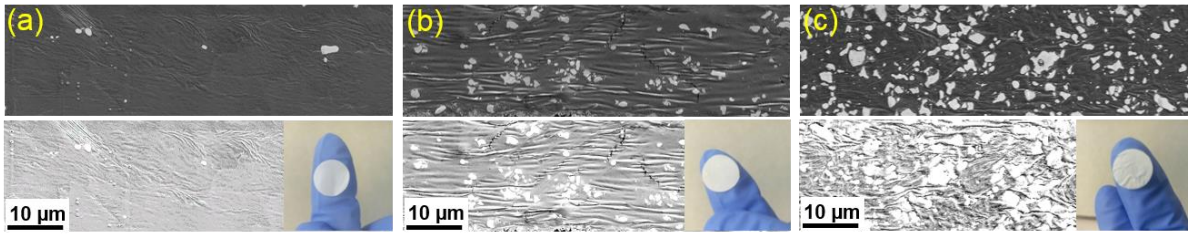

Figure 4.2. SEM and corresponding high brightness of images of the CSE films: LP6.25 (a), LP37.50 (b) and LP68.75 (c), the insert images are the digital pictures.

In this study, a theoretical equation ($Eq_{.th}$) based on the measured densities [138,139] ($\rho_{(PEO)}$= 1.29 g cm^{-3} and $\rho_{(LLZ)}$ = 5.43 g cm^{-3}) was proposed:

$$R_{(v.LLZ)} = \frac{R_{(m.LLZ)}/\rho_{(LLZ)}}{R_{(m.LLZ)}/\rho_{(LLZ)} + (1 - R_{(m.LLZ)}/\rho_{(PEO)})} = \frac{0.22R_{(m.LLZ)}}{0.93 - 0.71R_{(m.LLZ)}} \qquad Eq_{.th}$$

Based on the analysis of the SEM images (see Figure 4.S3) via ImageJ software, area ratios of the fillers are ~0.84%, ~6.71% and ~20.81% for the LP6.25, LP37.50 and LP68.75, respectively. Analogous to liquid mixation, inorganic fillers blending polymer matrix gives a reduced total volume compared to the mathematical sum of each volume. In theory, a single CSE film can be divided into infinite cross-sectional layers. Area ratio in each infinitely thin layer can be simplified to be equal to the volume ratio of the LLZ ($R_{(v.LLZ)}$) because the filler size is far smaller than the total thickness of the CSE film. Combined with negative inverse proportional function $Eq_{.th}$ and ImageJ analysis, an empirical equation ($Eq_{.em}$) is proposed to describe the actual relationship between $R_{(m.LLZ)}$ and $R_{(v.LLZ)}$. Figure 4.3 depicts function equation curves of $Eq_{.th}$ and $Eq_{.em}$, here one can observe that the $R_{(m.LLZ)}$ from $Eq_{.th}$ is much closer to the $R_{(v.LLZ)}$ from $Eq_{.em}$. The blue pots (area ratios of the LLZ fillers) obtained from analysis of crosssectional images agree well with the $q_{.th}$ curve, which confirms a good fitting result, and it is surprising that the majority of $R_{(v.LLZ)}$ constitutes less than 26.50 vol.% (corresponding to 81.25 wt.%).

$$R_{(v.LLZ)} = \frac{0.22R_{(m.LLZ)}}{1.83 - 1.62R_{(m.LLZ)}} \qquad Eq_{.em}$$

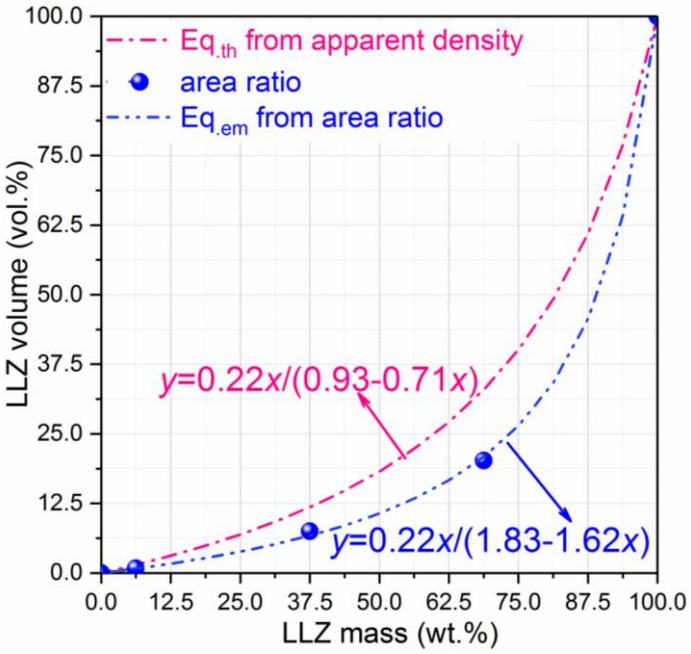

Figure 4.3. The relationship between mass ratio (wt.%, $R_{(m.LLZ)}$) and volume ratio (vol.%, $R_{(v.LLZ)}$), expressed by the theorical equation ($Eq_{.th}$) and the empirical equation ($Eq_{.em}$).

4.3.2 Ionic migration

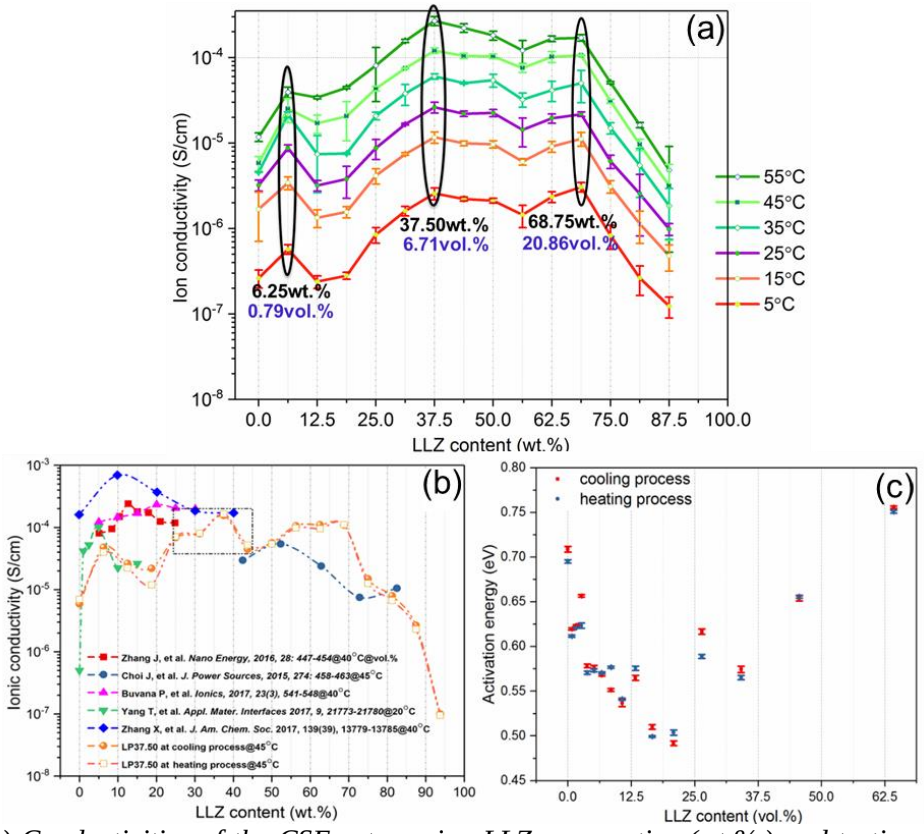

Figure 4.4. (a) Conductivities of the CSEs at varying LLZ mass ratios (wt.%,) and testing temperatures. Each data point is an average of at least three battery cells with very small deviations to ensure reproducibility; (b) Ionic conductivity of the LP37.50 as a function of LLZ contents at 45 ℃ and related

reports: Zhang et al. LLZTa content range of 5~25 vol.%, optimal value = 12.7 vol.% [119]; Choi et al. LLZ content range of 42.5~82.5 wt.%, optimal value = 52.5 wt.% [95]; Buvana et al. LLBaTa content range of 5~30 wt.%, optimal value = 20 wt.% [140]; Yang et al. LLZ content range of 0~15 wt.%, optimal value = 5 wt.% [141]; Zhang et al. LLZTa content range of 0~40 wt.%, optimal value = 10 wt.% [103]; (c) Activation energy of the CSE films at varying LLZ contents (vol.%).

Ion conductivity is the most fundamental quality of electrolyte materials, and EIS is a powerful technique of its evaluation. Based on data analysis and previous reports, three equivalent circuits are proposed for data fitting (see Figure 4.S4) [106,133–135,142]. Ionic conductivities as a function of $R_{(v.LLZ)}$ obtained from $Eq_{.em}$ and $R_{(m.LLZ)}$ are depicted in Figure 4.4a. At the same LLZ content, ion transfer can be thermally activated by elevated temperature, and transient mobility can be enhanced by enlarging free volume of the polymer matrix. Thus, higher ionic conductivity can be achieved at elevated temperature. At same temperature the high conductivity is achieved at the medium mass ratio of LLZ fillers. In Figure 4.4b, ionic conductivities of the CSEs is mostly higher than during the inverse heating process from 55 ℃ to 5 ℃, except the LLZ contents of 6.71~8.52vol.% (or 37.5~43.75 wt.%, marked by black rectangle, see). This is associated with the recrystallization process of polymer matrix over a wide time scale, which is also related to the thermal history and the free volume of the matrix [141,143]. Similarly to previous reports on polymer electrolyte, the PL0.00 delivers a low ionic conductivity of 5.87×10^{-6} S cm^{-1} [80,144]. For reference, reported optimal filler contents (mostly expressed as weight percentage) for conductivity are summarized in Figure 4.4b, suggesting that the proper LLZ contents are mainly located at ~10 wt.% and ~50 wt.%, and the maximum conductivity of the CSE films is achieved at the LP37.50 (6.71 vol.%) in this study. The result indicates that the proper combination of the polymer matrix and garnet fillers synergistically enhances the total conductivities, but massive LLZ fillers lead to a dramatic drop in the conductivity.

Not only available energy for ion migration, but also the temperature is crucial to determine segmental motion and ionic conductivity, the energy barrier of Li^+ diffusion below T_g (~60 ℃) normally follows Arrhenius law: $\sigma = \sigma_0 \exp(-E_a/RT)$ rather than Vogel-Fulcher-Tammann (VFT) law, where σ is ionic conductivity (S cm^{-1}), σ_0 is pre-exponential constant related to charge carriers, R is gas constant (8.31446 J·mol^{-1}·K^{-1}) and T is testing temperature (K) [145,146]. Figure S4.5 depicts the ionic conductivities ($\ln\sigma$) of the CSE films as functions of temperature (*1000/T*) and LLZ content (vol.%). In the cooling process, the calculated $E_a$decreases from 0.71 eV (LP0.00) to 0.62 eV (LP6.25), then further incorporation of LLZ leads to lower $E_a$values (*i.e.*, 0.56 eV for

LP37.50 and 0.48 eV for LP68.75), as shown in Figure 4.4c. This indicates that Li^+ ions overcome migration barrier easily, with moderate content LLZ added.

Herein, the LLZ filler with moderate content can effectively enhance the conductivity. Based on $\sigma = \sum n_i z_i u_i$, where n_i is number of free charged species, z_i is number of ion charges ($z = q/e$, q is electric charge, and e is elementary charge ($1.6021766208(98)\times10^{-19}$ C)), and u_i is ion mobility ($u = ez/(6\pi\eta r)$,e is elementary charge, z is number of ion charge, η is the viscosity, and r is ion radius), the ionic conducticivity is directly proportional to the concentration of charged species and their mobility. In this study, ionic conducticivity depends on the active Li^+ concentration, Li^+ mobility and Li^+ transport pathway. In order to determine the reasons behind these factors, some experiments with in-depth discussion were employed in this study:

4.3.2.1 Li^+ concentration

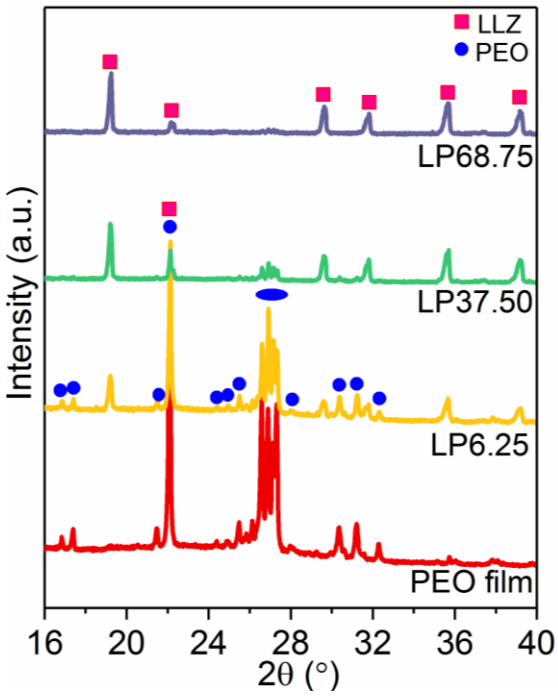

Figure 4.5. XRD patterns (Co K_α) of the pure PEO and CSE films with varying LLZ contents.

Among Li salts, $LiClO_4$ has good conductivity and electrochemical stability in the PEO-based electrolyte, and Li^+ ions prefer to dissolve in the amorphous phase based on Li^+ complexing coordination [147], so that amorphous content in the CSE can determine active Li^+ concentration. Therefore, amorphous phase evolution of the CSEs with varied LLZ contents was detected by XRD measurement at RT. In Figure 4.5, the pure PEO film displays four peaks, which is ascribed to the partial reorganization of polymer chains into crystal grains during the casting process. With more

LLZ fillers added, PEO peak intensity located at 2θ = 22.1°~27.5° gradually decreases, and characteristic peaks of the LLZ fall to appear in the XRD pattern. In detail, the low content LLZ fillers (≤ 6.71 vol.%/37.50 wt.%) can serve as nucleators to facilitate heterogeneous nucleation and form small crystal grains. In the moderate LLZ contents (8.52 ~ 16.64 vol.%/43.75 ~ 62.50 wt.%), the added fillers can limit reorganization of polymer chain and produce maximum amorphous region, evidenced by the disappearance of the PEO peaks and decrease in melting enthalpy, which is confirmed by DSC analysis (see Figure S4.6). The XRD patterns of CSEs with high LLZ contents (≥ 20.86 vol.%/68.75 wt.%) mainly display typical LLZ peaks (*i.e.*, at 2θ = 19.2°, 22.3°, 29.7° and 31.8°), and large LLZ particles can block Li^+ transport channels within the polymer. Therefore, whne blending with the moderate LLZ fillers, polymer chains can rearrange themselves disorderedly and solidify radially around fillers with high amorphous status, indicating a high dissolubility for Li^+. It is well known that fillers can reduce the crystallinity of PEO. Furthermore, the fillers containing Li can be an additional Li^+ source participating in conduction, and the decomposed LLZ can enlarge Li^+ concentration, which can improve the ionic conductivity compared to the inert organic filler like Al_2O_3 (see Figure S4.7) [140,148–150]. However, the excessive LLZ fillers are diluted and separated by PEO result in much lower ionic conductivity, because massive LLZ fillers confine the motion of the Li salts owing to the high interface resistance.

4.3.2.2 Li^+ mobility

PFG-NMR diffusion experiments provide reliable information on the long-range transport of the Li^+ ions (the distance of ions path at RT is ca. 0.5 mm). In this work, we measured diffusion-caused damping of the signal intensity as a function of temperature in the range of 300~340 K with a step of 10 K (see Figure 4.6). The decays obeyed single Gaussian behavior at each temperature and a single diffusion coefficient (*D*) was obtained with the Stejskal-Tanner equation. With the increase of the LLZ fraction to 28.86 vol.% (68.75 wt.%), the ^7Li relaxation times increased in the CSE, which suggests a slowdown of Li^+ motion. Figure 4.7 depicts the changes of the Li^+ diffusion coefficient as a function of 1000/*T* showed non-Arrhenius nature at 330 K the slope altered. The LP6.25 and LP37.50 display high Li^+ diffusion coefficients, compared to that of the LP68.75. This fact indicates the enhancement of the polymer dynamics which facilitates movements of the Li^+ in the matrix. The operating temperature of the battery is close to the room temperature, thus we only considered an initial slope to define activation energy of the conductive dynamics. Figure 4.7

displays experimental diffusion data along with fitting according to the Arrhenius law: $D = D_0 \cdot \exp(-E_a/(k_b T))$. As it can be seen from the figure, 6.25% and 37.5% samples perform equally at the given temperature range, resulting in the low E_a, whereas 68.75% possesses much slower mobility with higher energy barrier.

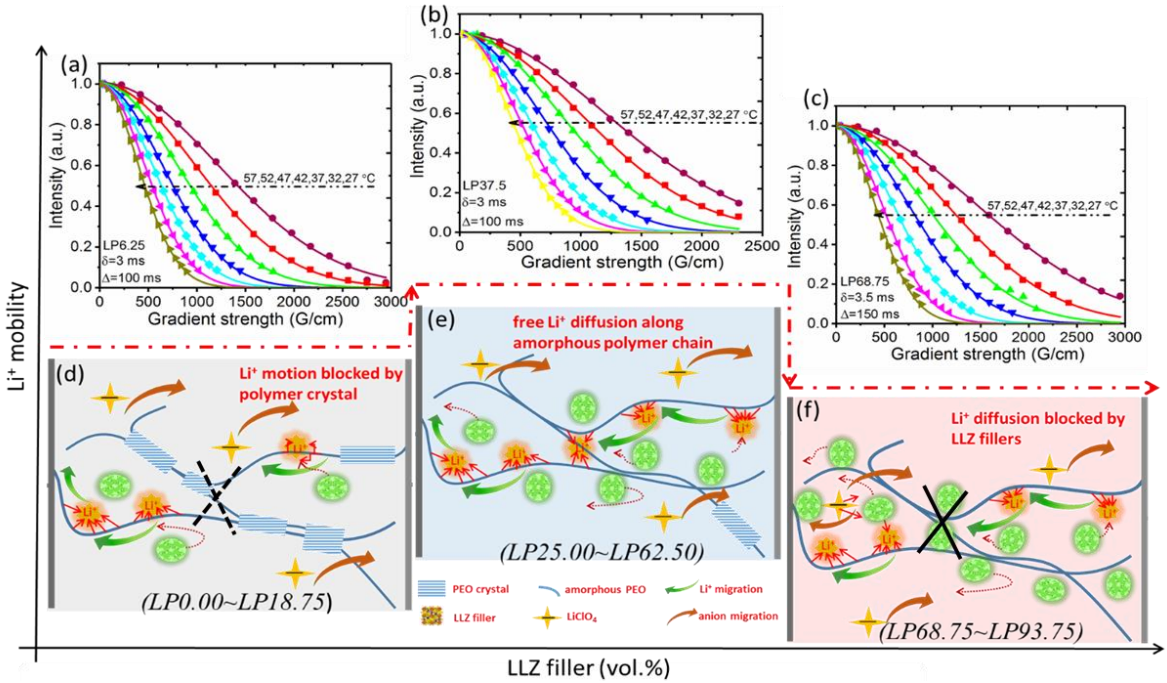

Figure 4.6. PFG-NMR result: Echo damping vs. gradient strengths of the LP6.25 (a), LP37.5 (b) and LP68.75 (c), and corresponding schematic illustration of Li^+ coordination and migration in the CSEs (d~f).

To summarize the variation of Li^+ diffusion, Figure 4.6d~f depicts the schematic illustrations of Li^+ coordination and migration in the CSEs. In the low LLZ contents (≤ 2.69 vol.%/18.75 wt.%), the CSEs behave like a polymer electrolyte modified by LLZ; and mobile Li^+ ions from $LiClO_4$ or decomposed LLZ are transiently coordinated to four ether-oxygen as Lewis bases, and Li^+ transport occurs when initial coordination link breaks and the new one forms [135,136]. However, some mobile Li^+ are blocked by crystalline grains (see Figure 4.6d) [88]. In the moderate LLZ contents (3.84~16.64 vol.%/25.00~62.50 wt.%), amorphous PEO phase reaches the maximum status, evidenced by disappearance of reflection peaks, where mobile Li^+ are easily dissolved in the CSE to enrich charge carriers, and the long-range Li^+ pathways can form along polymer chains, leading to a high ionic conductivity (see Figure 4.6e) [119,134]. When LLZ content is above 20.86 vol.% or 68.75 wt.%, their slower mobility is due to the excessive LLZ fillers blocking Li^+ transport channels within the polymer, Li^+ ions can go through the interior LLZ, but large interface resistance between LLZ fillers can hinder Li^+ transfer (see Figure 4.6f) [106,135].

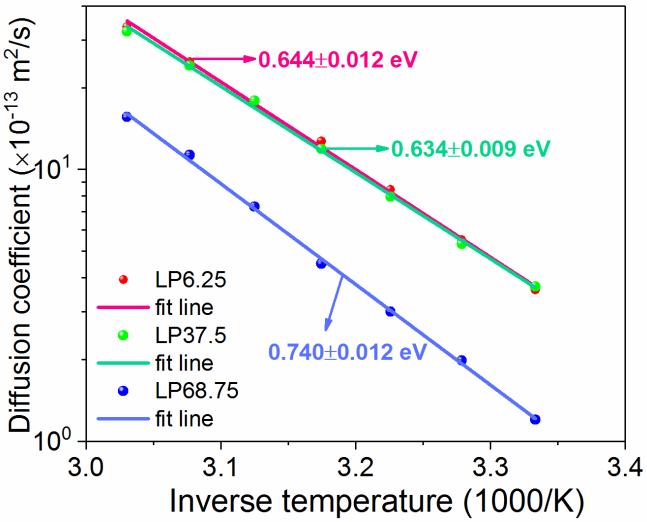

Figure 4.7. temperature-dependent Li diffusion coefficient (D_{Li}) of the CSEs and corresponding calculated activation energy.

4.3.2.3 Li^+ pathway

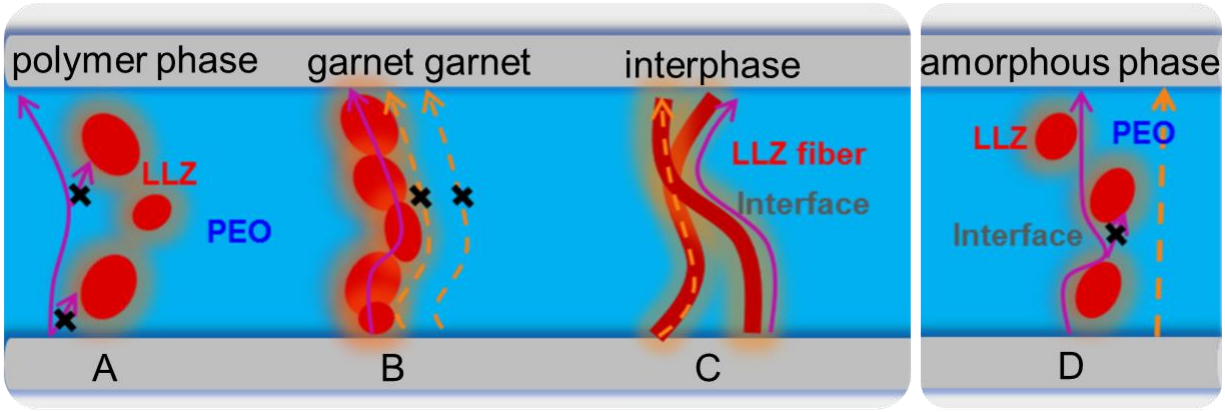

Figure 4.8. Schematic illustration of Li^+ pathways within the CSE: LLZ−PEO (Li salt))−ionic liquid based on reports and this work.

Direct tracing of the Li^+ footprint in the SE is still a challenge. M. Keller et al. [133] studied the EIS results of the LLZ/$P(EO)_{15}$LiTFSI on the cooling process, and believed that Li^+ cannot transfer through the grain boundary resistance between LLZ and PEO as well as among LLZ particles (see Figure 4.8A). Thus, Li^+ prefers to go through PEO matrix, otherwise Li^+ ions are most likely trapped at the LLZ surface in a form of LiOH and Li_2CO_3. Y. Hu's group developed the high-resolution NMR method using $^6Li \rightarrow ^7Li$ isotope replacement strategy to determine the Li^+ migration trace. NMR results show that Li^+ prefers to go through LLZ percolation network (≥ 50wt.%) with as few PEO phases as possible (see Figure 4.8B) [106]. When using LLZ electro-spun fiber (~5wt.%), Li^+ prefers to go along LLZ/PEO interphase (see Figure 4.8C) [141]. Therefore, the preferable Li pathway in the CSE depends on the filler content and morphology, and this can further correlate to the change of amorphous fraction.

In this case, the CSEs with the small size of the LLZ particles contribute to the formation of continuous amorphous polymer phase. Additionally, the particle interface itself is a disordered region, where the migration energy is generally low, leading to enhanced ionic transport within the interface (grain boundary diffusion). In the complementary percolation model, two critical filler fractions can be found in the ionic conductor/matrix composites [107]. At the first critical LLZ fraction (it depends on the polymer molecular, Li salts and garnet topography), the system will change from polymer electrolyte to CSE; and the concentration of active Li ions rises with increasing LLZ content. The second critical LLZ fraction is reached when the fillers disrupt the conduction paths of the second phase. Based on the previous results on increasing LLZ amount to a critical point (around 6.71 vol.%/37.50 wt.%), it is the amorphous LLZ/PEO interphase rather than LLZ particles that form a percolated network (see Figure 4.8D). The highest ionic conductivity achieved at the LP37.50 can be attributed to three factors: 1) the active LLZ fillers enrich mobile Li^+; 2) the enlarged amorphous phase improves carrier solubility and mobility; 3) long-range pathways form along LLZ/PEO interphase based on percolation effect.

4.3.3 Electrochemical performance

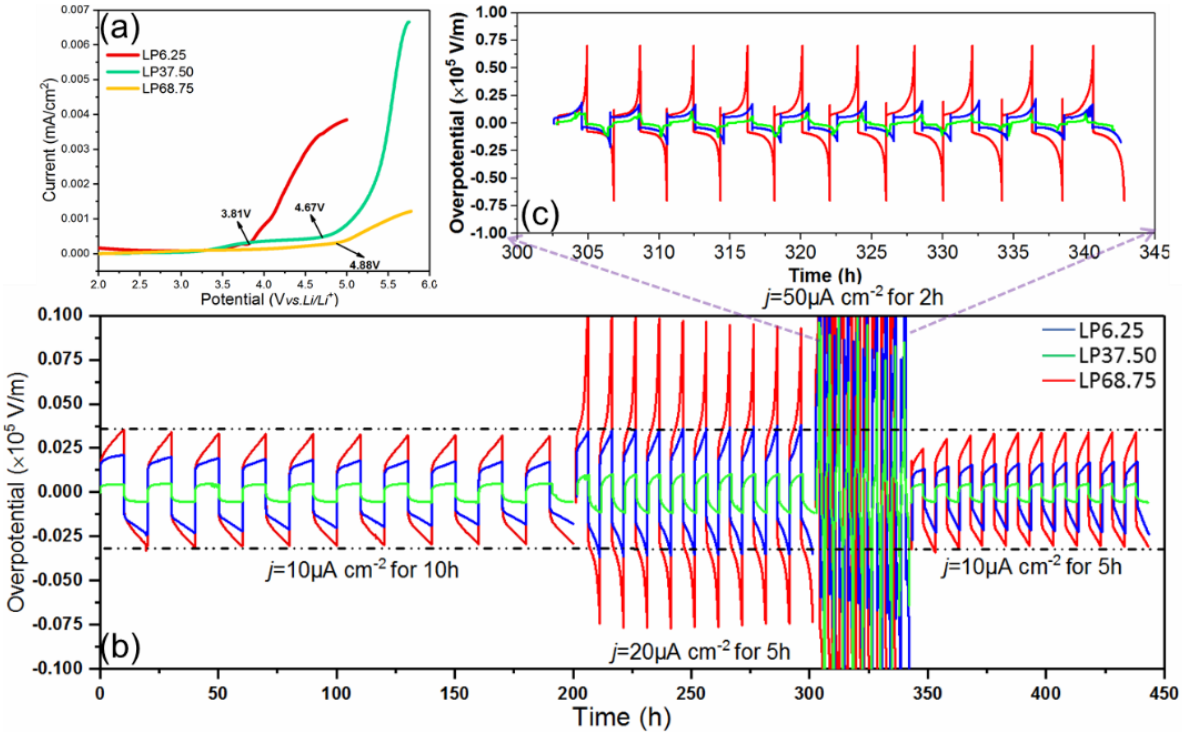

Figure 4.9. (a) Linear sweep voltammetry curves of the CSE films at 45 ℃measured in glassy-carbon|LP|Li cells; (b, c) Galvanostatic stripping/plating profiles of the CSEs in Li symmetrical cells at 45 ℃.

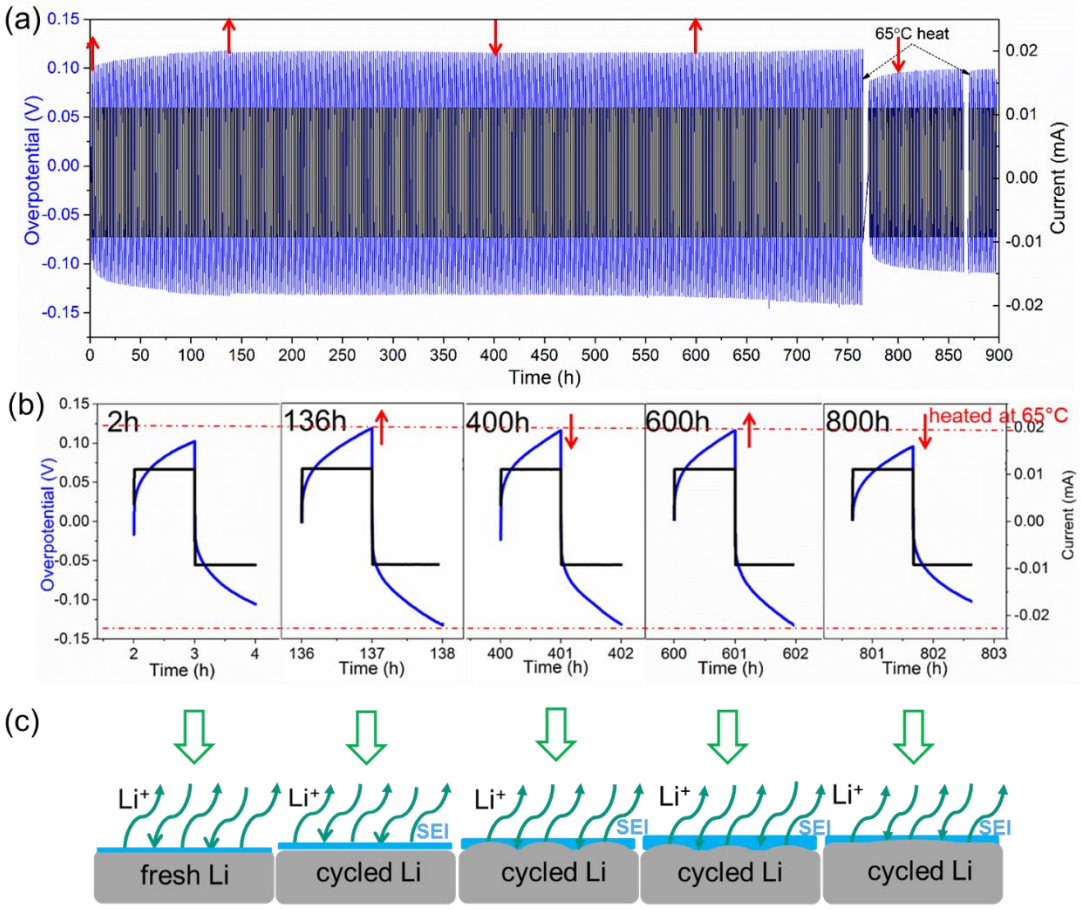

Figure 4.10. (a) Galvanostatic stripping/plating profiles using the LP37.50 at j = 10 µA cm^{-2} at 45 ℃; (b) selected overpotential profiles during this cycling; (c) schematic illustration of the passivation layer formation during Li$^+$ stripping process.

In this study, the electrochemical stability window of the CSE films was determined by linear sweep voltammetry using a Swagelok® cell (glassy carbon|LP*x*|Li). As shown in Figure 4.9a, the LP6.25 displays a severe current fluctuation from ~3.81 V, which is associated with the decomposition of the Li salt and polymer matrix [131,151]. By contrast, the current fluctuation of the LP37.50 and LP68.75 commence at ~4.67 V and ~4.88 V, respectively. Therefore, the addition of LLZ fillers can enlarge the electrochemical stability windows of the CSE film for high potential. To analyze the interface stability between Li anode and CSEs, Galvanostatic cycling was employed in Li symmetrical cells to monitor Li$^+$ stripping/plating process. As shown in Figure 4.9b and c, the LP37.50 displays the lowest potential (~100 mV) at the current density of 10 µA cm^{-2} for 10 h interval, and the same applies to the higher current densities (10, 50 and 10 µA cm^{-2}). Based on $U = IR$, the lower overpotential U indicates the lower resisitance R of the LP37.50. The smallest IR drops are also observed in the profiles of the LP37.50. Thus, effective wetting of Li foil with

the polymer matrix is beneficial to ion transfer, in contrast to the large overpotential of the LP68.75, implying its higher interface resistance [152].

To investigate cycling reversibility of the LP37.50, longtime Li^+ stripping/plating at 10 µA cm^{-2} for 2 h interval was carried out using Li symmetrical cell over 450th cycles at 45 ℃ (see Figure 4.10a). The generated potential gradually increases to 270th cycles and then decreases. As illustrated in Figure 4.10b and c, A thin SEI layer is formed at the interface (2 h), involving reactions of polymer matrix and Li foil after initial cycle, and they can provide a sufficient connection and facilitate the Li^+ transfer. Then the growing SEI layer becomes thicker with enlarging overpotential and resistance, blocking Li^+ ions in and out of the Lithium anode (136 h). Then surface of the Li foil becomes rougher due to the lithium redeposition (400 h) [153]. They can invade soft SEI layer and reduce SEI thickness and overpotential. Finally, the SEI layer becomes much thicker. But the overpotential can obviously decrease after heating treatment at 65 ℃ due to a local structural reorganization between PEO matrix and Li foil, but it works only once. Therefore, close contact between garnet fillers and polymer matrix can enable long cycling (≥ 900 h) without dendrite penetration in the lithium metal batteries. Therefore, the proper integration of LLZ fillers helps to increase the wettability, and a uniform distribution of current (charge carrier) contributes to dendrite-free lithium deposition [154,155].

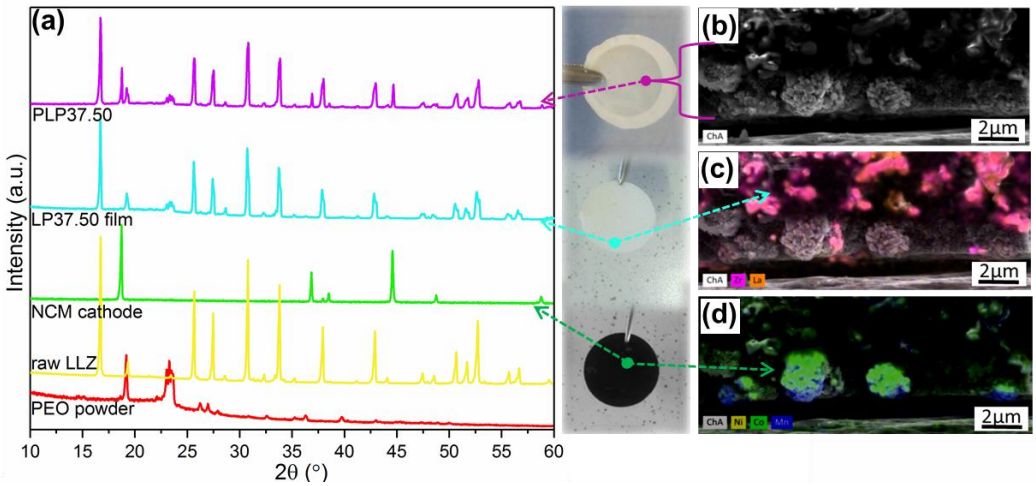

Figure 4.11. (a) XRD patterns (Cu $K_{\alpha 1}$) and digital pictures of components; (b) SEM of the interface of PLP37.50/NCM; EDX element mapping for Zr/La (c) and Ni/Co/Mn (d);

Given the ionic conductivity and cycling stability as stated above, the NCM|LP37.50|Li full cell was assembled by compressing route or coating route (see Figure S4.8a and b). Figure S4.8c and d displays cross-sectional regions of these two assembly methods, indicating a close contact in the PLP37.50 electrode (compressing route), while a huge crack exists in the CLP37.5 electrode due

to that the evaporation of sol solvent induces an intense contraction of the bulk polymer. Thus, compressing route was applied in further research. Figure 4.11a displays the XRD pattern of the LP37.50 with merged peaks attributed to either LLZ or PEO, and diffraction peaks of the PEO, LLZ and NCM are observed in the PLP37.50. Figure 4.11b-d displays SEM images of the selected EDX region of interest, which exhibits layered element distribution. Indeed, the Zr/La mapping enabled us to locate the CSE film, similar to Ni/Co/Mn mapping for the NCM cathode. The EDX mapping also confirmed that the PLP37.50 assembled by pressing route had a close contact with the CSE film.

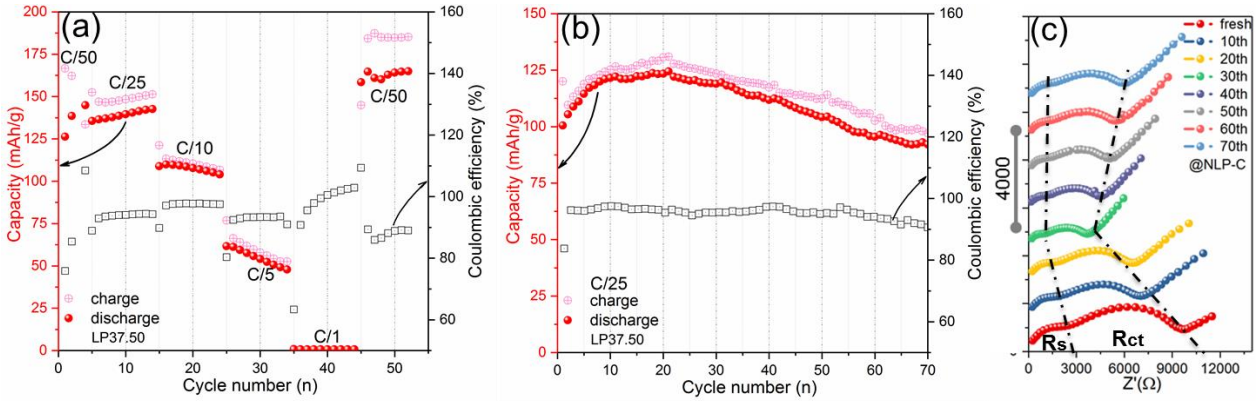

Figure 4.12. (a) Rate performance at 45 °C; (b) cycling performance of the PLP37.50, and (c) corresponding Nyquist plots recorded every 10 cycles at 45 °C.

In Figure 4.12a, compares the rate capability of samples at different current rates, the capacity values decrease with rising current rates due to the sluggish Li^+ diffusion kinetics in the CSE. The PLP37.50-based cell exhibited a moderate rate performance (140, 130, 117, 45 and 2 mAh g^{-1} at C/50, C/25, C/10 and 1C, respectively). This indicates that the CSE in this work cannot be qualified for the request of fast charge. Figure 4.12b shows the discharge capacities the PLP37.50 increase from 100 to 124 mAh g^{-1} within initial 20 cycles, which is attributed to the formation of the SEI layer and deeper activation of the cathode [156]. Then the capacities gradually decrease to 97 mAh g^{-1} after 70 cycles. The corresponding Nyquist plots display enlarging semicircles after the 30th cycle (see Figure 4.12c), where two reactions basically occur across the entire frequency range: the interface resistance (intermediate frequency semicircle) and the bulk resistance (high-frequency semicircle) [157], and the interface resistance decreases more obviously at 30th cycle, due to the close combination and formed passivation layer. Following the previous result, a long-distance Li^+ conductive pathway created by modifying distribution of the medium content of the LLZ fillers will allow fast transport of Li^+ between the anode and cathode during charge and discharge cycles.

Combining TG analysis (Figure S4.6) and stress tensile test (Figure S4.9), the CSE at low and medium content of fillers can exhibit an acceptable electrochemical performance for SSBs with superior thermal and mechanical stability.

4.4 Conclusions

In this work, the influence of variations in LLZ content on ionic conductivities and Li^+ migration routes was detailed discussed. An empirical equation about relationship between mass ratio and volume ratio of LLZ fillers was firstly proposed. Here 6.71 vol.% (37.50 wt.%) LLZ fillers were found to be enough to enlarge amorphous phase of the PEO matrix, improving carrier solubility and mobility. Different from the percolation of the garnet fillers, long-range diffusion routes were formed along the amorphous LLZ/PEO interphase, where the mobile Li^+ ions prefer to go through. The flexible and self-supporting LP37.50 exhibits high upper potential limitation reaching up to 4.7 V, moderate ionic conductivity (~1.56×10^{-4} S cm^{-1} at 45 °C), high thermal stability (decomposition temperature ≥ 355 °C) and acceptable mechanical properties. Wetting of the CSE and Li anode via thin SEI layer reduces the Li^+ transfer resistance, and a stable cycling over 900 h with Li electrodes suggests a uniform Li^+ flux across the interface; the as-prepared PLP37.50 can deliver an average capacity of ~110 mAh g^{-1} at C/25. Therefore, the integration of the advantages of the garnet and polymer electrolyte can lead to the practical application of CSEs in SSBs.

4.5 Supporting information

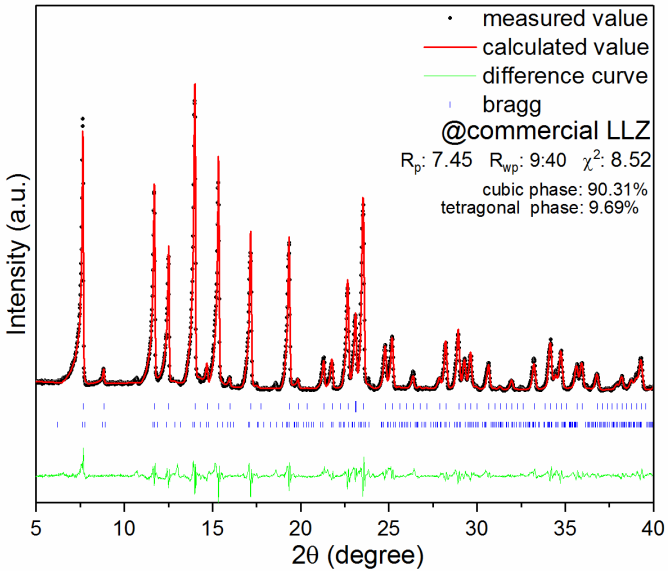

Figure S4.1. XRD (Mo K_{a1}) Rietveld refinement of the commercial LLZ.

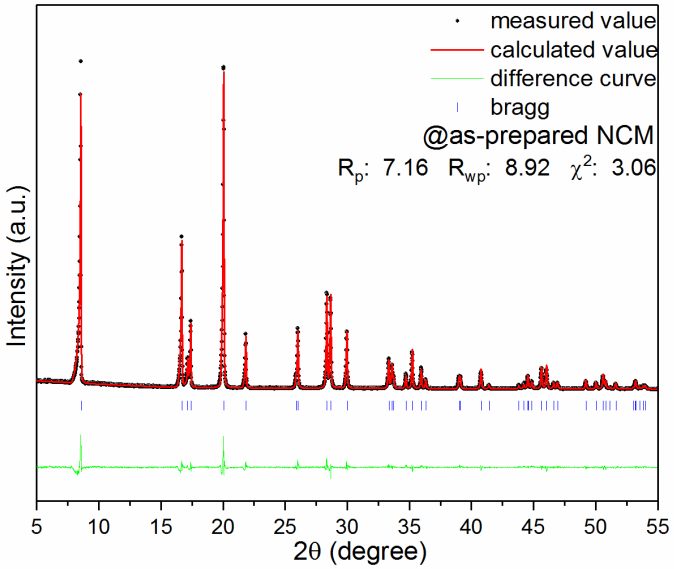

Figure S4.2. XRD (Mo K_{a1}) Rietveld refinement of the as-prepared NCM.

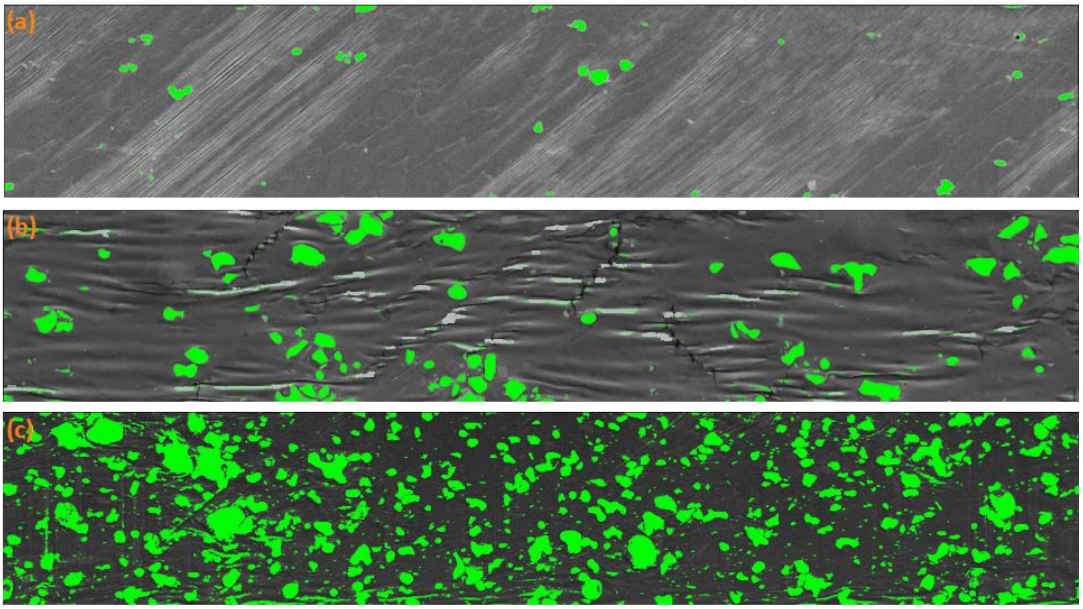

Figure S4.3. The selected cross-sectional images of the LP6.25, LP37.50, and LP68.75 used to analyze surface area ratio using ImageJ software.

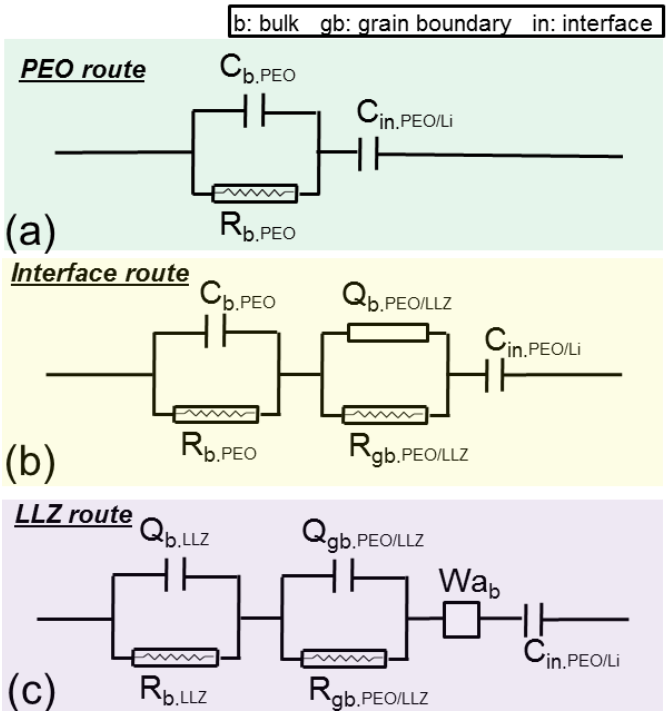

Figure S4.4. Equivalent circuit used for EIS data fitting for the CSEs with different LLZ contents: (a) low LLZ content (LP0.00~LP18.75); (b) moderate LLZ content (LP25.00~LP62.50); (c) high low LLZ content (LP68.75~LP93.75); where R_b, C_b, C_{in}, R_{gb}, Q, and Wa_b represent the bulk resistance, bulk capacitance, double layer capacitance at the interfaces, interface resistance at the LLZ/PEO or among LLZ particles, constant phase element and Warburg element (solid state diffusion of Li^+ into the cathode), respectively.

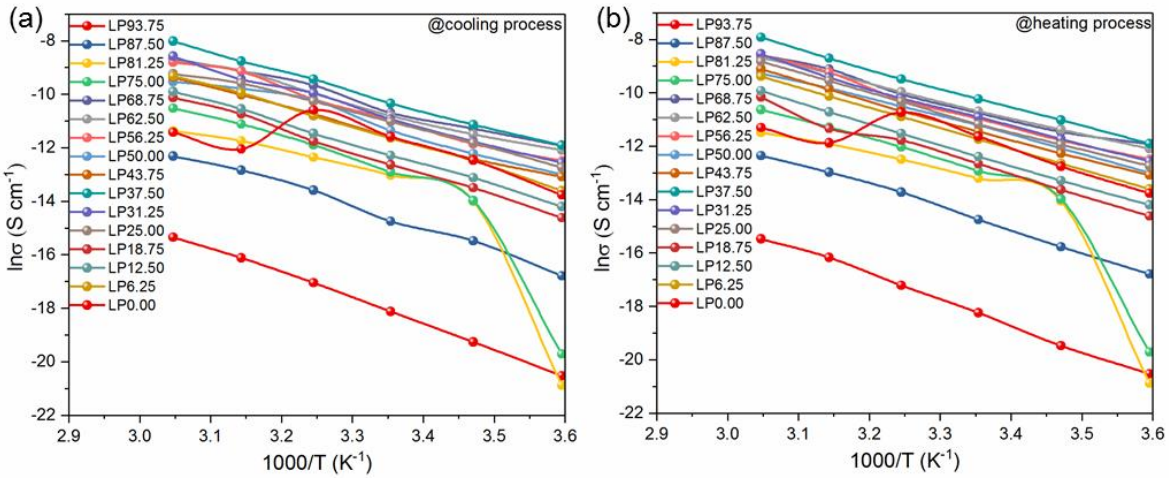

Figure S4.5. Temperature dependence of the ionic conductivities of the CSE films at varying LLZ content. Note: for the sake of readability ln(σ) vs. 1000/T is shown. The activation energies in the text are calculated from the slope of ln(σ) vs. 1/T. ,

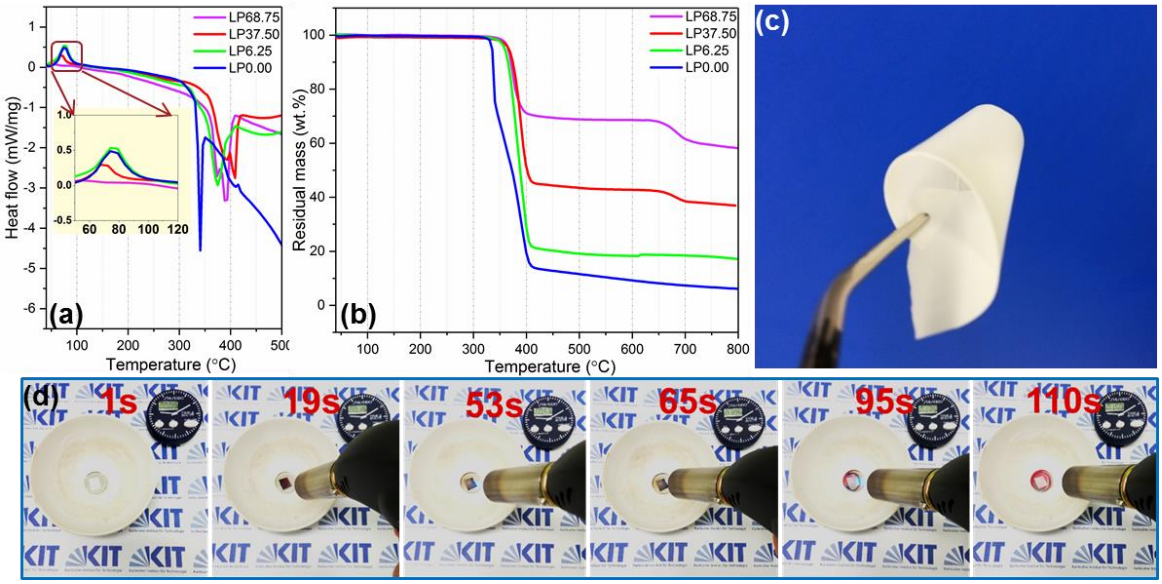

Figure S4.6. TG (a) and corresponding DSC (b) curves of the CSE films under argon flow; Digital pictures of the LP37.50 film: (c) high flexibility and (d) nonflammable property.

TG analysis: Figure S4.6a displays a severe endothermic reaction at an onset temperature of ~75 °C for the LP0.00, then T_m gradually shifts to lower onset temperatures to ~70 °C (LP37.50) and ~55 °C (LP68.75). The decrease in melting enthalpy (crystalline fraction) is also evidenced by the smaller and smaller enclosed area, because garnet fillers and Li salts can interrupt ordered structure the PEO chains, increasing amorphicity and Li^+ transferability of the CSEs [158]. Moreover, onset temperatures for the exothermic reactions gradually increase from 311 °C (LP0.00) to 345 °C (LP37.50), confirming the enhanced thermal stability induced by garnet fillers.

Enlarging upper limitation of working temperature of CSEs can significantly enhance battery safety. In Figure S4.6b, TG result confirms a major mass loss of the LP0.00 at an onset temperature of ~325 °C due

to dehydration and decomposition of the polymer, and this process is ongoing up to 420 ℃. Residual masses of the LP0.00 and LP6.25 above 500 °C are ~11.79 and 19.33 wt.%, respectively, and such serious vanishing may lead to the short-circuit at overtemperature. In contrast, the decomposition of the LP37.50 film starts at 355 ℃ after more LLZ added, indicating that garnet fillers confinement in the polymer matrix enhances thermal stability. The second mass loss occurs at 640 ~ 700 ℃ due to the lithium loss of the LLZ [159]. The LP37.50 and LP68.75 still remain ~43.58 wt.% and ~69.15 wt.% of the total mass at 800 °C, respectively. Once catching fire, the residual LLZ fillers can serve as physical barriers to insulate electrodes and avoid short circuit. The melting point (T_m) is a crucial parameter to reflect the segmental mobility and the crystalline fraction of polymers, and lowering T_m can help to realize fast charge at RT.

Figure S4.6c displays the freestanding and flexible LP37.50 film, further optimization may lead to the practical usage of the CSEs available in varied geometries of SSBs. Due to the adhesion effect between the polymer matrix and garnet fillers, the excellent elasticity can avoid the penetration of Li dendrite [103,104,133]. In Figure S4.6d, the LP37.50 was firstly oxidized into dark residual in a direct burning test, and then completely burned away without any flame combustion, while the white garnet fillers still remain there providing an ultimate protection in case of catching fires, even a steel holder turns red after 110 s of flame exposure. Thus, these achieved thermal stability and mechanical properties are beneficial to battery safety [160–162].

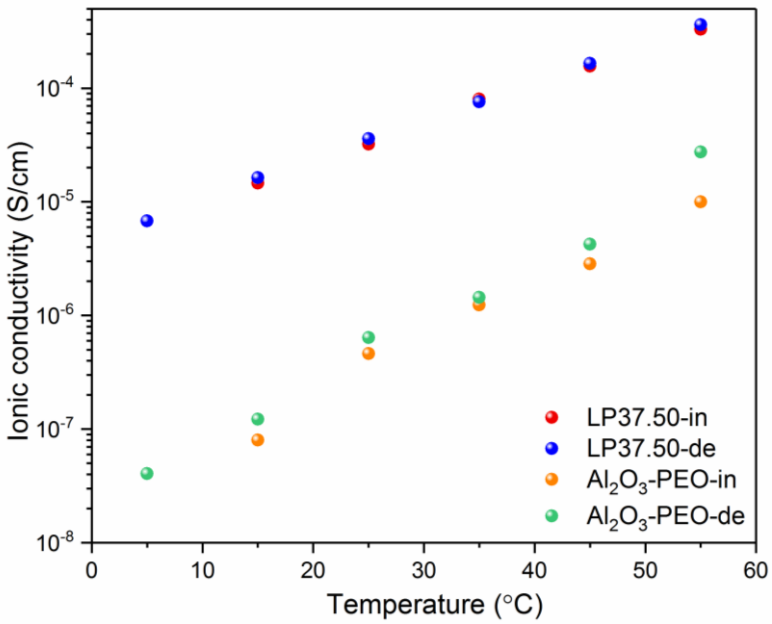

Figure S4.7. Comparison of ionic conductivity of the CSE based on LLZ and Al_2O_3 fillers at cooling(-de) and heating (-in) process.

The influence of assembly routes

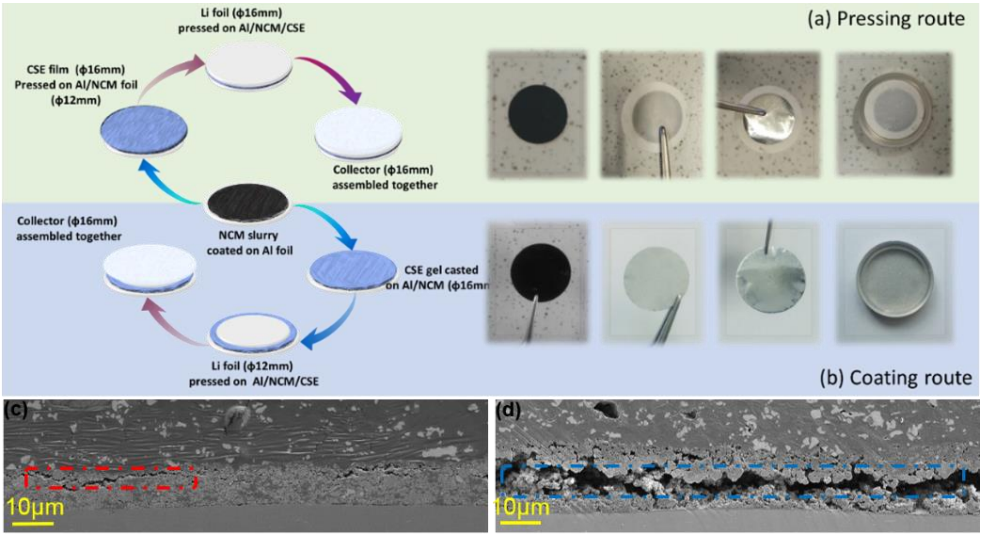

Figure S4.8. Schematic assembly of the full SSBs: (a) PLP37.5: CSE films pressed on NCM cathode on Al foil; (b) CLP: polymer gel coated on NCM cathode on Al foil. The insert graphs display the actual interface in different assembly steps; SEM cross-sectional images: (c) a close contact between PLP37.5 electrode and Al foil irrespective of a slight slit (red square) due to the compressed recovery during the pressing process, (d) a huge crack band (blue square) exists in the CLP37.5 electrode due to that the evaporation of sol solvent induces an intense contraction of the bulk polymer.

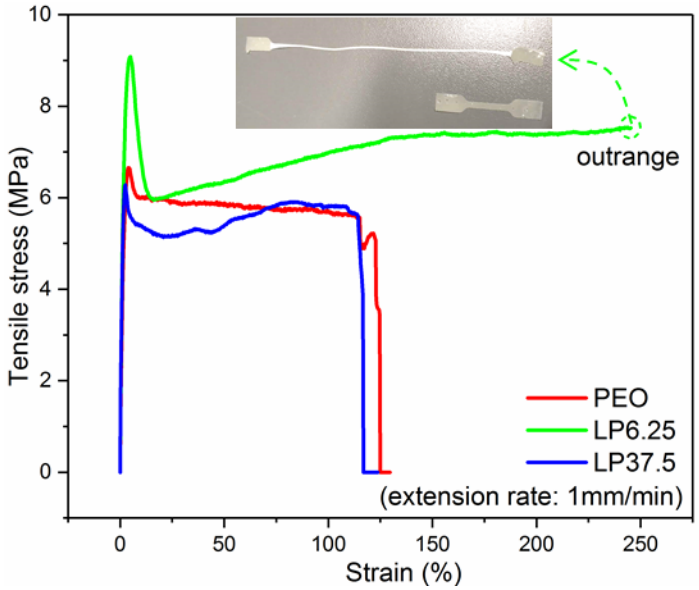

Figure S4.9. The stress-strain curves of PEO, LP6.25 and LP37.50 CSE films, which was investigated by a dynamic mechanic tester (GABO Qualimeter, Eplexor 150N). Initially, the elongation at break increases with the added LLZ fillers (6.25 wt.%), possessing the highest tensile strength of 9.1 MPa. However, the tensile strength (6.4 MPa) and elongation at break (~114%) of the LP37.50 are obviously decreased as high as the pure PEO film, and the LP68.75 cannot be a self-supporting film.

Chapter 5 Crosslinked polyglycol-garnet composite solid electrolyte

5.1 Introduction

In the previous chapter, we discussed the influence of variations in LLZ content on ionic conductivities and Li^+ migration routes. However, it has been shown that linear polyethylene oxide (PEO) exhibits low ionic conductivity at RT. Notably, the pure PEO is a semi-crystalline material below 60 ℃ due to its regular units in long-range. Segmental mobility is limited by these crystal domains, resulting in low conductivities (10^{-8} ~10^{-6} S cm^{-1} at RT) and low ionic transfer number (~0.3) [129]. At high temperature (≥ 50 ℃), the melt PEO matrix will lose its dimensional stability, impeding migration of Li^+ ions through favorably placed paths and leading to short-circuits. One way to solve the issues is to use a crosslinked polymers to improve structural disorder and stability [163–166].

As a shared concern, SEs cannot fully infiltrate the electrode interior like LEs, resulting in low ionic conductivity and serious cycling fade. Tailoring interfacial contact is the major target in the research of solid state batteries (SSBs) [70,122,127,128]. In contrast, organic polymer electrolytes are soft enough to contact electrode materials. When considering Li^+ solvation, strong coordination induced by oxygen atom is found in ether, carbonates, esters and ketones groups, and recent studies confirmed that Li^+ prefers to coordinate with glycol ethers, especially ones of suitable lengths showing high ionic conductivity [91,92]. Polymer electrolytes also possess low mechanical strength, and their thermal stability and flammability are also controlled by the organic nature. However, mobile Li^+ ions prefer to travel through the amorphous segmental chain in the CSEs. The dilemma is that a more flexible polymer can transport ions better, but fails in terms of rigidity. Therefore, inorganic fillers like active Li^+ garnet fillers were therefore incorporated into polymer matrix [95–98]. For the sake of conductivity and safety as discussed above, the segmental flexibility and bulk stability of polymer matrix should be simultaneously considered. In order to combine of advantages of the garnet filler and crosslinked glycol for efficient Li^+ dissolvability at the microscale and enough mechanical strength at the macroscale. In this work, a crosslinked polyglycol is prepared on the basis of polymerization of terminal active groups with incorporated garnet fillers,

maintaining the bulk structural stability and interconnected ionic pathways at high temperature. A high ionic conductivity as well as superior electrochemical performance are expected due to this unique structures and close contact between the electrolyte and electrode.

5.2 Experimental

5.2.1 Preparation of composite solid electrolyte film

Commercial Bisphenol A diglycidyl ether (BADGE, 50 mg, liquid chromatography purity ≥ 95%, M_w = 340.41 g, Sigma-Aldrich), polyethylene oxide (PEO, 30 mg, $M_w \approx 5\times10^6$, Sigma-Aldrich), $Li_7La_3Zr_2O_{12}$ (LLZ, 25 mg, NEI Corporation), and lithium bis (trifluoromethylsulfonyl) imide (LiTFSI, (EO)/Li^+ = 8 in molar, ion chromatography purity ≥ 98.0 %, Alfa-Aesar) were stepwise added into *O,O'*-Bis (2-aminopropyl)polypropylene glycol-block-polyethylene glycol-block-polypropylene glycol (Jeffamine® ED600, 245 mg, $M_r \approx 600$, Aldrich) with stirring at 1200 rpm. After degassing the polymer sol, it was solidified into quasi-solid-state gel via the polymerization of terminal active groups at 90 ℃ curing for 12 h, as depicted in Figure 5.1a. The casting ether-abundant film was freestanding and high-tensile, abbreviated as BPL. As references, the films consisting of PEO + LiTFSI and PEO + LiTFSI + LLZ dissolved in Dimethylcarbonate (DMC, gel chromatography purity ≥ 99.0%, Merck KGaA) were also prepared via the gel-casting process, abbreviated as PLi and PL, respectively (see detail components in Table 5.S1). The BPL without LLZ fillers is too sticky to be free-standing film, thus will not discussed here.

5.2.2 General characterization

X-ray diffraction (XRD) was carried out using an STOE STADI P X-ray powder diffractometer equipped with a Mythen1K detector and a Co K_α radiation (λ=1.78896 Å) to characterize the crystalline structure of the CSEs. The surface morphology of films was investigated with a Merlin scanning electron microscopy (SEM, Zeiss GmbH). Thermogravimetry (TG) data was collected through an STA 449C Netzsch analyzer from 35 ℃ to 800 ℃ at a heating rate of 5 ℃ min^{-1} under argon flow (42 mL min^{-1}). A Bruker Tensor 27 Fourier transform infrared spectroscopy (FT-IR) spectrometer was used to collect data from 4000 ~ 400 cm^{-1} in ATR transmittance mode to examine the polymerization reaction.

Pulsed-field gradient-nuclear magnetic resonance (PFG-NMR) spectra were measured on a Bruker Avance 300 MHz spectrometer equipped with a Diff 50 probe, which produces pulsed-field gradients reaching up to 3000 G cm^{-1}. The ^{7}Li NMR spectra were measured at 116.6 MHz. A stimulated-echo pulse sequence in combination with bipolar gradients was used to observe the echo damping as a function of gradient strength. The duration of the $\pi/2$ and π pulses varied from 27 ℃ to 70 ℃. Recycle delays in the range of 1 to 2.5 s were chosen on the basis of the T1 measurement results. All delay times during each PFG-NMR experiment were kept constant, whereas the gradient amplitude was varied to cause the signal decay, then the influence of relaxation on the echo decay is eliminated. The optimal values for the gradient duration δ and the diffusion time (Δt) were found to be around 3 and 160 ms, respectively. In total 16 points were acquired to form each diffusion decay, and each point was sampled with 64 scans.

5.2.3 Electrochemical evaluation

Electrochemical impedance spectroscopy (EIS) tests were carried out over a frequency range of 10^{6}~10^{-2} Hz with a sinus amplitude of 10 mV during cooling and heating (85 °C→5 °C→85 °C). The CSE film (ϕ12 mm) was sandwiched by stainless steel cylinders (SS) and assembled into a Swagelok® cell. Prior to measuring, the cells were kept in the climate chamber (M53, Binder GmbH) at the setting temperature for 30 min. The obtained impedance spectra were fitted using ZsimpWin software (Ametek. Inc.). The total conductivity σ_t was calculated based on the equation $\sigma_t = l/A \cdot R$, where l, A and R represent the thickness (cm, which is the average of five measurements by Sylvac thicknessmeter), electrode area (cm^2) and total resistance (Ω) of the CSE film, respectively. Tests for Electrochemical stability window were performed in a coin cell (SS|CSE|Li) through linear sweep voltammetry over a potential range of 2.0~9.0 V (*vs.* Li/Li^+) at a scanning rate of 1 mV s^{-1} at 45 °C. Cyclic voltammetry (CV) was applied for a symmetrical cell (Li|CSE|Li) at a potential range of -1.0~1.0 (*vs.* Li/Li^+) at a scanning rate of 1 mV s^{-1} to determine Li^+ solubility. Galvanostatic cycling using Li symmetrical cells was also performed at a current density of 10 μA cm^{-2} for 2 h.

5.2.4 Battery tests

$LiNi_{1/3}Co_{1/3}Mn_{1/3}O_2$ (NCM) was prepared with a hydroxide co-precipitation method described by Hua *et al.* [132]. A typical cathode slurry was fabricated by mixing NCM powder,

hybrid binder (2.5 wt.% solvend (PEO:SBR = 51.6wt.%:48.4wt.%) in aqueous solution), carbon black (Super-C65, Timcal Ltd.) and LLZ at a weight ratio of 8: 1: 0.9: 0.1. The uniform slurry was coated on Al foil using a laboratory coater with doctor-blade and then dried at 80 ℃ for 12 h. CR2032 cells were assembled in an argon-filled glovebox (MB200, Mbraun GmbH) consisting of the NCM cathode foil (ϕ12 mm), CSE film (ϕ16 mm) and Li foil (ϕ12 mm, Alfa Aesar), then compressed under 15 MPa and aged at 80 ℃ to ensure the components were closely packed. Electrochemical tests were performed utilizing a multichannel potentiostat (VMP3, Bio-Logic). A voltage range of galvanostatic charge/discharge was set to be 2.5~4.3 V (*vs.* Li/Li^+).

5.3 Results and discussion

5.3.1 Crosslinking preparation

Figure 5.1a depicts conceptual illustration for synthesizing a crosslinked polymer matrix, where the terminal active groups (epoxy–amine) from ED600 and BADGE can react with each other to build an ether-abundant gel at a mild temperature (90 °C) (see Figure 5.1b). In this study, the BPL film is composed of LiTFSI embedded in the ED600-BADGE crosslinked matrix. The larger anions ($TFSI^-$) can easily dissociate in the PEO matrix and set off the free Li^+ ions; owing to the presence of a strong electron withdrawing group (SO_2CF_3), high flexibility and excellent chemical stability [147]. To achieve enough mechanical strength, 25mg LLZ fillers (see Figure 5.1c) and macromolecular PEO is added into the BPL. The incorporated LLZ is a typical garnet SE, which has high thermal stability, electrochemical stability, and high ionic conductivity. SEM image of the LLZ fillers displays irregularities in shape and a narrow size distribution (average size = 743 ± 194 nm). Based on Rietveld refinement, the LLZ fillers consist mainly of the cubic phase (space group: 90.3% $Ia\bar{3}d$, see Figure S5.1). Figure 5.1d shows a rough surface of the PEO matrix with embedded LLZ fillers, and the obvious segregation of fillers from the matrix. In comparison (Figure 5.1e), the fillers are homogeneously dispersed throughout the BPL film. No voids are detected between the ceramic phase and the polymer phase. Indeed, the smooth interface and uniform structure can induce homogeneous current flow and avoid the polarization [163].

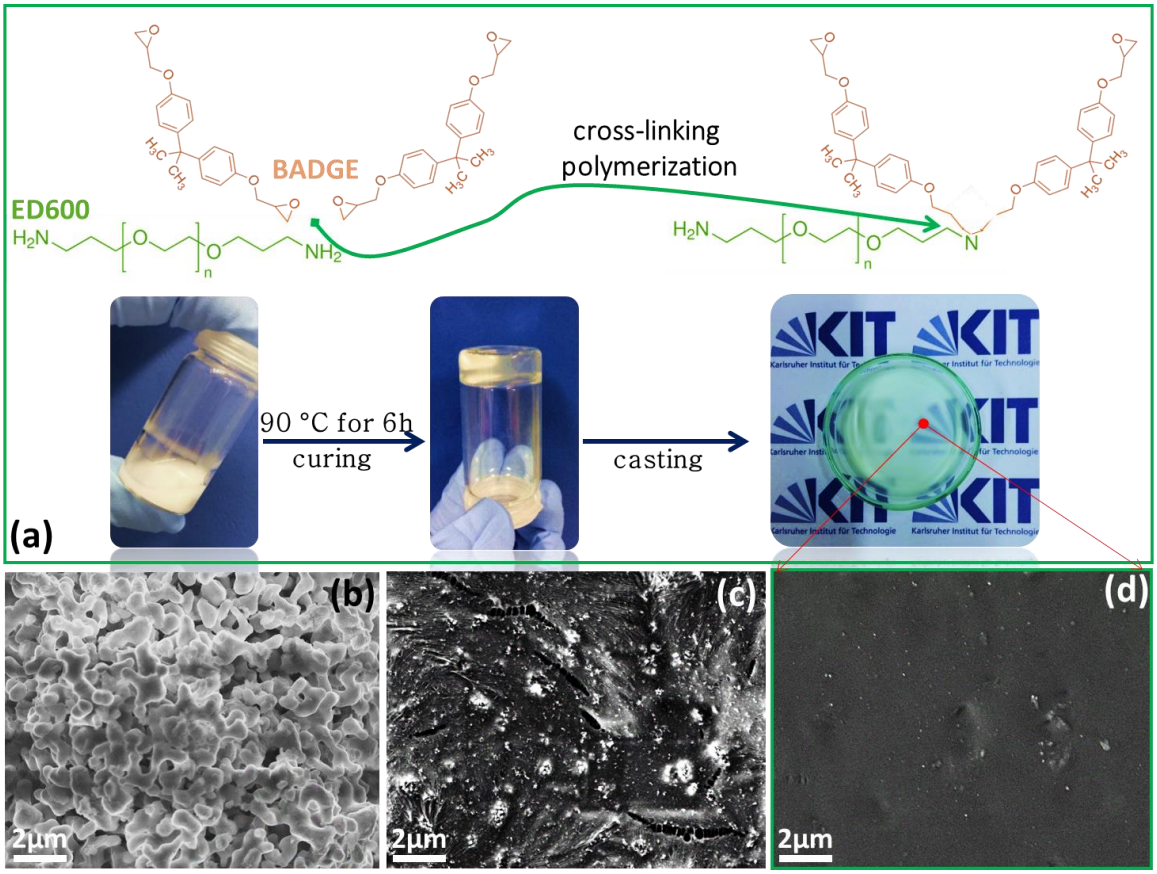

Figure 5.1 (a) Conceptual illustration of the cross-linking polymerization of O,O-Bis(2-aminopropyl)polypropylene glycol-block-polyethylene glycol-block-polypropylene glycol (ED600) and bisphenol-A diglycidyl ether (BADGE), and photographs of the precursor sol, crosslinked gel and casting film; SEM images: $Li_7La_3Zr_2O_{12}$ (LLZ) fillers (c) the PL film (d) and the BPL film (e).

In Figure 5.2a, FTIR spectra are shown to examine the crosslinked between terminal amine groups from ED600 and terminal epoxy groups from BADGE after 90 °C curing. In these CSEs, the peaks located at 1095 and 1461 cm^{-1} correspond to the –C–O–C– stretching and $–CH_2$ bending from the $–(CH_2CH_2O)_n–$ backbone. The peaks at 738 and 790 cm^{-1} in the PL are ascribed to the symmetric bending and stretching modes of $–CF_3$ and C–S groups of the $(TFSI)^-$ anion, respectively [164]. The absent stretching vibration- and bending mode of HO– at ~2875 cm^{-1} in the LLZ verifies no proton-ion exchange (substitution of Li by H) proceeded during storage [167]. The peak at 1510 cm^{-1} is ascribed to the –C=C– stretching of the benzene rings from bisphenol-A. It is notable that the 1582 cm^{-1} peak corresponding to –C–N– symmetric stretching appears in the BPL film, which confirms the crosslinked groups in the BPL. The N atoms from terminal amine groups with strong electronegativity can attract Li^+ ions to migrate into the amorphous region, which may improve ionic conductivity. In Figure 5.2b, the peak intensities at 21.1°~28.4° for the PL and BPL obviously decrease compared to the PEO and the

PLi films, indicating a dramatic drop in crystalline phase. The incorporation of LiTFSI can activate the CSEs and improve its ionic conductivity [168], but no corresponding peak is observed in the PLi pattern, confirming the complete dissolution of Li salt in the polymer matrix [169]. ED600 mainly consists of polyphenylene oxide (PPO) segments that interrupt the ordered segmental array, and garnet fillers also reduce the crystallinity of the BPL film as discussed in Chapter 4. Thus, Li^+ ions can easily creep along the polymer chains in the amorphous region based on Li^+ dissolution and coordination process [147].

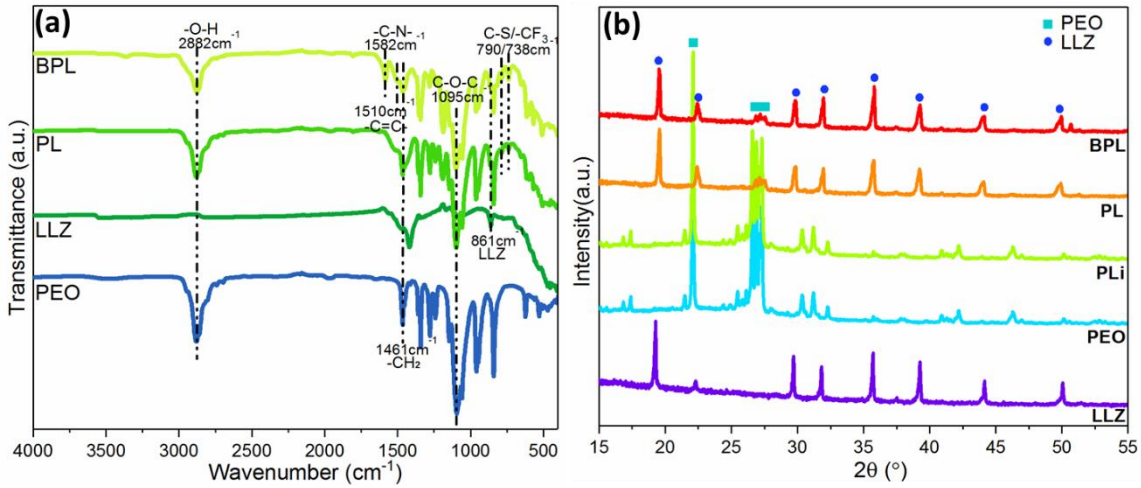

Figure 5.2. FTIR spectra (a) and XRD patterns (b) of the raw components and the CSE films.

In Figure 5.3, the TG curves show that the PLi, the PL and the BPL films exhibit the major decomposition at ~350 ℃ due to dehydration and decomposition of the polymer matrix, and the residual mass remains stable after 400 ℃. In particular, garnet fillers increase the onset decomposition temperature up to 348 ℃ for the PL film, compared to that of the PLi at 329 ℃. In contrast, the BPL displays the lowest onset temperature of 298 ℃, and it is consistent with our expectation. The inserted DSC curves display the smallest enclosed endothermic area of the BPL at melting point, confirming the lowest crystallinity in the BPL, which agrees with the XRD result. This implies that the crosslinked matrix and garnet fillers disturb the ordered structure of the glycol chains [158]. The main target of this study was to increase the segmental flexibility and ionic mobility. To achieve this, it is inevitable to decrease the rigid structure. Although the decomposition temperature decreased to about ~300 ℃, which is still enough for normal battery application. Figure 5.3b shows a direct burning test of the BPL without any combustion; the polymer matrix was oxidized into dark residual and then completely burned

away after 113 s of flame exposure, while garnet fillers still remained there providing the ultimate protection in case of short circuit. These results confirm the nonflammable nature and high thermal stability of the BPL.

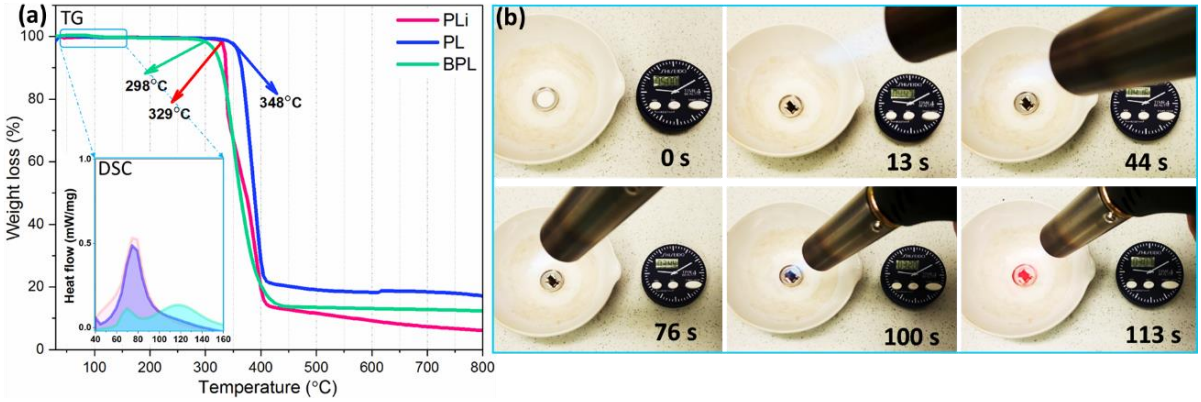

Figure 5.3 (a) TG and inserted DSC curves of the CSE films under argon flow (42 mL min^{-1}) at a heating rate of 5 ℃ min^{-1}; (b) a direct burning test on the BPL film over 113 s.

5.3.2 Ionic conductivity

Ion conductivity is the fundamental property of electrolyte materials, and EIS is a powerful technique to analyze the kinetic behavior of ion motion by modeling equivalent circuit. Selected Nyquist plots of the PL and BPL achieved at heating process are shown in Figure 5.4a&b. All CSE films sandwiched by stainless steel electrodes (Figure 5.4c) show semicircles in the high-frequency region below 45 ℃, which corresponds to electrolyte bulk resistance (R_b) and electrode/electrolyte interface resistance (R_{in}), respectively [158]. There are only oblique lines above 45 ℃ in the Nyquist plots due to Warburg diffusion (W_a) in the CSEs (see Figure 5.4d). Based on previous reports [106,133,135], an equivalent circuit R_e-(R_b/CPE)-(C_{in}/R_{in})-W_a (see Figure 5.4f) was proposed for data fitting, where R_e, R_b, CPE, C_{in}, R_{in}, and W_a represent the contact resistance, bulk resistance, constant phase element, double layer capacitance at the interfaces, interface resistance and Warburg element, respectively. An overview of total ionic conductivities as a function of testing temperature is depicted in Figure 5.4e and Table S5.2. The ionic conductivities of the CSEs increases as the temperature goes up, because the transient mobility of the polymer chains can be enhanced by enlarging free volume, and therefore ion transfer is thermally activated by higher temperature. In detail, the BPL exhibits higher ionic conductivity than the PL below 55 ℃. This confirms that crosslinked polymer chains and garnet fillers dispersed in the glycol matrix lead to low amount of crystalline phase and high

conductivity. On the other hand, Y. Hu's group confirmed that decomposed LLZ can provide extra mobile Li^+ ions, finally forming a long-range pathway for Li^+ transfer [135,141]. At the same testing temperature, the CSE films display higher conductivities at cooling process than that at heating process. This is due to the thermal history and slow recrystallization kinetics of polymer materials below melting point [80,133,144]. At higher temperature (≥65 ℃) the PL film will more easily melt and lose its dimensional stability, disturbing Li^+ migration through favorable localized pathways, as reported by Porcarelli *et al.* [163]. Compared to that of the PL, the BPL film possesses higher ionic conductivity over the whole temperature.

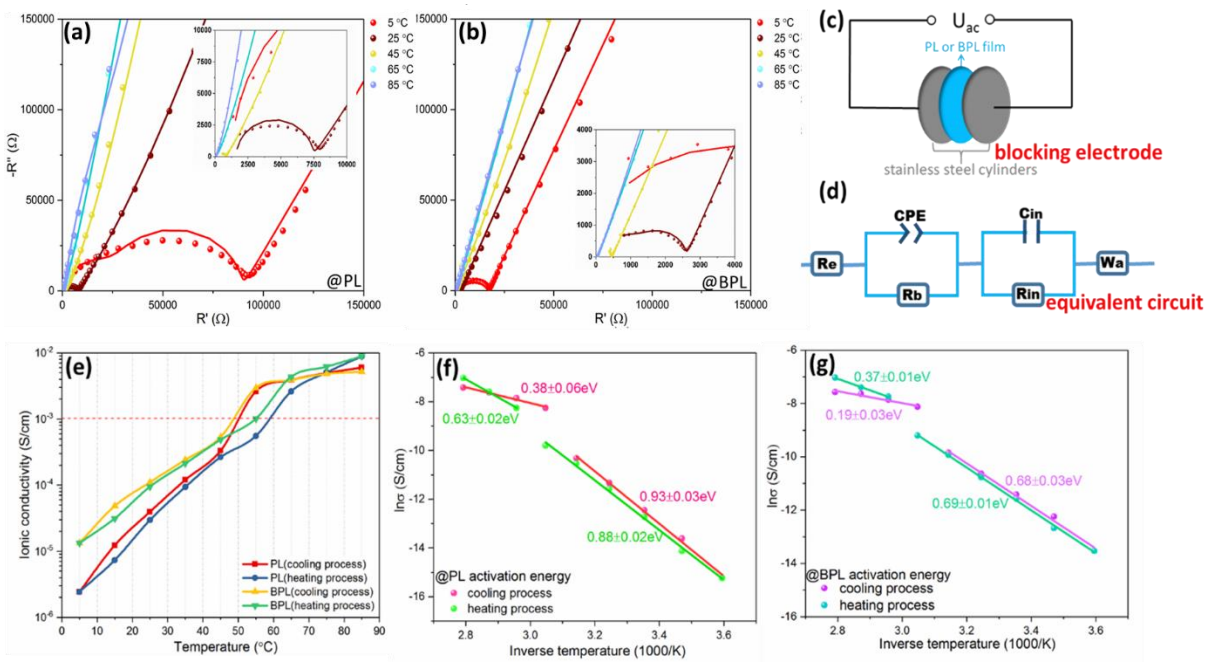

Figure 5.4. Nyquist plots of the PL (a) and BPL (b) at heating processes; illustration of the measured blocking electrode (c) and its equivalent circuit (d); conductivities of the PL and BPL films at the cooling- and heating processes (e). Arrhenius fitting curve of the PL (f) and BPL (g) films. Note: for the sake of readability $ln\sigma$ vs. 1000/T is shown here, the activation energies in this study are calculated from the slope of $ln\sigma$ vs. 1/T.

Figure 5.4f&g depicts ionic conductivities ($ln\sigma$) of the CSE films as a function of temperature (1000/T), and the temperature dependence of the conductivities is well-described by the Arrhenius law, and there are two types of activation energies above and below the melting temperature. It is noteworthy that activation energy for charge transfer depends on local relaxation and segmental motion of the polymer chains. In general, below 55 ℃ Li^+ ions can only hop in the solid solvent of the CSE decoupled with segmental movement [130]. In contrast,the activation energies are obviously reduced above 55 ℃ because of low resistivity

of the melten polymer, and Li^+ ions can go fast through the CSE coupled with chain motion. At cooling process, the calculated E_a of the PL below 55 ℃ (0.88±0.02 eV) is larger than that (0.69±0.01 eV) of the BPL, and this applies the same to E_a at heating process. The lower the activation energy is, the easier the Li^+ ions overcome the barrier. As discussed above, the results can be attributed to three factors: 1) the flexible polymer backbone improves amorphous phase and Li^+ mobility; 2) the crosslinked matrix can stabilize favorable localized pathways; 3) long-range diffusion pathways can form along the crosslinked chains.

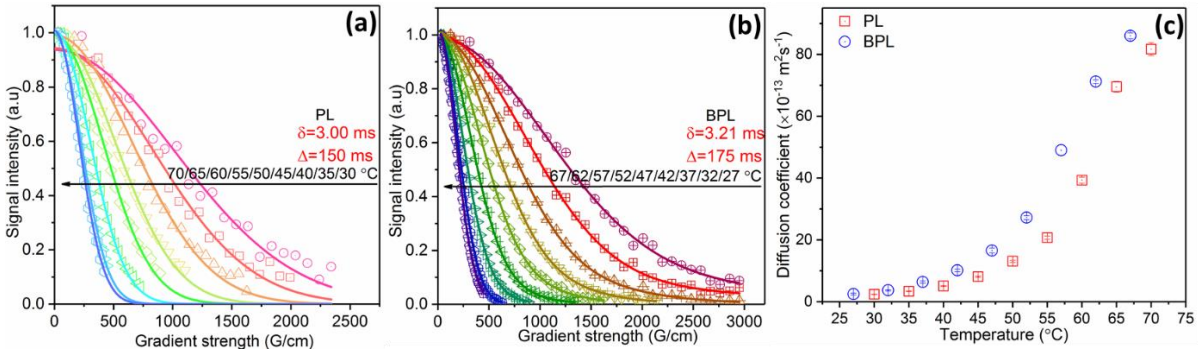

Figure 5.5. PFG-NMR results: echo damping vs. gradient strengths of the PL (a) and BPL (b); the calculated diffusion coefficient D_{Li} (c).

To study long-range dynamic diffusion and ionic mobility, PFG-NMR test was performed on time scale of 150 or 175 ms, to record diffusion-caused damping of the signal intensity as a function of temperature in the range of 27~70 ℃ with a step of 5 ℃. In Figure 5.5a and b, 1024 scans were applied to record 16 gradients per temperature for each diffusion decay, and a standard Stejskal-Tanner equation was utilized to process diffusion curve obeyed single Gaussian behavior at each temperature and determine diffusion coefficient (D_{Li}). An echo damping is clearly observed when increasing gradient strength. The echo dampings fall to overlap above 60 ℃, suggesting fast Li^+ diffusion can achieved at melten status in the CSEs. Figure 5.5c and Table S5.2 displays temperature-dependent D_{Li} of the PL and BPL films calculated from the *dc* conductivity using the Nernst-Einstein relation [41]. The BPL film exhibits higher D_{Li} over the whole temperature range, ascribed to the large amorphous content and high free volume in the crosslinked matrix, resulting in easier Li^+ migration in the CSE [130]. The diffusion coefficient results agree well with the trend of ionic conductivities (see Figure 5.4).

5.3.3 Electrochemical performance

To determine the electrochemical stability window, a Swagelok® cell consisting of CSE film sandwiched between SS cylinder (working electrode) and Li foil (counter/reference electrode) was assembled for linear sweep voltammetry test at 45 ℃. As displayed in Figure 5.6a, the PLi displays an obvious current fluctuation from ~3.81 V due to the decomposition of the PEO and LiTFSI [131,151]. In contrast, the current fluctuations of the PL commence at ~4.97 V. The results confirm that LLZ fillers can stabilize the polymer matrix and Li salt at high voltage [160]. However, the terminal functional groups of the BPL may involve electrochemical reaction, leading to reduced electrochemical stability window to ~4.51 V.

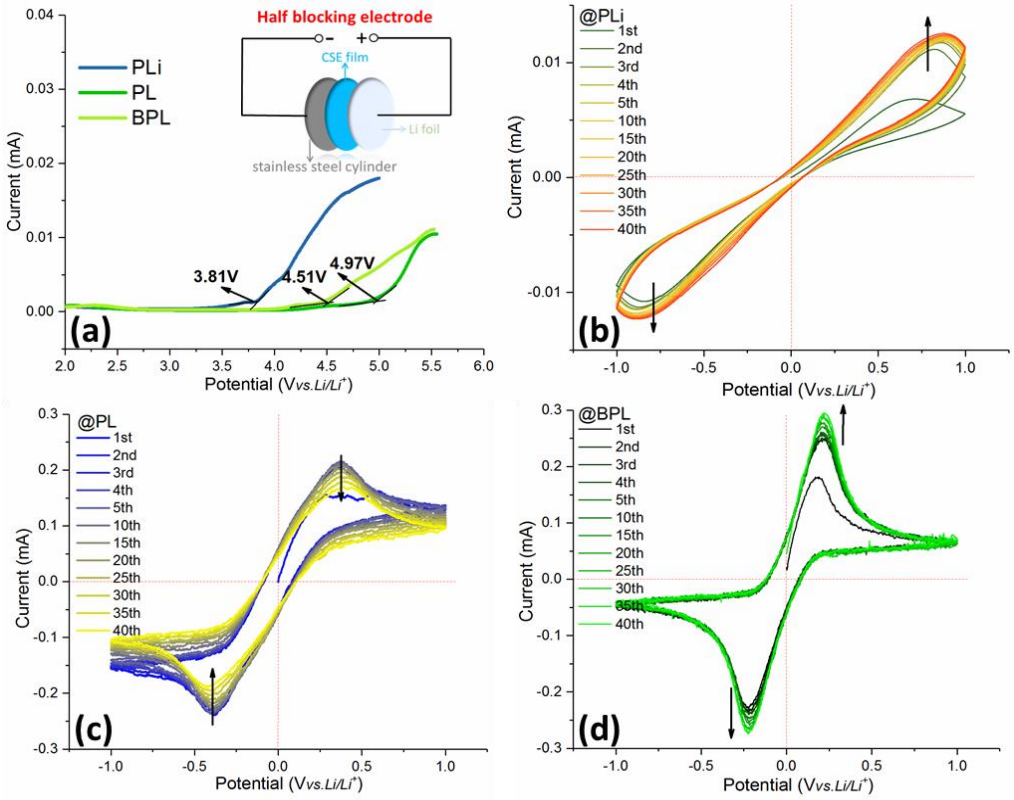

Figure 5.6. (a) Linear sweep voltammetry curves of the CSE films at 45 ℃ measured in SS|CSE|Li cell; CV curves: the PLi (b), the PL (c) and the BPL (d) in Li symmetrical cells over -1.0 V~1.0 V.

In general, Li^+ ions prefer to coordinate to four or six ether-oxygens as Lewis base, and Li^+ transport occurs when initial coordination breaks and the new one forms. Similar to PEO structure, the flexible backbone of the ED600 is rich in ether oxygen (poly(phenylene oxide)) and can easily complex Li^+ ions [166,170]. To determine Li^+ stripping from Li metal and dissolving in CSEs, CV tests were performed using Li symmetrical cells at the potential range of -1.0~1.0 V *vs.* Li/Li^+ at 45 ℃. An ideal SE can be considered ionic cable, and the current *vs.* potential profile should be an oblique line in the CV curve. In fact, it is difficult for the CSE to

behave like a pure ionic resistor because of the hysteresis of current response during the CV test, even for LP30 electrolyte (see Figure S5.2). In Figure 5.6b, the symmetrical CV curves of the PLi actually display capacitor behavior, and no current peak is observed because Li^+ ions are mainly stored at the CSE/Li interface by forming electric double layer [155]. In Figure 5.6c and d, cathodic peaks of the PL and BLP films are ~0.38 V and ~0.22 V, respectively, which indicates the amorphous polymer matrix can enhance Li^+ solubility. Based on the same scan rate $v = u/t = i/C$, the increase in current (i) accounts for high capacity (C) and more Li^+ dissolution in the CSEs. It is notable that the PL displays serious current fluctuations because of the inhomogeneous distribution of fillers and insufficient connection with Li anode. Therefore, the PL film suffers the polarization problem arising from uneven plating/stripping, which often leads to hazardous dendrite formation [163]. In contrast, CV curves of the BPL exhibit highly uniform and overlapping current.

To dynamically investigate interfacial stability and cycling reversibility of the CSE films, longtime galvanostatic Li^+ stripping/plating at current density j = 10 µA cm^{-2} was carried out using Li symmetrical cell for 2 h interval at 45 ℃. It can be seen that the overpotential is ~0.034 V and ~0.025 V for the PL and BPL within the initial 50 cycles, respectively. In detail, severe turbulent potentials are occasionally observed in the PL (see Figure 5.7a), which is due to the polarization current, and the interfacial impedance slightly increases with following cycles (see Figure 5.7c). In contrast, the BPL film displays the overall stable currents during the cycling test over 500^{th} cycles (≥ 1000 h). Hence, the soft and interlinking polymer matrix can contact Li foil well according to local topography, whereas the rigid PL film cannot achieve close interfacial contact with the electrodes [120].

Figure 5.7b confirms the stable interfacial impedance of the PL as cycling goes on. However, Figure 5.7d shows high resistance induced by the insufficient contact, then the formed SEI layer can facilitate Li^+ transfer through the BPL film, slightly reducing the resistance at 32^{nd} cycle (see Figure 5.7e), whereas the growing SEI layer can block Li^+ ions in and out of the CSEs after 50^{th} cycle. Within 500^{th} cycles (≥ 1000 h), there is no destabilization of overpotential in the BPL film, indicating dendrite-free lithium deposition during long cycling [154,155]. Therefore, the amorphous matrix helps to dissolve Li^+ ions for homogeneous current flow, and local flexibility of the BPL film can facilitate the wetting of the CSE by the Li foil

and inhibit the growth of lithium dendrite, but chemical stability of the BPL with Li electrode should be further improved.

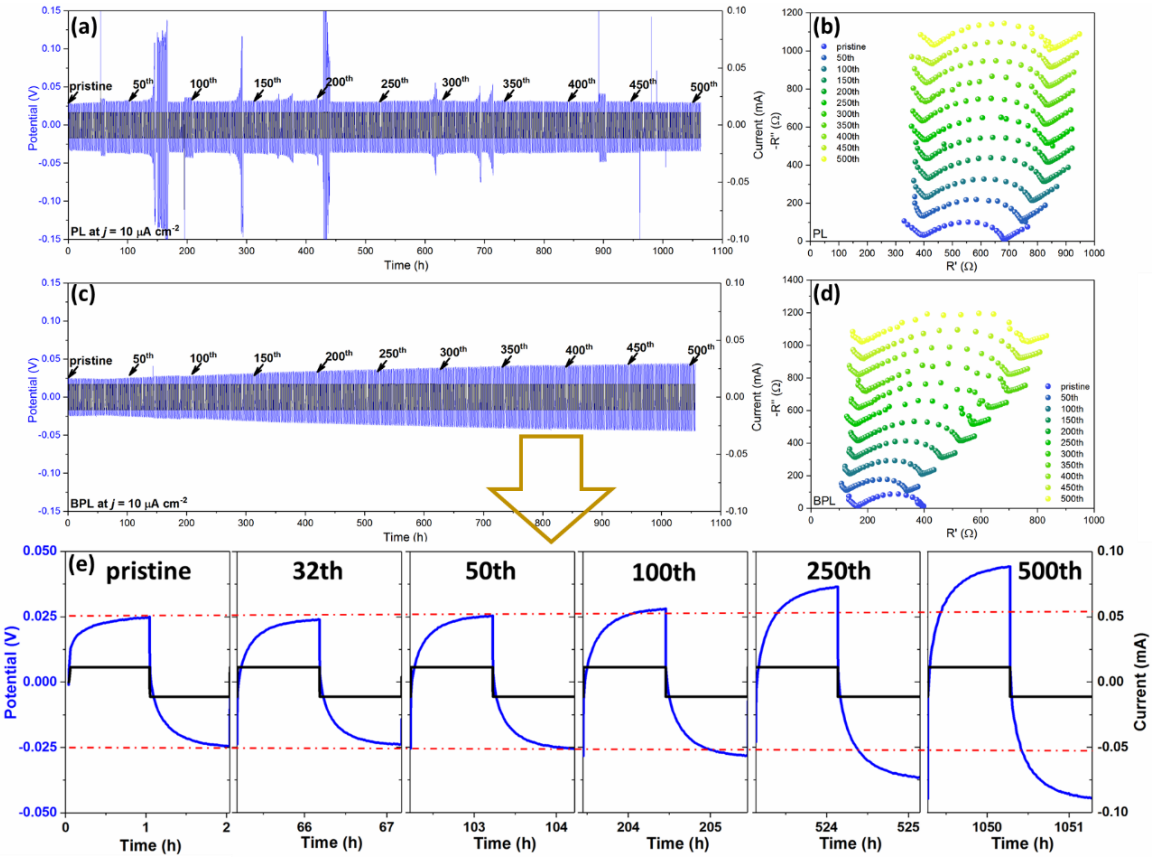

Figure 5.7. Galvanostatic stripping/plating profiles and Nyquist plots recording every 50 cycles at current density j = 10 μA cm^{-2} using the PL (a, b) and BPL (c, d) films; and selected overpotential profiles of galvanostatic cycling using the BPL film (e).

5.3.4 Battery performance

Given that ionic diffusion in the solid cathode is often the rate-limiting factor for battery capacity performance [171], 2.00 wt.% LLZ and PEO/SBR binder were applied in the cathode slurry. The LMBs were assembled by integrating a CSE film between Li anode and NCM cathode. Figure 5.8 displays SEM images of the selected EDX region of interest, which exhibits layered element distribution. Indeed, similarly to Ni mapping for the NCM cathode, La/Zr mapping enables to locate the CSE film, therefore one can observe a close contact between the BPL film and electrodes in this full cell. Since BPL film can charge below 4.5 V, the potential range for the galvanostatic cycling tests at 45 °C was set to be 2.5~4.3 V *vs.* Li/Li$^+$. As depicted in Figure 5.9a and b, the rate capacities of the NCM|CSE|Li cells decrease with increasing current densities from C/25 to 1C, which is ascribed to sluggish Li$^+$ diffusion kinetics [172]. The PL-based cell exhibits a lower rate performance (85, 25, 11, 2 and 91 mAh g^{-1} at C/25,

C/10, C/5, C/1, and C/5, respectively), compared to that using BPL film. The latter displays capacities as high as 135, 109, 101, 48 and 126 mAh g^{-1} at C/15, C/10, C/5, 1C and 5C, respectively (see Figure 5.9c). Notably, initial activation process and long responding time can allow enough Li^+ to enter electrodes for high specific capacities at high C-rates.

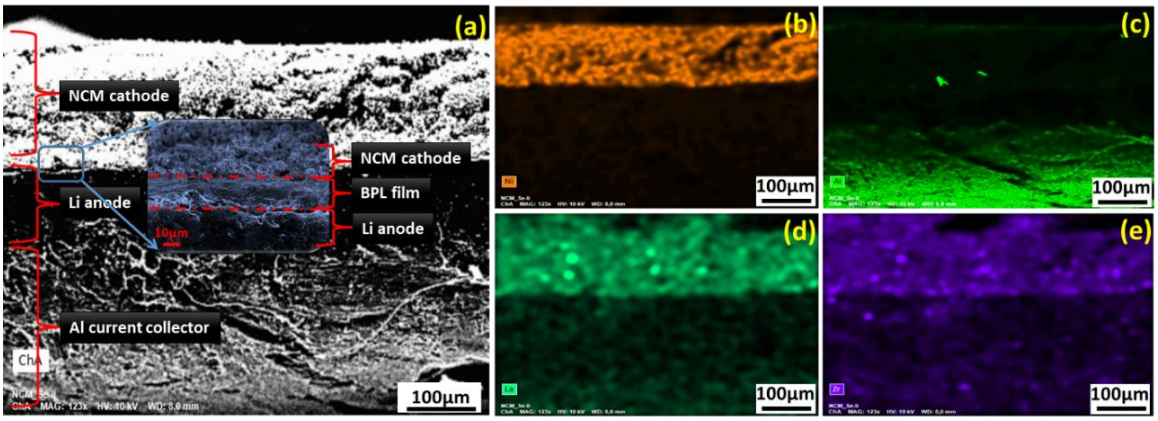

Figure 5.8. Cross-sectional SEM images of the NCM|BPL|Li (a); EDX element mapping for Ni (b), Al (c), La (d) and Zr (e).

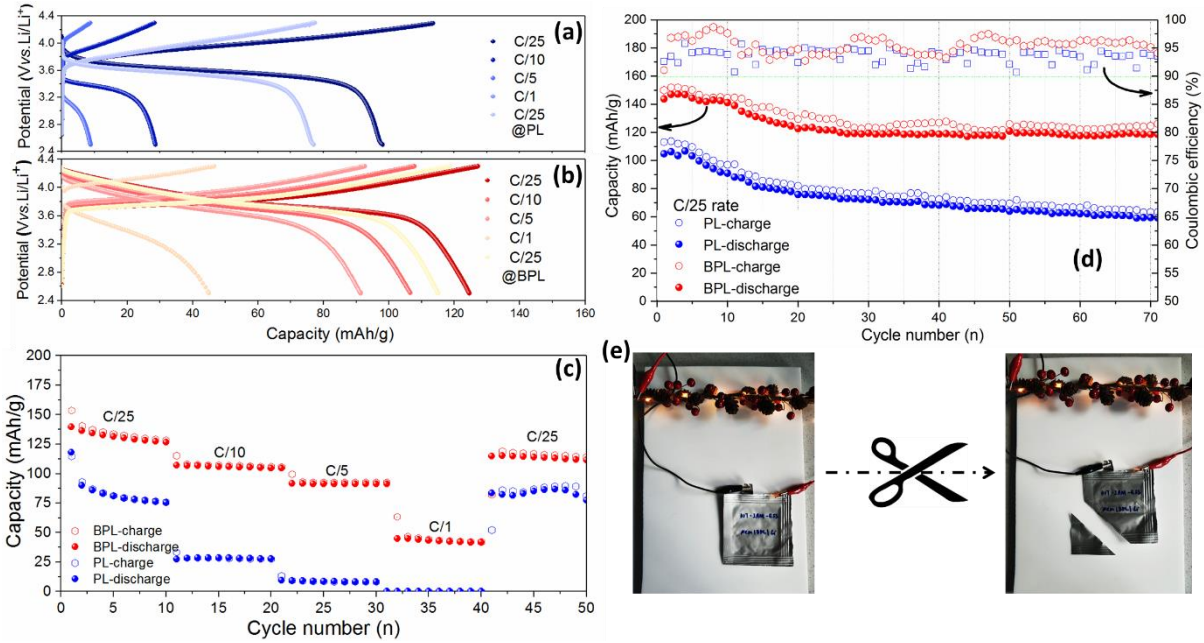

Figure 5.9. The 5th charge/discharge curves of the NCM|PL|Li (a) cell and NCM|BPL|Li cell (b) cycled at C/25, C/10, C/5; C/1 and reverse C/25, and the corresponding rate performance (c); long cycling performance (specific capacity and Coulombic efficiency) of the PL (blue) and BPL (red) based cells (d). Photographs of the pouch cell that can light up LED string lights after truncation (e).

In Figure 5.9d, capacities of the PL-based cell cycled at C/25 gradually decrease from ~105 mAh g^{-1} at the 1st cycle to ~60 mAh g^{-1} at 70th cycle. By contrast, the BPL film exhibit higher capacities (~145 mAh g^{-1} at the initial cycle and ~120 mAh g^{-1} at the 70th cycle). Importantly, the BPL-based cell displays higher Coulombic efficiency (~97%) than that of PL-based one

(~94%). This should be attributed to the improved interfacial compatibility and wettability between the BPL and the electrodes, because mobile Li^+ ions from electrodes cannot go through the PL completely due to the interfacial integrity and low migration rate [120,156]. As displayed in Figure 5.9e, a flexible pouch cell successfully lights up LED string lights. When manually truncated with a ceramic knife, the pouch cell still works without any degradation. Compared to recent reports (see Table 5.1), the BPL-based cell in this study exhibits an moderate electrochemical capacity. The electrochemical results confirm a promising application of the BPL film for electronics.

Table 5.1. Composition and electrochemical performance of the CSE film.

Ref.	Year	Solid Electrolyte	Polymerization	Conductivity	Cathode||Anode	Capacity
[173]	2016	TiO_2 gel, [EMI][TFSI], Tetrabutyl Titanate with LiTFSI	esterification hydrolysis/condensation	2.8 mS/cm	$LiFePO_4$||Li	150 mAh/g for 300 cycles at 2C
[120]	2017	silyl-polyether, LiTFSI, TEGDME, di-n-butyltin bis(2,4-pentanedionate	polymerization	0.36 mS/cm at 25 °C	$LiFePO_4$||Li	152 mA h/g at 0.1C
[165]	2016	PEO and branched acrylate; LiClO4, LiBOB and LiTFSI	UV photo-polymerization	0.22 mS/cm	$LiFePO_4$||Li	66 mAh/g at 0.5 and 5 C
[163]	2016	PEO, TEGDME, 1M LiTFSI	UV-induced polymerization	0.1 mS/cm at 25 °C	Li|TiO_2	141 mAh/g at 0.1 mA/cm at 20 °C
[174]	2016	TPGDA monomer and AIBN in LiPF6-EC/EMC/DMC	polymerization Li salt injecting	1.74 mS/cm	SiO_2 coated $LiFePO_4$||Li	159.3 mAh/g and retention of 100.2% after 200 cycles at 0.2C
[175]	2018	PEGDA-1000, PEGDE LiTFSI and BPO	one-pot polymerization	0.053 mS/cm at 30 °C	$LiFePO_4$||Li	162 mAh/g at 0.2 C and 55 °C
[152]	2017	LATP, PEO and BPEG	crosslinked	2.5 mS/cm at 60 °C	$LiFePO_4$||Li	158.2 and 94.2 mAh/g at 60 °C and 0.1C and 2C
[176]	2016	MMT, LiTFSI, PVDF and PVA	casting method	0.43 mS/cm	$LiFePO_4$||Li	123 mAh/g after 100 cycles at 0.1C
[177]	2014	PMA, PEG, $LiClO_4$, 3wt % SiO_2	sonication mixing	0.26 mS/cm	$C_{35}H_{20}O_{10}$ cathode||Li	418 mAh/g, 94.7% capacity retention after 50 cycles at 0.2C
[178]	2016	PEC with 80 wt.% LiFSI and 3D polyimide matrix	gel-casting	~10^{-5} S/cm at 30 °C	$LiFePO_4$||Li	~125 mAh/g at 30 °C and C/20
[179]	2016	PEO, BPEG, Al_2O_3 and LiTFSI	gel-casting	0.071 mS/cm at 45 °C	$LiFePO_4$||Li	132.9 and 165.1 mAh/g at 0.2C at 30 and 45 °C
[180]	2017	0.2M LiTFSI, 0.8M Pyr14TFSI, $BaTiO_3$	ball-milling	1.3 mS/cm at 30 °C	$LiFePO_4$||Li $LiCoO_2$||Li	160 and 131 mAh/g for $LiFePO_4$ and $LiCoO_2$ at 0.1C and 80 °C
[181]	2016	bisphenol A ethoxylate, BDM, DPG, LiTFSI and AIBN	in-situ free radical polymerization	0.14 mS/cm at 20 °C	PEDOT:PSS-based $LiFePO_4$ ||Li	120 mAh/g at 0.1C and RT

[93]	2017	PDEC, PTEC substituting with triethylene glycol	gel-casting	0.011mS/cm at 25℃	$LiFePO_4$‖Li $LiFe_{0.2}Mn_{0.8}PO_4$‖Li	40 mAh/g at 0.1C and 25 ℃/170 mAh/g at 0.02C and 25 ℃
[169]	2017	TPU, PEO, LiTFSI TPU/PEO = 1:3	casting	0.53 mS/cm at 60 ℃	$LiFePO_4$‖Li	112 and 127 mAh/g at 1C under 60 and 80 ℃
[182]	2015	PVA-CN in PAN membrane, LITFSI and $LiPF_6$	in situ polymerization	0.3 mS/cm at RT	$LiFePO_4$‖Li	N/A
[168]	2018	PVDF-HFP, LLZ	tape casting process	0.11 mS/cm at 25 ℃	$LiFePO_4$‖Li	110 mAh/g after 180 cycles at 0.5C
this work	2018	ED600, BADGE, LLZ, LiTFSI, PEO	crosslinked polymerization	0.53 mS/cm at 45 ℃	NCM‖Li	125 mAh/g after 70 cycles at 45 ℃

5.4 Conclusions

In this work, we designed a facile and large-scalable strategy to produce polyglycol chains, which are crosslinked by bisphenol-A segments as an amorphous matrix for Li ions. Ionic conductivity values above 45 ℃ exceeding 5.3×10^{-4} S cm^{-1} are obtained, as well as wide electrochemical stability window (> 4.51 V *vs.* Li/Li^+), high ionic diffusion coefficient (16.6×10^{-13} m^2 s^{-1}) and long cycling stability (> 500 cycles or 1000 h) that can satisfy the multiple requirements of SSBs. Wetting the electrodes by the flexible BPL film can reduce the interface resistance and distortion of Li^+ flux at the interface; the crosslinked matrix can remain the favorable Li^+ pathway at elevated temperature; garnet LLZ serves as fillers to break the ordered segmental chain improving the amorphous region. Therefore, the as-assembled NCM|BPL|Li cell displays moderate capacities (125 mAh g^{-1}) with high Coulumbic efficiency (> 97%). Remarkably, the fabricated pouch cells demonstrate high electrochemical safety under the truncation. Therefore, the BPL solid electrolyte can facilitate more advanced and safer SSB designs.

5.5 Supporting information

Table S5.1 Detailed amounts of each component in the CSE film

sample	polymer matrix	Li salt	garnet filler	preparation
PLi	PEO (350 mg)	LiTFSI (50 mg)	-	gel-casting
PL	PEO (325 mg)	LiTFSI (50 mg)	LLZ (25 mg)	gel-casting
BPL	BADGE (50 mg)+ED600 (245 mg) + PEO (30 mg)	LiTFSI (50 mg)	LLZ (25 mg)	polymerization

Table S5.2 Ionic conductivity of the PL and BPL films calculated by the equation $\sigma_t = l/A \cdot R_t$

Temperature (℃)	PL (mS/cm)		BPL (mS/cm)	
	cooling process	heating process	heating process	cooling process
5	0.0132	0.0132	0.0024	0.0024
15	0.0480	0.0313	0.0073	0.0123
25	0.1100	0.0945	0.0295	0.0393
35	0.2402	0.2115	0.0935	0.1195
45	0.5318	0.4852	0.2637	0.3307
55	2.9499	1.0102	0.5531	2.6028
65	3.8814	4.3380	2.6028	3.8814
75	4.8095	6.1455	5.0282	4.9164
85	5.1451	8.8496	8.8496	5.9794

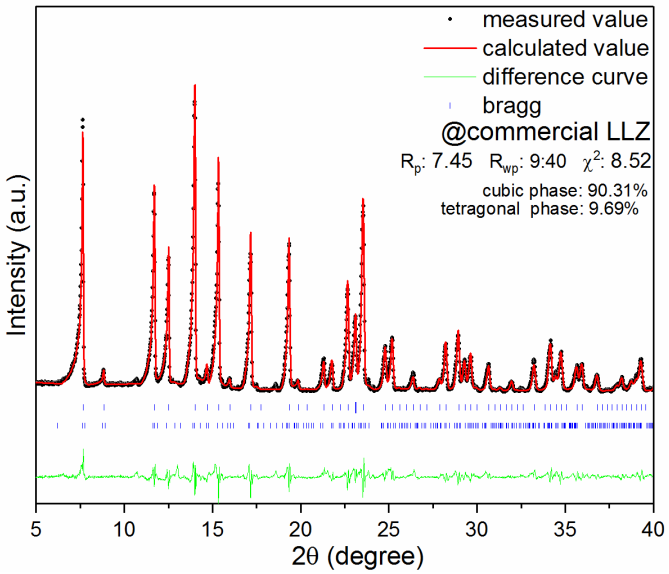

Figure S5.1 XRD Rietveld refinement of the commercial LLZ.

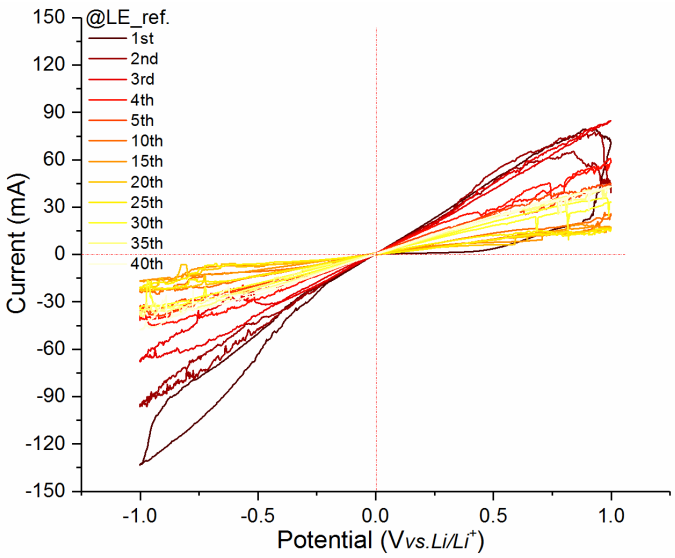

Figure S5.3. CV curves of the LP30 LE in Li symmetrical cell over -1.0 V~1.0 V.

Table S5.3 Diffusion coefficients (D_{Li}) of the PL and BPL calculated from the dc conductivity using the Nernst-Einstein relation.

Sample	℃	1000/K	Δ ms	δ ms	D $\times 10^{-13}$ m^2 s^{-1}	D_{error} $\times 10^{-13}$ m^2 s^{-1}
PL	30	3.30	150	3.00	2.4	0.06
	35	3.25	150	3.00	3.4	0.09
	40	3.19	150	3.00	5.1	0.14
	45	3.14	150	3.00	8.1	0.21
	50	3.09	150	3.00	13.1	0.33
	55	3.05	150	3.00	20.7	0.52
	60	3.00	150	3.00	39.3	0.99
	65	2.96	150	3.00	69.5	1.75
	70	2.92	150	3.00	81.7	2.03
BPL	27	3.33	175	3.21	2.5	0.33
	32	3.28	175	3.21	3.7	0.20
	37	3.23	175	3.21	6.4	0.35
	42	3.17	175	3.21	10.2	0.43
	47	3.13	175	3.21	16.6	0.80
	52	3.07	175	3.21	27.2	0.60
	57	3.03	175	3.21	49.0	1.70
	62	2.99	175	3.21	71.2	0.60
	67	2.94	175	3.21	86.0	0.90

Chapter 6 Fe stabilized $Li_7La_3Zr_2O_{12}$ solid electrolytes

6.1 Introduction

In general, SEs generally fall into three categories (sulfide-, oxide- and polymer SE) according to their frame atoms: sulfur, oxygen and carbon. In detail, polymer SEs suffer from low ionic conductivity and flammable nature; sulfide SEs are highly reactive with Li anode and moisture. Among oxide SEs garnet LLZ displays remarkable electrochemical stability against Li anode and chemical stability against moisture [122,126]. Two main structures exist in the LLZ: tetragonal phase (space group: *no. 142 $I4_1/acd$*) and cubic phase (space groups: centric *no.230 $Ia\bar{3}d$* and acentric *no.220 $I\bar{4}3d$*) [77–79]. Compared to tetragonal phase, cubic garnet LLZ displays two orders of magnitude larger conductivity (~10^{-4} S cm^{-1} at room temperature, RT), which has been proved by simulation analysis [82,83] and experiment results [70,80,81].

However, short Li–Li distances in the Li-rich cubic LLZ can destabilize the cubic phase at RT. The introduction of doping cations can lessen Li^+ density and create disordered Li-sites as well as vacancies. For example, Li^+ (24d) sites can be substituted by Al^{3+}, then followed by 96h sites and 48e sites, according to the site preference energy [183]. ~0.6 per formula unit (pfu) Li substituted by doping cations is greatly beneficial to conductivity, where the ratio of 96h/24d Li sites reach to 3:1 [74,184,185]. Therefore, trivalent or higher dopants were applied to stabilize cubic phase, *e.g.*, Al^{3+} [186], Ga^{3+} [187], Fe^{3+} [188], Ce^{3+} [189], Sc^{3+} [190], Y^{3+} [191], Bi^{3+} [192], Ge^{4+} [193], Ti^{4+} [194], Ru^{4+} [195], Ta^{5+} [128], Sb^{5+} [196], Nb^{5+} [197], Mo^{6+} [198] and W^{6+} [199]. Recently, Ga-stabilized LLZ (Ga pfu ≥ 0.15) displayed a superior electrochemical performance compared to Al-stabilized sample, because Ga^{3+} prefers to occupy tetrahedral (12a) sites, improving the Li^+ random distribution over the available sites [79,200–202]. Since the Fe^{3+}dopants can receive the same doping results as the Ga^{3+} [203,204], low-cost Fe^{3+} dopants are of particular interest to be used to improve Li^+ migration. In addition, it is important to investigate the influence of sintering temperature on the solid electrolyte, because sintering process is a necessary step to convert ceramic powders into pellets that can be integrated into solid state batteries (SSBs). Densification of the pellet needs a high sintering temperature (above 1000 °C), while too high temperatures can cause a serious Li loss from the

sub-lattice together with impurity formation (*e.g.*, $La_2Zr_2O_7$ and La_2O_3) [75,126,205]. The proper sintering temperature is crucial to achieve phase pure LLZ.

Up to now, none of the ceramic electrolytes has been widely applied due to their huge interfacial resistance [44]. An unpolished LLZ surface easily induces the growth of lithium dendrite along the cracks, due to an unbalanced current distribution, but a surface that is too flat will reduce the contact area with electrodes [206,207]. To solve this dilemma, polymer electrolytes (*e.g.*, polyethylene oxide–LiTFSI [208], poly(ethylene glycol) methyl ether acrylatetetra(ethylene glycol) diacrylate–LiTFSI [155], poly(ethylene oxide)–LLZ–Celgard film–poly(ethylene glycol) methyl ether acrylate–LiTFSI [209], poly(vinylidenefluoride–hexafluoropropylene−LP30 [210]) were introduced as a buffer layer to wet electrodes. Such hybrid solid electrolytes (HSEs) containing LLZ pellet and polymer electrolyte film can effectively improve wettability and suppress dendrite issues.

In this work, Fe doped $Li_{7-3x}Fe_xLa_3Zr_2O_{12}$ (x = 0, 0.12, 0.16, 0.20 and 0.24) were prepared via solid-state reaction. Analysis of results of Raman spectroscopy, X-ray diffraction (XRD), pair distribution function (PDF) and scanning electron microscopy (SEM) confirm that Fe^{3+} doped LLZ can lead to a stable cubic phase with disordered Li^+ arrangement; high-temperature X-ray diffraction (HT-XRD) proves that Fe doping can suppress Li loss during sintering process, and the ionic conductivity of the LLZ pellets is also obtained by the analysis of electrochemical impedance spectroscopy (EIS). In order to enlarge contact interface, an ultrathin polymer buffer is attached rigid LLZ pellet to accomplish dendrite-suppression.

6.2 Experimental methods

6.2.1 Synthesis of Fe doping LLZ

Commercial LLZ powder (NEI Corporation) and Fe_2O_3 nanopowder (purity ≥ 99.99 wt.%, Aldrich) were used without further purification. A series of $Li_{7-3x}Fe_xLa_3Zr_2O_{12}$ garnet samples with varying Fe^{3+} fractions (x = 0.00, 0.12, 0.16, 0.20 and 0.24 pfu, labeled LLZ, LLZFe0.12, LLZFe0.16, LLZFe0.20 and LLZFe0.24) were synthesized by solid-state reaction. The mixed materials in the stoichiometric fractions were sintered at 930 ℃ for 6 h using MgO crucible (ϕ 32 mm, Alfa Aesar) in a muffle furnace (P330, Nabertherm GmbH), then the powders were regrounded and pressed into a die (ϕ 15 mm) under the pressure of 435 MPa, and the second-step sintering was performed for 10 h with covering mother powder.

Bisphenol A diglycidyl ether (BADGE, 50 mg, liquid chromatography purity ≥ 95%, Sigma-Aldrich), lithium bis (trifluoromethylsulfonyl), imide (LiTFSI, 50 mg, ion chromatography purity ≥ 98.0 %, Alfa Aesar), and LLZ powder (15 mg) were stepwise added into *O,O'*-Bis (2-aminopropyl)polypropyleneglycol-block-polyethylene glycol-block-polypropylene glycol (Jeffamine® ED600, 245 mg, M_r = 600, Aldrich), and stirred with 200 rpm at 90 ℃ curing (see Figure S6.1). After degassing, the polymer sol was cast on the LLZ pellet surface in a quasi-solid-state, and the as-prepared HSE was stored in an argon-filled glovebox (MB200, Mbraun GmbH) before usage.

6.2.2 Crystal characterization

XRD was carried out using an STOE STADI P X-ray powder diffractometer equipped with a Mythen1K detector and a Mo $K_{\alpha 1}$ radiation (λ=0.7093 Å), Rietveld refinement was conducted to determine the phase purity of the garnet powders (LLZ and LLZFe*x*) after the first-step sintering. Data for PDF analysis were collected at the beamline P02.1 PETRA III (DESY, Hamburg), and a Perkin Elmer XRD1621 detector was used in conjunction with hard X-rays (~60 keV, λ=0.2072 Å). In detail, the intensity function I(Q) was calculated from the raw X-ray data using PDFgetX2 software and was corrected for the sample and instrument effects like Compton scattering, Laue diffuse scattering, self-absorption, X-ray polarization, and weighting after background subtraction. The reduced structure-function Q[S(Q)-1] was calculated based on corrected intensity function and then Fourier transformed to the pair distribution function G(r).

To demonstrate the crystal revolution during the sintering process, *in situ* HT-XRD experiments for the pristine LLZ and LLZFe powders were performed at the beamline P02.1 PETRA III (DESY, Hamburg), as shown in Figure S6.2. All samples were sealed in quartz capillaries (ϕ 5 mm) under argon atmosphere. The heating device can realize a rapid change in temperature, and an XRD pattern was taken for 2 min (including dark image) after reaching and holding the setting temperature for more than 1 min. For comparison, *ex situ* HT-XRD measurements using STOE STADI powder diffractometer (Cu $K_{\alpha 1}$ λ=1.5406 Å) was also applied to compare the phase stability of reground powder from the pellet and covered powder during the re-sintering process.

6.2.3 General characterization

Raman spectroscopy (Jobin Yvon LabRAM HR800) was conducted at 532 nm over the range of 80~900 cm^{-1} with a laser power of 25mW, 1800 lines per mm holographic grating and 100× magnification. The morphology of samples was investigated by a scan electron microscope (SEM, Merlin, Zeiss GmbH). To determine elemental distribution, energy-dispersive X-ray spectroscopy (EDS) data were collected with a Bruker XFlash (60 mm^2) EDX detector. 50 nm-thick -gold layer was sputtered on both sides of the pellet to build the blocking cell for EIS test, which was measured over a frequency range of 10^6 ~ 10^{-1} Hz and a temperature range of 25 ~ 65 °C with test cells inside a climate chamber. The obtained Nyquist plots were fitted by equivalent circuits using ZSimpWin (Ametek. Inc.), and Li^+ conductivity was calculated based on the equation $\sigma_t = l/A \cdot R_t$, where l, A and R_t are the thickness (cm), electrode surface area (cm^2) and total resistance (Ω) of the pellets, respectively.

6.2.4 Battery tests

$LiNi_{1/3}Co_{1/3}Mn_{1/3}O_2$ (NCM) cathode was prepared with a hydroxide co-precipitation method described by Hua *et al.* [132]. A typical cathode slurry was fabricated by mixing NCM powder, 2.0 wt.% PEO/SBR (51.6:48.4 in weight ratio) aqueous solution, carbon black (Super-C65, Timcal Ltd.) and LLZ at a weight ratio of 8: 1: 0.9: 0.1. The uniform slurry was coated on Al foil using a laboratory coater with doctor-blade and then dried at 80 ℃ for 12 h. A Swagelok® cell was assembled by layered stacking of Li|hybrid solid electrolyte|$LiNi_{1/3}Co_{1/3}Mn_{1/3}O_2$ (Li|HSE|NCM) under pressure of 5 MPa in the glovebox (MB200, Mbraun GmbH), here the HSE was used to enlarge contact interface by attaching polymer electrolyte (PSE) buffer on rigid LLZ pellet, and this PSE was fabricated as stated in Section 5.2.1 (see Figure S6.1). A potential range of galvanostatic charge/discharge was set to be 2.5~4.3 V (*vs.* Li/Li^+). All assembled cells were aged at 80 ℃ to ensure the components closely packed. All the electrochemical tests were performed utilizing a Bio-Logic VMP3 multichannel potentiostat.

6.3 Results and discussion

6.3.1 Initial sintering analysis

Figure 6.1a depicts digital pictures of the raw LLZ and as-prepared LLZFe powders after the initial sintering at 930 ℃, from which one can observe the white powder gradually turns to deep yellow, indicating that Fe_2O_3 was integrated into the LLZ powder after calcination. Herein,

Raman measurement was performed to elucidate the structural change after doping (see Figure 6.1b). The band intensities at ~412 cm^{-1} and ~704 cm^{-1} increase as more Fe was added due to the E_g/T_{2g} mode and A_{1g} mode of Fe_2O_3, respectively. Due to the overlapping features of the Raman spectra, it is impossible to obtain a quantitative fitting result for the polycrystalline sample [211]. The band at ~654 cm^{-1} of the LLZ and LLZFe0.12 represents the stretching of the ZrO_6 octahedral, while this band of the LLZFe0.16 shifts to ~641 cm^{-1} due to the dynamic disorder of mobile Li^+ [212,213]. The characteristic bands at ~96 and ~111 cm^{-1} for the tetragonal phase are associated with degenerated Raman modes [212]. Due to the Li^+ arrangement in tetragonal phase with low symmetry, tetragonal phase prefers to display more spectral bands in low-wave number region compared to cubic phase. In Figure 6.1c, the bands at 106, 119, 252 and 359 cm^{-1} are related to the vibration of the La-O and Li-O in cubic phase. Therefore, the raw LLZ and LLZFe0.12 display hybrid phases (cubic- and tetragonal phase), whereas rest LLZFe*x* ($x \geq 0.16$) powders show only the cubic phase.

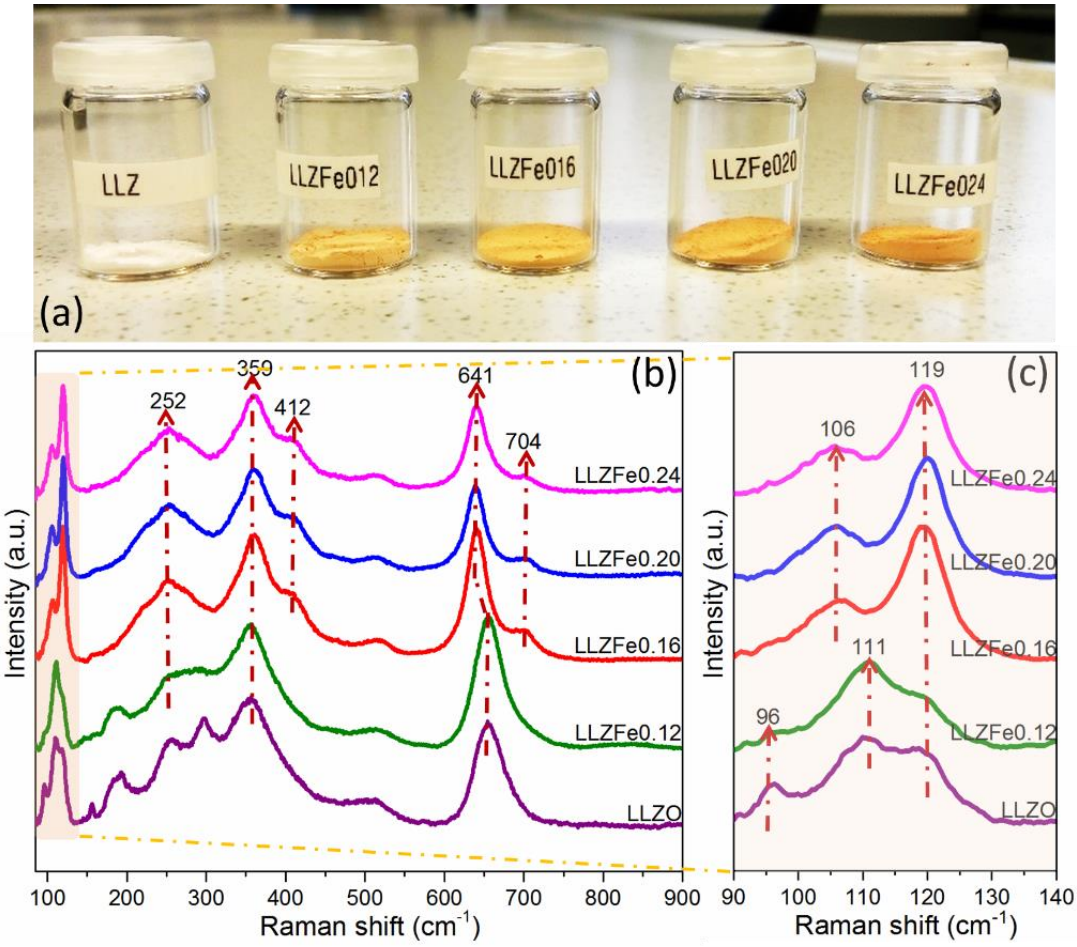

Figure 6.1 Digital pictures (a) and Raman spectra (b, c) of the LLZ and LLZFe powders after the initial sintering.

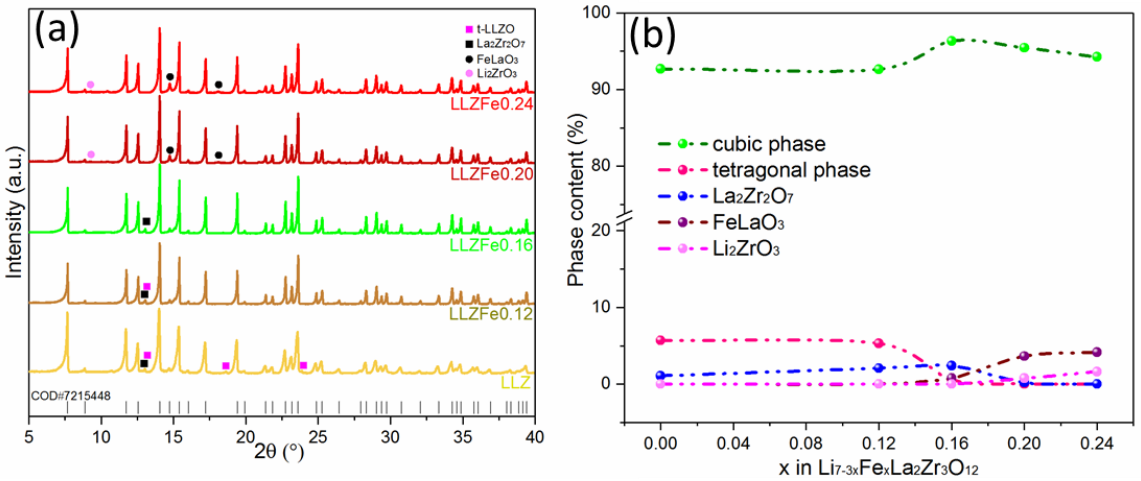

Figure 6.2. (a) XRD patterns (Mo λ=0.7093 Å) of the raw LLZ and LLZFe powders. Pattern contributions from impurity phases are marked with pink square (tetragonal phase), black square ($La_2Zr_2O_7$), black circle ($FeLaO_3$) and pink circle (Li_2ZrO_3); (b) phase content of the raw LLZ and LLZFe samples determined by Rietveld analysis.

XRD test was also performed to analyze the phase content in the doped LLZFe powders after the initial sintering (space group: $Ia\bar{3}d$, see Figure 6.2a). Combined with Raman results, 5.71% tetragonal phase and 1.60% $La_2Zr_2O_7$ are present in the raw LLZ. As shown in Figure S6.3 and Table S6.1, the content of tetragonal phase gradually decreases in the LLZFe0.12 (~5.30%) and the LLZFe0.16 (~0.57%). Notably, the tetragonal phase and $La_2Zr_2O_7$ almost disappear when doped Fe is more than of 0.16 pfu. Meanwhile, new peaks corresponding to impurities ($FeLaO_3$ and Li_2ZrO_3) can be identified, *i.e.*, the new peak at ~14.7° corresponding to $FeLaO_3$ is due to the excessive Fe doping. 3.62% $FeLaO_3$ present in the LLZFe0.20 indicates that the maximum Fe^{3+} solubility in the LLZ is below 0.20 pfu. Among them, the LLZFe0.16 exhibits the minor impurity, only 0.57% tetragonal phase and 2.33% $La_2Zr_2O_7$. Furthermore, the lattice parameter (cubic *a*) is ~13.01 Å for the non-doping LLZ, which is in agreement with previous results [192,214]. Then *a* decreases with more Fe dopant added, because the ionic radius of Fe^{3+} (78 pm) is shorter than that of Li^+ (90 pm) [203,215]. When dopant content is above 0.16 pfu Fe^{3+}, a tiny variation is observed in *a* value of around 12.70 Å. In fact, some impurities are inevitable to coexist in the garnet sample, because excessive Li source and serious Li loss can lead to stoichiometric change during the preparation process, and some impurities segregate at grain boundary during sintering and storage process [188,216,217]. The comprehensive understanding of the existence of impurities is necessary. For example, $La_2Zr_2O_7$ can be used

as a sintering agent to lessen interface impedance, while the $FeLaO_3$ is poorly conductive [218]. Therefore, 0.16 pfu Fe^{3+} is suitable to stabilize the cubic phase for the initial sintering process.

The diffuse scattering which lies between and beneath the Bragg reflections yields information of the short range and local deviations. It has weaker intensities compared to Bragg reflections and dominates at higher scattering angles in the XRD reflections. As one dimensional function, reduced PDF G(r) can distinguish two atoms separated by the real-space (r) distance, not like X-ray diffraction in reciprocal space. Hence, the real-space local structural information obtained from the corresponding PDF data provides insight into the crystal structure. Based on the low 2θ XRD pattern (see Figure S6.4 and Figure 6.3a, b), Rietveld refined structures give the similar Li^+ distribution for LLZ and LLZFe0.16, where cubic *a* are 13.0005 Å for LLZ and 12.9754 Å for LLZFe0.16. As shown in Figure S6.5, three types of ordered Li sites (tetrahedral 8a, octahedral 16f and octahedral 32g) are fully occupied in the tetragonal phase ($I4_1/acd$). In an average structure of cubic phase ($Ia\bar{3}d$), Zr atoms are located at the center of an octahedral site with six coordinated oxygen atoms around, and La atoms are situated at the center of a dodecahedral site with eight coordinated oxygen atoms around. Owing to the existence of Li vacancies induced by Fe doping, Li ions can migrate/hop in the garnet vacancy network, 7/9 Li^+ ions and 2/9 vacancies are located at tetrahedral 24d sites and octahedral 48g/96h sites, which are face-shared with each other forming a three-dimensional Li^+ pathway in the interstitial space or vacancy of the garnet framework [219,220]. Li^+ motion in the cubic phase is governed by the restriction imposed in the occupied site-to-site separation, and along only 24d-96h/96h-24d, the unstable 24d Li sites can trigger ion motion and reconfiguration of Li neighbors. In detail, the electrostatic repulsion of Li-Li and Li-Fe dopant pairs can redistribute Li^+ ions between tetrahedral and octahedral sites. Around the Fe ions, the strong repulsion blocks four nearest octahedral sites for Li^+ occupation, and vacancies are trapped as dead sites beside the dopants, and the rest octahedral sites are far away from the doping Fe as active sites, which enables fast Li^+ motion along the two neighboring tetrahedral sites in the cubic garnet [79,83,204].

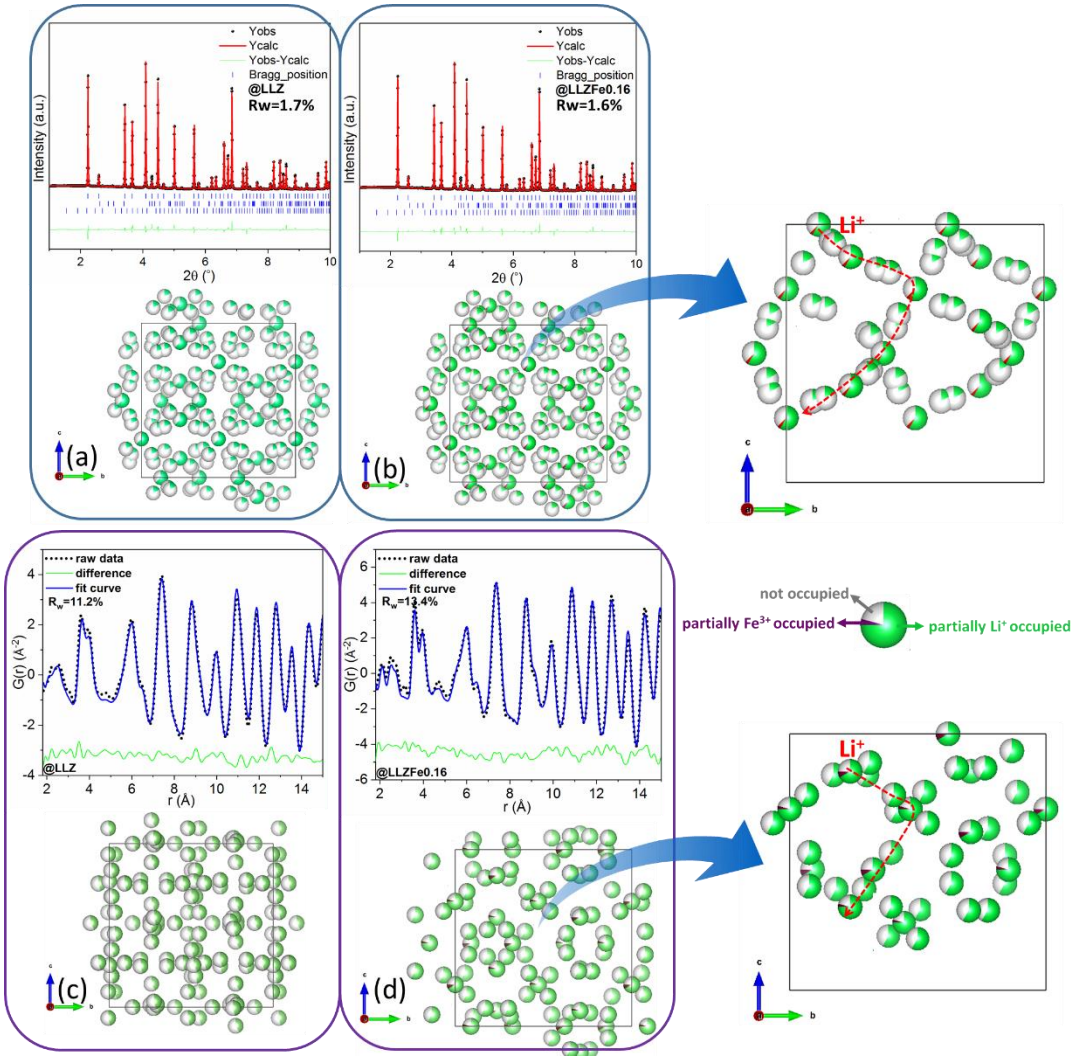

Figure 6.3 Change in Li^+ arrangement for the raw LLZ and LLZFe0.16: XRD Rietveld refinement gives the reported crystal structure (a, b), and PDF G(r) analysis gives the crystal structure model (c, d), and corresponding Li and Fe atoms distribution in the unit cell. R_w is the XRD/PDF fit residual.

In contrast, the local structure of cubic *a* in PDF fitting are 13.0281 Å (LLZ) and 12.9458 Å (LLZFe0.16), and the sharp and well-resolved peaks in PDF suggest a high symmetry and a well-defined local structure, as shown in Figure 6.3c and d. The peak at ~1.9994 Å is ascribed to Li-O vector for LLZ, while there are three vectors for LLZFe0.16 (~1.8399/2.0837/2.2861 Å). The diversity of Li-O distance is due to the local distortion around Li^+. Doped Fe located in tetrahedral sites can promote random distribution of Li^+ over the available sites improving the conductivity [221]. Therefore, the difference between the average structure and the local structure of the Li^+ arrangement was evident based on Rietveld refinement and PDF fitting (see Figure 6.3b and d).

6.3.2 Re-sintering analysis

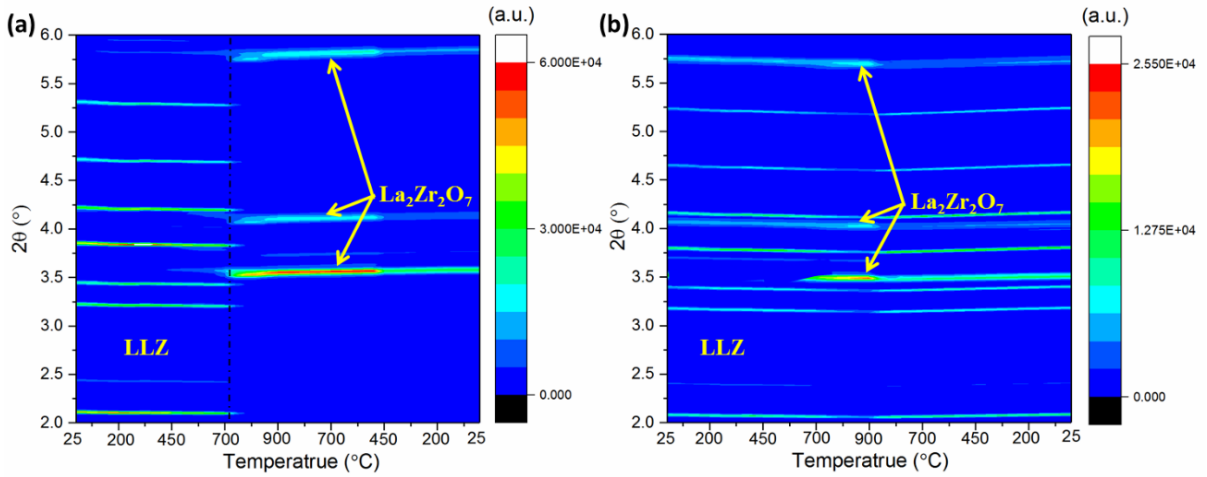

Figure 6.4. In situ HT-XRD patterns of LLZ (a) and LLZFe0.16 (b) at a temperature range of 25 °C → 900 °C →25 °C.

Sintering is the basic process of compacting garnet powder into the ceramic pellet, which plays a crucial role in determining the bulk crystallinity, grain boundary, and porosity of pellets [222–225]. *In situ* X-ray characterization could help to provide direct insights into structural changes. In this study, the phase stability of the raw LLZ and LLZFe0.16 during the sintering was investigated by *in situ* HT-XRD. As displayed in Figure 6.4a, the major phase change of the pristine LLZ occurs up to 750 °C, where $La_2Zr_2O_7$ is formed due to a serious Li volatilization from the lattice. In contrast, the LLZFe0.16 exhibits a reversible phase transformation (see Figure 6.4b). The diffraction peaks shift to lower angles with the stepwise heating, and reverse to original positions once the stepwise cooling was completed. This is explained by the linear thermal expansion of the cubic unit cell at high temperature [159]. Although tiny $La_2Zr_2O_7$ coexists in the LLZFe0.16 above 750 °C, it clearly shows a stable cubic phase up to 900 °C, indicating that Fe^{3+} doping can repress Li loss compared to the Fe-free garnet sample. The Fe doping induces amorphous Li_2O-Fe_2O_3 phase in the grain boundary, acting as a sintering agent and blocking Li loss during the sintering process [76,184]. The intensity of the cubic peaks above 750 °C drops due to the atom dynamic disorder. It is noteworthy that previous works report that the sintering temperature for cubic LLZ is above 1100 °C [203,226–229]. The difference stands from the fact that a tiny amount of the garnet specimen easily leads to an earlier evaporation of Li source. In the experiment, the fresh pellet should be covered with mother powder to repress Li loss [205,230,231]. E*x situ* XRD patterns of the LLZFe0.16 powder from reground pellets and corresponding cover powders are

displayed in Figure S6.6, which confirms that the $La_2Zr_2O_7$ appears at 930℃ and 1130 ℃ for the LLZFe0.16- powder and pellet, respectively. This proves that covering mother powder is effective in repressing Li loss from the pellet.

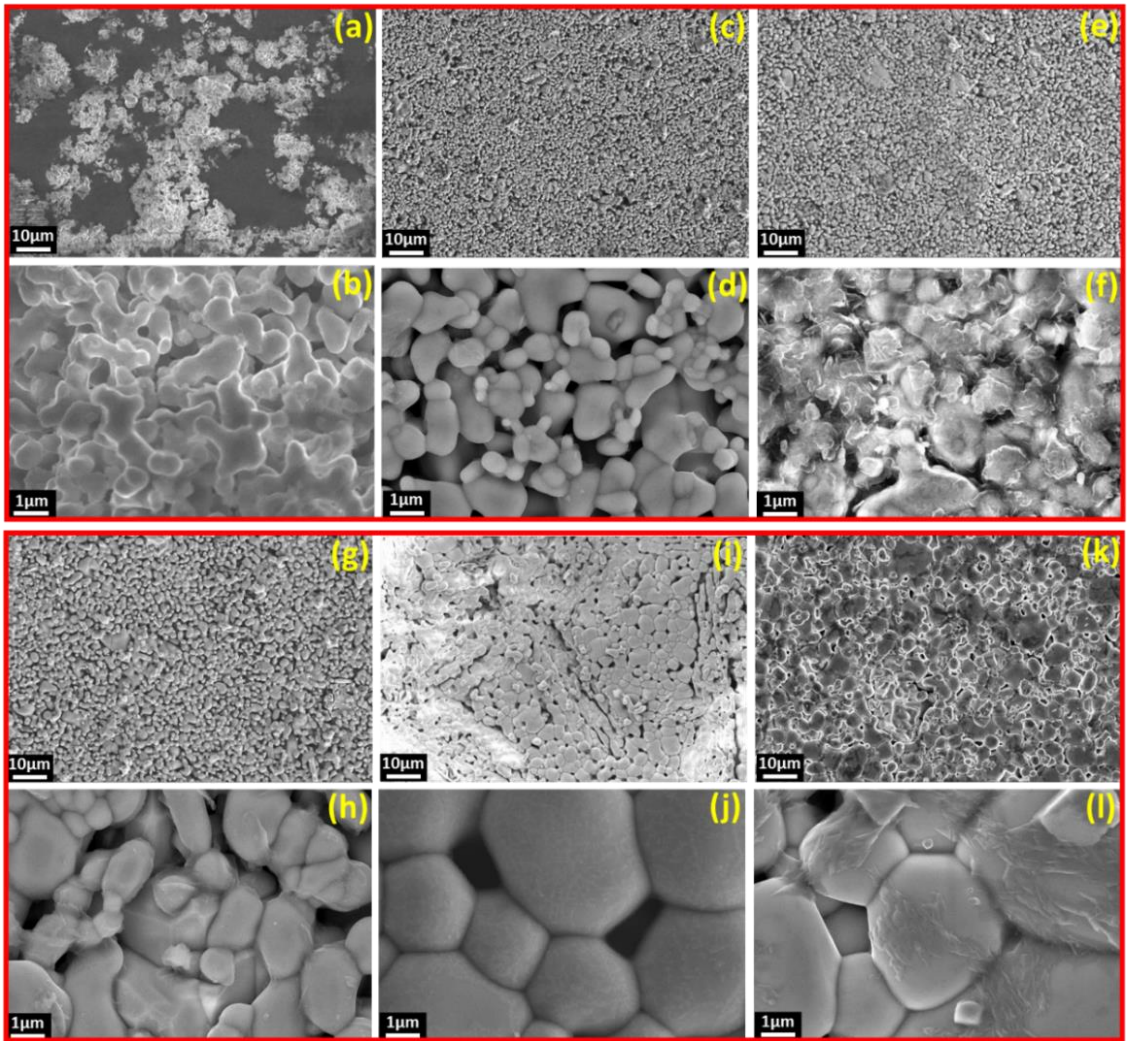

Figure 6.5. SEM images of the LLZFe0.16 powder (a, b) and its pellets re-sintered at 730 ℃ (c, d); 830 ℃ (e, f); 930 ℃ (g, h); 1030 ℃ (i, j) and 1130 ℃ (k, l).

Figure 6.5 depicts SEM surface images of the LLZFe0.16 pellets sintered at varying temperatures, from which it can be seen that particles' size increases as the temperature goes up, and a broader size distribution of the particles is observed at a higher re-sintering temperature. As shown in Figure 6.6a, average sizes of garnet particles are calculated from the analysis with Zeiss SmartTiff software: raw powder (a&b, 743±194 nm) and the pellet re-sintered at 730 ℃ (c&d, 941±306 nm), 830 ℃ (e&f, 1033±352 nm), 930 ℃ (g&h, 1267 nm±497), 1030 ℃ (i&j, 2823±1172 nm) and 1130 ℃ (k&l, 3839±1549 nm). This behavior can be explained by Ostwald ripening, where small particles tend to dissolve and deposit again on the surface of larger particles. Some buffer layer attached to the large particles is observed in

Figure 6.5f, h and i, suggests an unfinished ripening process. As shown in Figure 6.5i-l, garnet powders in the pellets tend to stack more closely, and a remarkable grain growth occurs above 1030 ℃, which is beneficial to low grain boundary resistance and high ionic conductivity. EDX mapping for the elemental localization was performed on the LLZFe0.16 pellet (see Figure 6.6b-e), confirming that La, Zr and Fe are homogeneously dispersed on the pellet. It is noted that pellet's diameter shrinks slightly from ϕ 15.0 mm to ϕ 13.1 mm. Considering Li loss and phase purity, 1030 ℃ is chosen as the re-sintering temperature for Fe stabilizing LLZ pellet. Unlike other superionic conductors that are sensitive to air and moisture, the garnet oxide is stable for processing in dry air, and they has sufficient mechanical strength for handling scalable fabrication [232].

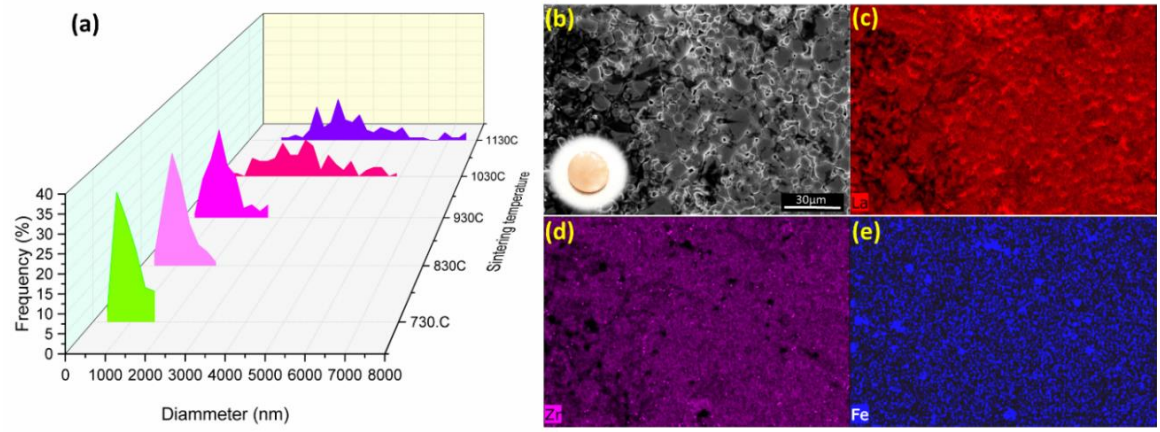

Figure 6.6. The average sizes of garnet particles in the LLZFe0.16 pellet at varying re-sintering temperature; SEM images of the LLZFe0.16 pellet re-sintered at 1030 ℃ (a) and its EDX mapping for La (b), Zr (c) and Fe (d).

6.3.3 Ionic conductivity

In order to investigate the doping influence on the ionic conductivity, EIS test was employed at 45 ℃ for LLZ and LLZFe0.16 pellets after re-sintered at 1030 °C. As shown in Figure 6.7a and b. All Nyquist plots display high-frequency semicircles followed by sloping lines toward low frequencies in the complex impedance plane, and the semicircle decreases as temperature goes on due to the temperature-dependent resistance [203]. It is notable that the gold sputtering layer can improve the connection between the LLZFe pellet and the collector (see Figure 6.7c). According to impedance spectroscopy, an equivalent circuit of $R_e(R_bCPE_1)(R_gCPE_2)W_a$ was established in accordance with Li^+ motion in the SE, where R is the resistance, CPE is the constant phase element, and the subscript **e**, **b** and **g** refer to the

external circuit, bulk- and grain-boundary contribution (see Figure 6.7d). The semicircle can be ascribed to the action of bulk resistance (Li^+ ions go through crystal lattice or twin crystal) and grain boundary resistance (Li^+ ions transfer across the grain boundary), which were resolved through the fitting analysis of Nyquist plot [96,140]. Figure 6.7e and Table S6.2 prove that grain boundary resistance is one order of magnitude larger than bulk resistance, and Fe-doped LLZ has a higher conductivity than the undoped LLZ. Wagner *et al.* calculated the high bulk ionic conductivity of Fe-doped LLZ (1.38×10^{-3} S cm^{-1} at RT) [203], but the grain boundary resistance was a major problem to overcome and should be addressed. In this study, the LLZFe0.16 exhibits the total ionic conductivities of 1.76×10^{-5} S cm^{-1} at RT and 1.99×10^{-5} S cm^{-1} at 45 °C, respectively.

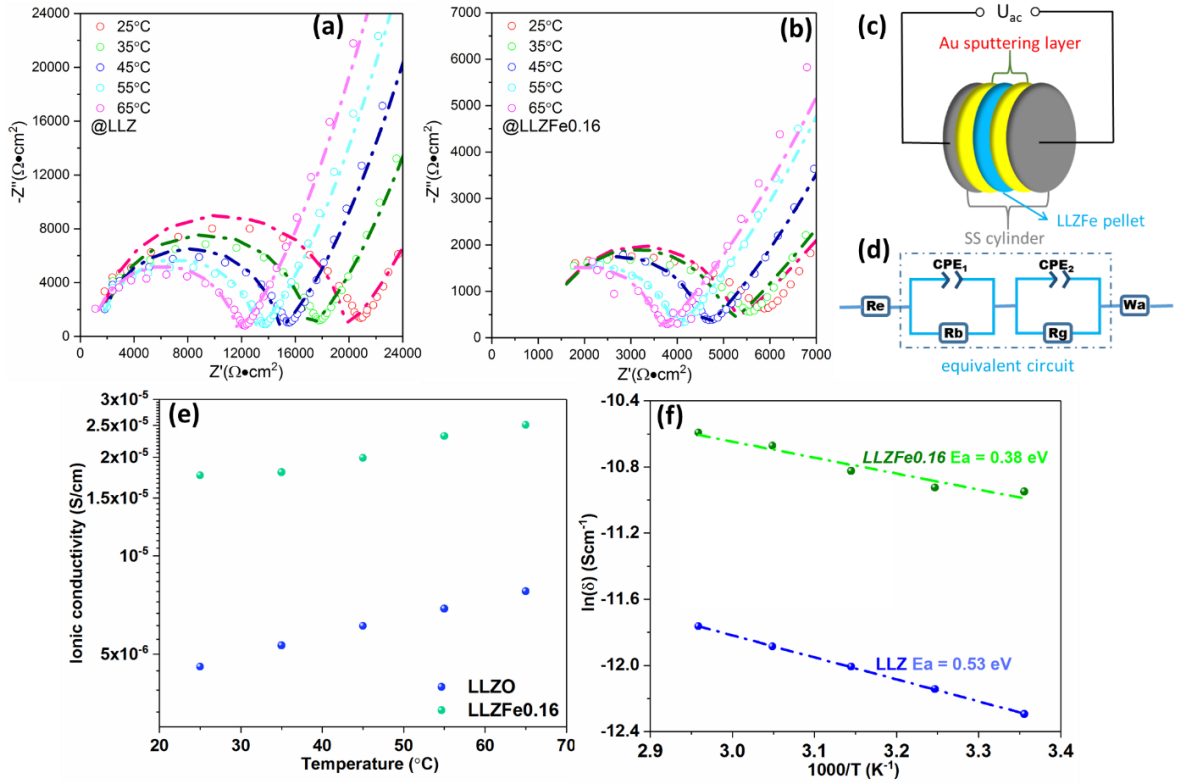

Figure 6.7. Nyquist plot and fitting curves of the raw LLZ (a) and LLZFe0.16 (b) pellets; (c) diagram for AC impedance measurements, garnet pellet sputtered with gold layer; (d) the equivalent circuit used to fit EIS data; temperature-dependent total ionic conductivity (e), and total conductivities for Arrhenius plots of the LLZ and LLZFe0.16 pellets (f).

The behavior of Li^+ diffusion in garnet structure can be normally characterized by an Arrhenius relation due to the energy barrier of Li^+ hoping in the lattice [145]. The activation energy E_a was calculated based on the following equation from 25 °C to 90 °C:

$$E_a = -R[(\partial ln\delta/\partial(1/T))]$$

where δ is total ionic conductivity ($S \cdot cm^{-1}$), R is gas constant (8.31446 $J \cdot mol^{-1} \cdot K^{-1}$) and T is the testing temperature (K). In detail, E_a was determined from the slope of $ln(\delta)$ *vs.* $1000/T$ plot. The Arrhenius graph in Figure 6.7f shows that the activation energy is ~0.53 and ~0.38 eV for the LLZ and LLZFe0.16, which are comparable to the reported value (0.45 eV) [233]. The high ionic conductivity and low activation energy of the LLZFe0.16 pellets are ascribed to phase content and doping effect. Table 1 summarizes the reported doping result in garnet SE. Most reports have proved that trivalent cations prefer to occupy 12a or 24d Li^+ sites, and higher valence can even replace Zr^{4+} sites. The x = 0.16 is close to optimal Li content (0.10~0.25) in $Li_xA_3B_2O_{12}$ garnet required to achieved the high Li^+ conductivity.

Table 1 Effects of metallic doping on ionic conductivity and re-sintering temperature in the literature.

Dopant	Substituted sites	Formula (optimum doping value)	Ionic conductivity	Reinterring T	Ref.
Al^{3+}	24d >96h >48g >16a ≫ 24c Li^+	$Li_{7-3x}Al_{3+x}La_3Zr_2O_{12}$	DFT analysis	-	[183]
Al^{3+}	24d Li^+	$Li_{7-3x}Al_xLa_3Zr_2O_{12}$ (x=0.25)	-	1050 °C	[234]
Al^{3+}	24d Li^+/ La^{3+}/Zr^{4+}	$Li_{7-3x+z}Al_{x+y+z}La_{3-y}Zr_{2-z}O_{12}$	10^{-5}~10^{-4} Scm^{-1} at RT	-	[235]
Al^{3+}	Zr^{4+}	$Li_7La_3Zr_{2-0.75x}Al_xO_{12}$ (x=0.15)	3.4×10^{-4} Scm^{-1} at RT	1150 °C	[236]
Al^{3+}/Ga^{3+}	24d&96h Li^+	$Li_{7-3(x+y)}Ga_xAl_yLa_3Zr_2O_{12}$	10^{-3}~10^{-4} Scm^{-1} at RT	1050 °C	[237]
Ga^{3+}	24d Li^+	$Li_{5.5}La_3Zr_2Ga_{0.5}O_{12}$	1×10^{-4} Scm^{-1} at RT	1000 °C	[238]
Ga^{3+}	Li^+	$Li_{7-3x}Ga_xLa_3Zr_2O_{12}$ (x=0.20)	4.0×10^{-4} Scm^{-1} at RT	600 °C	[187]
Ga^{3+}	Li^+	$Li_{7-3x}Ga_xLa_3Zr_2O_{12}$ (x=0.15)	1.6×10^{-3} Scm^{-1} at RT	-	[200]
Ga^{3+}	96h Li^+	$Li_{7-3x}Ga_xLa_3Zr_2O_{12}$	4.1×10^{-4} $S \cdot cm^{-1}$ at RT	1050 °C	[239]
Ga^{3+}	24d Li^+	$Li_{7-3x}Ga_xLa_3Zr_2O_{12}$	-	850 °C	[79]
Ga^{3+}/Sc^{3+}	24d Li^+/Zr^{4+}	$Li_{7-3x+y}Ga_xLa_3Zr_{2-y}Sc_yO_{12}$ (x = 0.15, y=0.10)	1.84×10^{-3} Scm^{-1} at RT	1200°C	[240]
Fe^{3+}	24d Li^+	$Li_{7-3x}Fe_xLa_3Zr_2O_{12}$ (x=0.16)	-	1050 °C	[188]
Bi^{3+}	$Li^+/Zr4^+$	$Li_{7-x}La_3Zr_{2-x}Bi_xO_{12}$ (x=0.20)	2.6×10^{-5} Scm^{-1}	1100°C	[241]
Ga^{3+}	12a Li^+	$Li_{7-3x}Ga_xLa_3Zr_2O_{12}$	-	850 °C	[79]
Al^{3+}/Ga^{3+}	24d Li^+	$Li_{6.4}Al_{0.2-x}Ga_xLa_3Zr_2O_{12}$ (x=0.15)	1.2×10^{-3} Scm^{-1}	1230 °C	[214]
Fe^{3+}	12a Li^+	$Li_{7-3x}Fe_xLa_3Zr_2O_{12}$	1.38×10^{-3} Scm^{-1} at RT	1230 °C	[203]
Ti^{4+}	$Zr4^+$	$Li_7La_3Zr_{2-x}Ti_xO_{12}$ (x = 0.3)	4.2×10^{-3} Scm^{-1} at 30 °C	1180 °C	[194]
Ba^{2+}/Ta^{5+}	La^{3+}/Zr^{4+}	$Li_{6.5}La_{3-x}Ba_xZr_{1.5-x}Ta_{0.5+x}O_{12}$ (x=0.10)	8.34×10^{-4} Scm^{-1} RT	1100°C	[205]
Ta^{5+}	Li^+/Zr^{4+}	$Li_{7-x}La_3Zr_{2-x}Ta_xO_{12}$ (x=0.6)	1.0×10^{-3} Scm^{-1} at RT	1140 °C	[184]
Sb^{5+}	Li^+/Zr^4	$Li_{6.925}La_3Zr_{1.925}Sb_{0.075}O_{12}$	3.40×10^{-4} Scm^{-1}	1160 ℃	[196]
Nb^{5+}	Li^+/Zr^{4+}	$Li_{7-x}La_3(Zr_{2-x}Nb_x)O_{12}$ (x=0.25)	8×10^{-4} Scm^{-1} at RT	1200 ℃	[197]
W^{6+}	Li^+/Zr^{4+}	$Li_{7-2x}La_3Zr_{2-x}W_xO_{12}$ (x=0.2)	8.7×10^{-5} Scm^{-1}	1050 °C	[242]
Mo^{6+}	16a Li^+/Zr^{4+}	$Li_{7-2x}La_3Zr_{2-x}Mo_xO_{12}$ (x = 0.25)	3.4×10^{-4} Scm^{-1} at RT	700 °C	[198]
Fe^{3+}	12a Li^+	$Li_{7-3x}Fe_xLa_3Zr_2O_{12}$ (x = 0.16)	1.76×10^{-5} Scm^{-1} at RT	1030 °C	this work

6.3.4 Battery performance

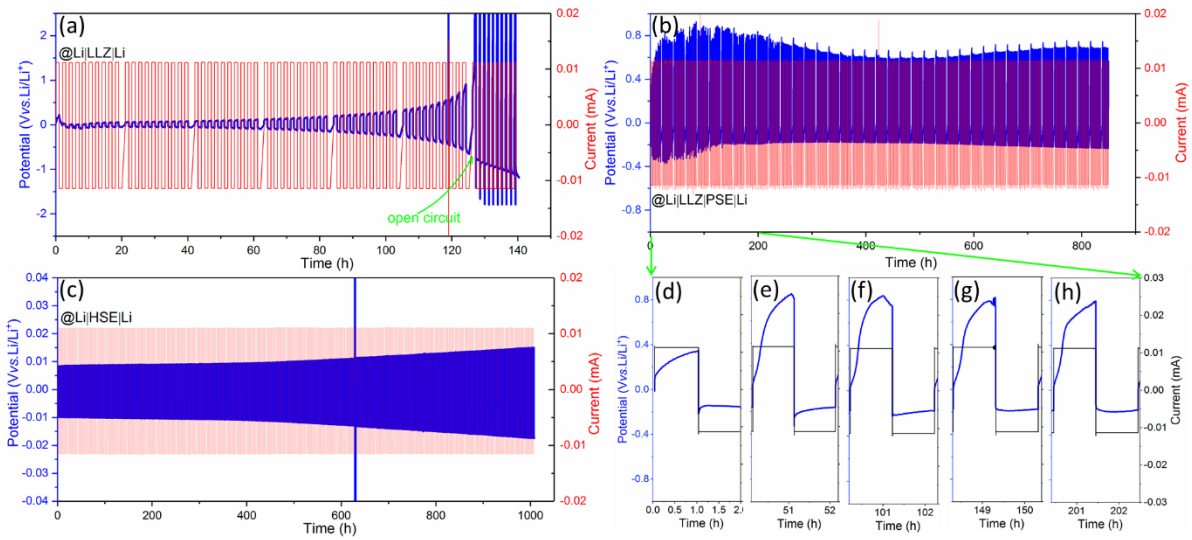

Figure 6.8. Voltage profiles of the lithium striping/plating process in the Li symmetric cells using LLZ pellet (a), LLZ pellet+PSE film (b) and HSE (c); and selected overpotential profiles of Li symmetric cell using LLZ pellet+PSE film cycling (d).

Considering its high ionic conductivity, high shear modulus and high stability with Li metal, the LLZFe0.16 pellet was used for further electrochemical characterization. However, the drawbacks of high brittleness, high mass density, poor surface contact and dendrite growth along the garnet cracks [155,208]. To avoid the issues stated above and enhance wettability, one effective strategy is to integrate both polymer and inorganic SE into a hybrid solid electrolyte (HSE) [220]. To compare the cycling stability of the garnet pellet and HSE, Li symmetric cells were constructed and charge/discharge cycled at 45 °C. Figure 6.8a shows the cycling performance of the cell using a single pellet at a current density of 1.0 μA cm^{-2}. The cell voltage firstly drops due to the initial activation, then the voltage gradually increases until open-circuit occurs after the 128th cycle, evidenced by the sudden voltage rise. In contrast, HSE-based Li symmetric cell displays a stable lithium plating /stripping more than 1000 h under the same conditions, suggesting a superior long-term reversibility without dendrite growth (see Figure 6.8c). To study the overpotential disturbance and interactive effect between PSE and LLZ, LLZ | PSE-based Li symmetric cell was assembled. The voltage profiles of LLZ with PSE film attached exhibit stable potential curves (downside, see Figure 6.8b and d–h), whereas the other side (upside) is a messy one. Thus, the close interface offers sufficient channels for Li ions to move from lithium foil to electrolyte, and this efficient strategy can significantly reduce the interface issues and suppressing uneven Li deposition during cycling.

Thus, the HSE film can exhibit superior cycling stability against electrode and repress the growth of lithium dendrite.

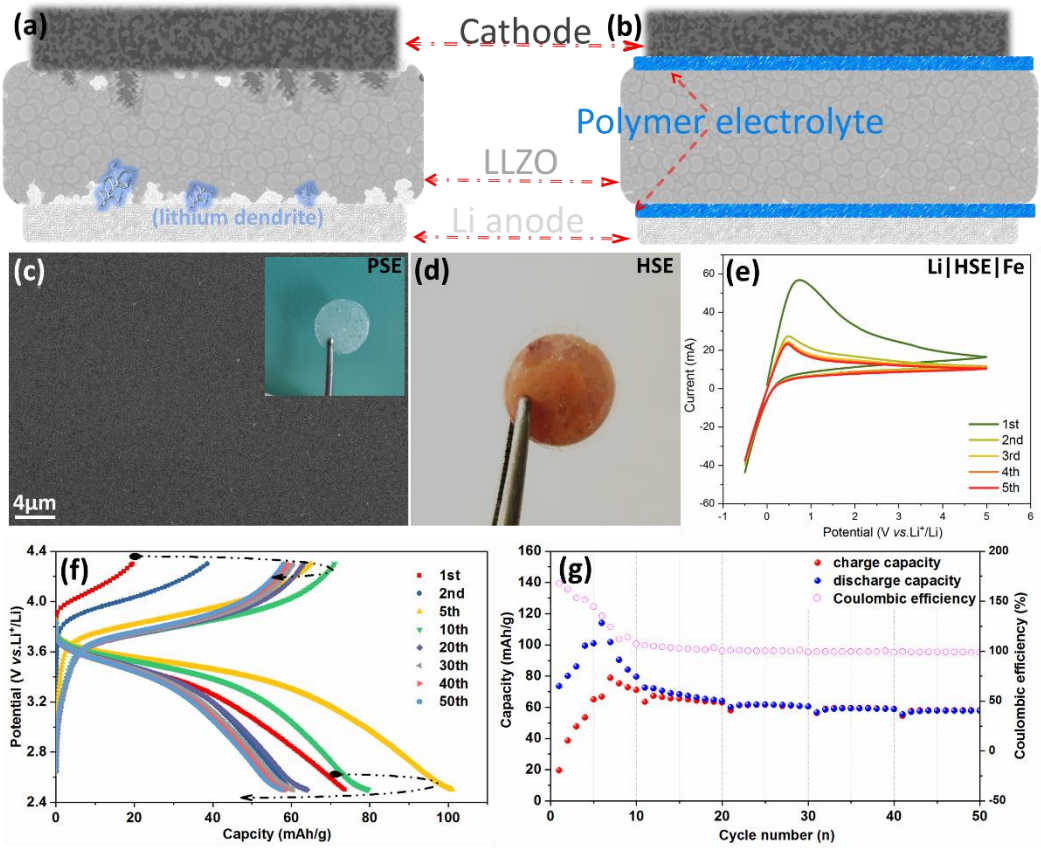

Figure 6.9. Schematic representation of lithium dendrite along the cracks in the garnet pellet (a) and stable interface in the HSE (b); (c) SEM image of the polymer electrolyte film and its digital graph; (d) the digital graph of the HSE; (e) CV curve of Li|HSE|SS cell at a potential range of -0.5~5 V at a scan rate of 0.1 mV s^{-1}; (f) galvanostatic charge/discharge profiles of the Li|HSE|NCM cell; (g) cycling performance and Coulombic efficiency at 2.5~4.3 V (vs. Li/Li^+) and at 45 °C.

Therefore, the superior cycling ability due to uniform current distribution through the interface, as illustrated in Figure 6.9a *vs.* b. In Figure 6.9c, the SEM image of the polymer electrolyte clearly shows the uniform surface. The interlinked polymer attached to LLZ pellet provides an amorphous buffer layer for dissolution and migration of mobile Li^+ (see Figure 6.9d). A 2032 coin cell consisting of Li|HSE|SS was used to examine the electrochemical stability windows of the HSE. The anodic scans of the CV curves in Figure 6.9e display reproducible current peaks at ~0.5 V, except the 1st scan due to the formation of SEI layer [151]. There is no severe anodic current fluctuation below 5.0 V, which indicates that the HSE is electrochemically stable above 5.0 V. In contrast, the electrochemical stability window of PEO based electrolyte is less than ~3.5 V due to the decomposition of the PEO and Li salt [131,151].

Because the existence of garnet pellet reduces the magnitude of the electric field across the HSE, higher electrochemical stability windows can be achieved here [155]. In Figure 6.9f, the assembled full battery shows a low 1st charge capacity ~20 mAh g^{-1} at C/25, compared to the 1st discharge capacity of ~73 mAh g^{-1}. This is due to Li consumption and storage in the interface. Afterwards, charge capacity gradually increases and Coulombic efficiency drops below 100% after the 8th cycle (Figure 6.9g). Then highly reproducible capacity was obtained in following cycles, verifying that the HSE can serve as an acceptable electrolyte in the LMBs.

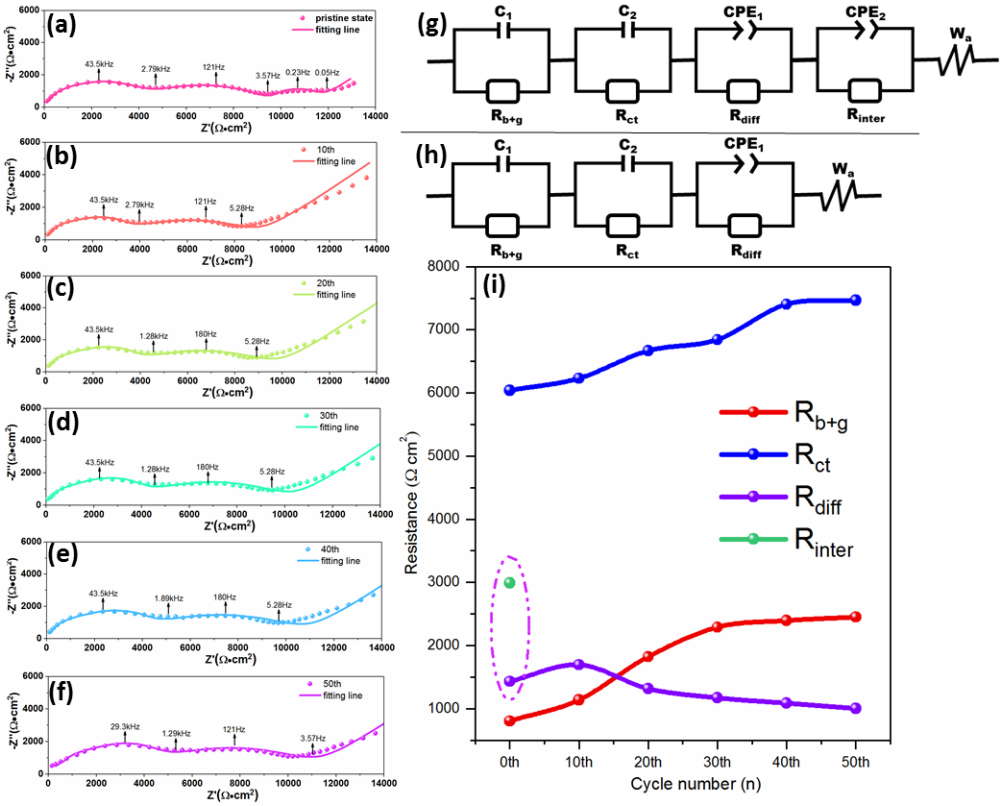

Figure 6.10. Impedance analysis of the Li|HSE|NCM cell during the cycling process: Nyquist plots recorded every ten cycles (a-f); equivalent circuits for different status cells (g-h) and the fitting results of resistances (i).

To investigate dynamic resistance, Nyquist plots were recorded in every ten cycles during long cycling (Figure 6.9f). The plots in Figure 6.10a show three semicircles in the fresh electrode assuming that at least three basic reactions occur across the entire frequency range. Based on Liu *et al.* work [210], an equivalent circuit ($(R_{b+g}C_1)(R_{ct}C_2)(R_{diff}CPE_1)(R_{inter}CPE_2)W_a$) (Figure 6.10g) was proposed for the fresh cell, containing the bulk and grain boundary impedances (R_{b+g}) of the garnet pellet in the high frequency region, the interfacial charge transfer resistance (R_{ct}) in medium frequency region, the diffusion impedance (R_{diff}) and interface contact impedance (R_{inter}) at low frequency region. In contrast, the rest Nyquist plots

display only two semicircles after electrochemical activation (Figure 6.10b-f), which can differentiate the contribution of R_{b+g}, R_{ct} and R_{diff}, and the corresponding equivalent circuit was $((R_{b+g}C_1)(R_{ct}C_2)(R_{diff}CPE_1)W_a)$ (see Figure 6.10h). In Figure 6.10i, the fitting result confirms that the total resistance gradually increases at subsequent cycles, mainly due to an increase in the R_{b+g} and the R_{ct}. As cycled, the resistance from growing SEI layer will slow down the Li^+ transfer.

6.4 Conclusions

In this study, Fe^{3+} doping is applied to stabilize the cubic phase LLZ, and the effects of doping and sintering temperature on the phase purity and ionic conductivity were studied. Raman spectra, Rietveld refinement, and PDF analysis determined that the LLZFe0.16 powder sintered at 930 °C is cubic phase (~96%) with more disordered Li^+ sites. The HT-XRD analysis confirms that Fe^{3+} doping can enhance the structural stability during the high-temperature sintering. Based on EIS analysis, the increase in ionic conductivity is associated with the Fe^{3+} amount and the disordered Li content in the garnet structure. The LLZFe0.16 pellet shows a high total ionic conductivity (1.99×10^{-5} Scm^{-1} at 45 °C) with low porosity. Importantly, the HSE film shows a high stability against metallic Li due to the strong wettability of the PSE. The constructed solid-state LMBs exhibited good capacity retention (65 mAh g^{-1} after 50^{th} cycle), because a PSE layer was attached to the LLZ disk and enhanced the mechanical resilience of the structure. In addition, if compared to the conventional liquid electrolyte, the HSE can not only reduce the safety concerns regarding the flammability of organic solvent, but it can also realize a facile fabrication of other types of HSEs as well.

6.5 Supporting Information

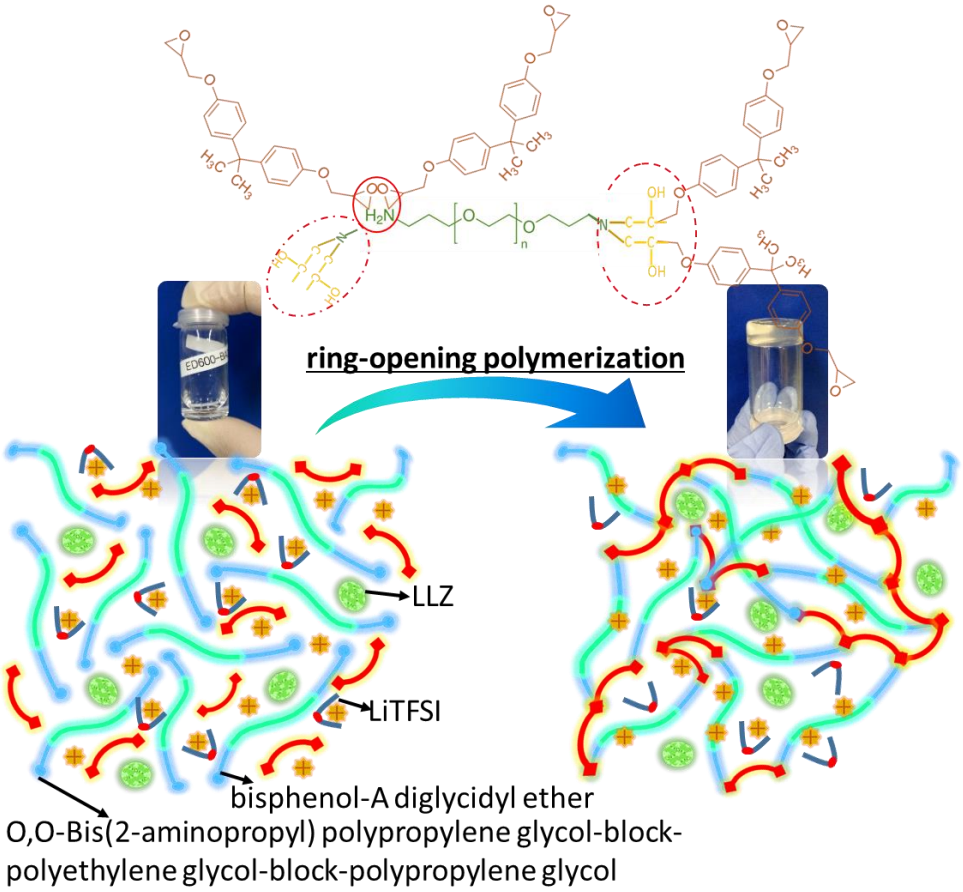

Figure S6.1 Conceptual illustration of the solvent-free ring-opening polymerization of O,O-Bis(2-aminopropyl)polypropylene glycol-block-polyethylene glycol-block-polypropylene glycol (ED600), bisphenol-A diglycidyl ether (BADGE) and lithium bis(trifluoromethylsulfonyl)imide (LiTFSI). Photographs of the homogeneous precursor sol and crosslinked BPL gel.

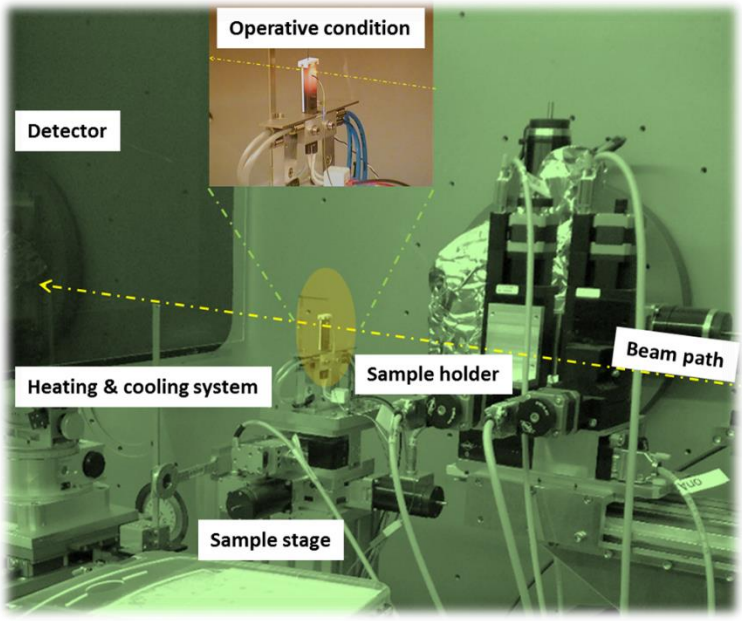

Figure S6.2. Device overview of the in situ HT-XRD at the beamline P02.2 PETRA III in DESY.

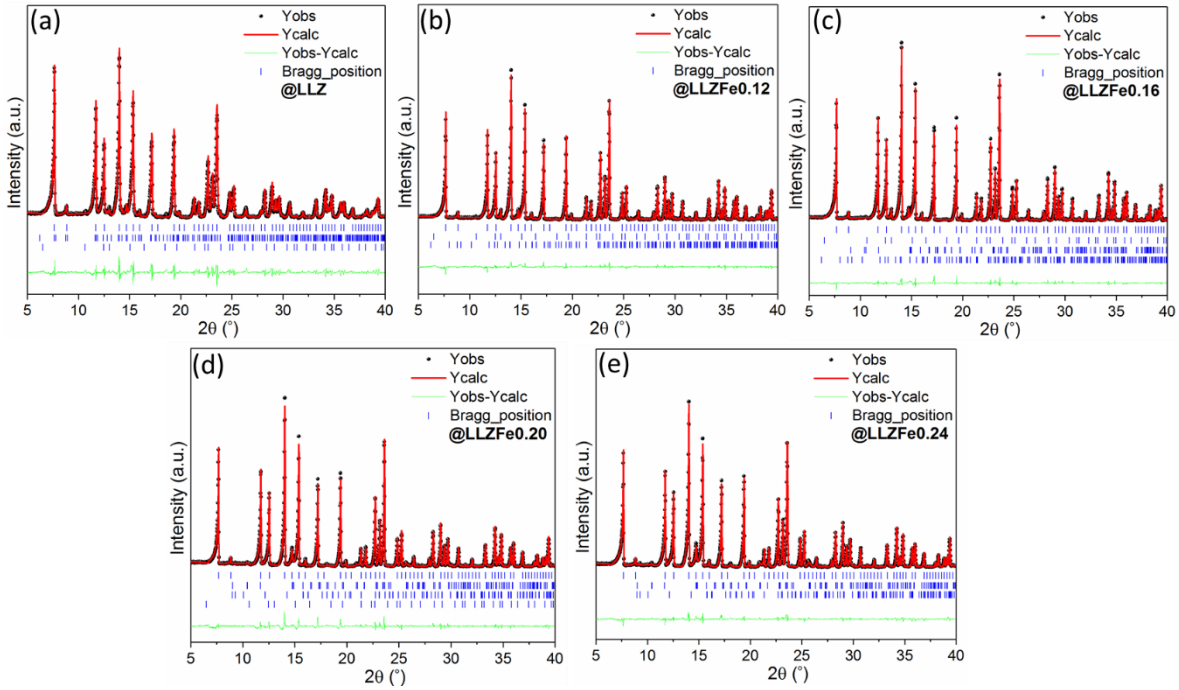

Figure S6.3. Rietveld refinement of the raw LLZ and LLZFe samples, black dot marks show observed X-ray diffraction intensities and a red solid line represents calculated intensities, blue vertical marks indicate positions of allowed Bragg reflections, the green curve at the bottom is a difference between the observed and calculated intensities in the same scale: a-LLZ, b-LLZFe0.12, c-LLZFe0.16, d-LLZFe0.20, and e-LLZFe0.12.

Table S1 Crystal parameter of raw LLZ and LLZFe samples, and the phase content determined by Rietveld refinement.

sample	lattice parameter (α Å)	cubic phase (%) (*Ia$\bar{3}$d*)	tetragonal phase (%) (*I4$_1$/acd*)	$La_2Zr_2O_7$ (%) (*Fd$\bar{3}$m*)	$FeLaO_3$ (%) (*Pnma*)	Li_2ZrO_3 (%) (*C12/c1*)	χ^2
LLZ	12.9976(2)	92.69(0.82)	5.71(0.38)	1.60(0.14)	-	-	7.68
LLZFe0.12	12.9690(1)	92.63(0.45)	5.30(0.14)	2.06(0.08)	-	-	2.56
LLZFe0.16	12.9694(1)	96.33(0.38)	0.57(0.08)	2.33(0.08)	0.77(0.00)	-	9.55
LLZFe0.20	12.9713(1)	95.45(0.61)		0.18(0.05)	3.62(0.02)	0.75(0.27)	4.44
LLZFe0.24	12.9733(1)	92.81(0.45)	-	-	5.27(0.13)	1.92(0.19)	3.86

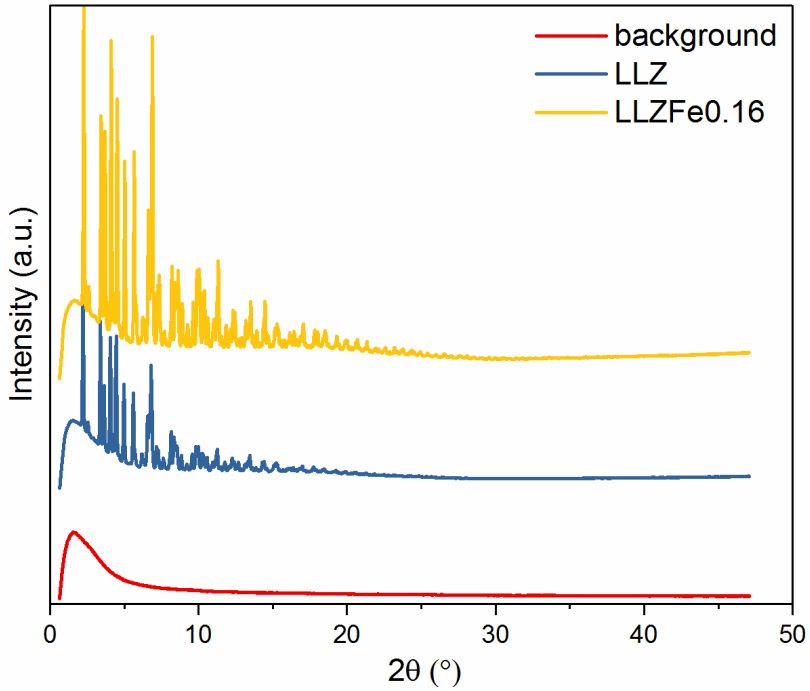

Figure S6.4 ex-situ X-ray total scattering of the raw LLZ and LLZFe0.16 powders.

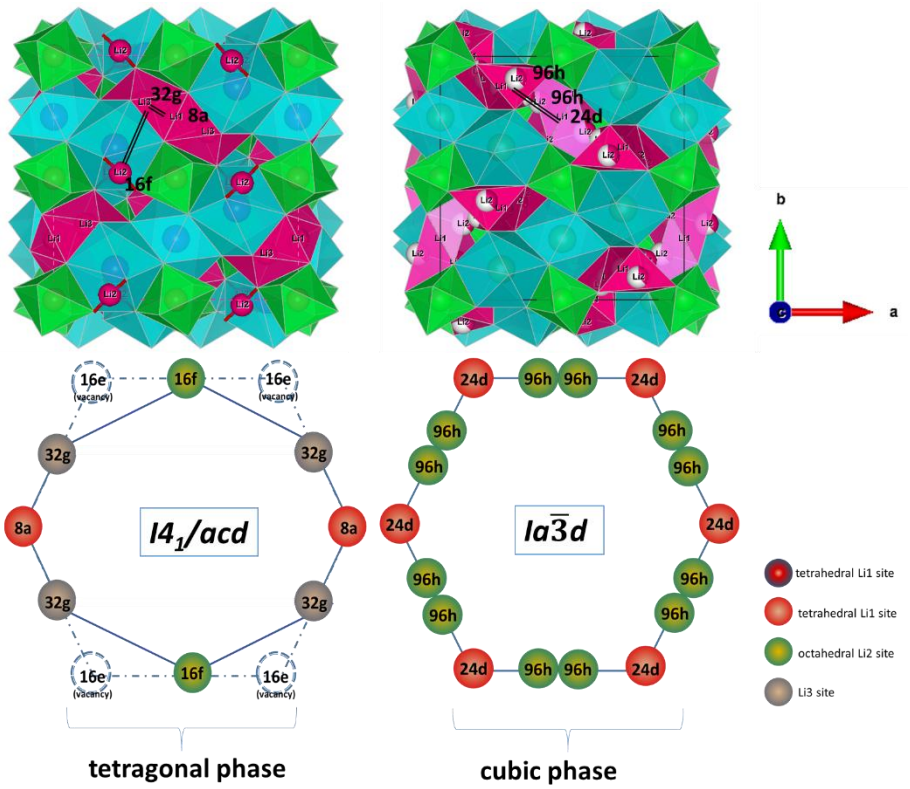

Figure S6.5 Li sites and loop arrangement in the LLZ crystals: tetragonal- and cubic phase.

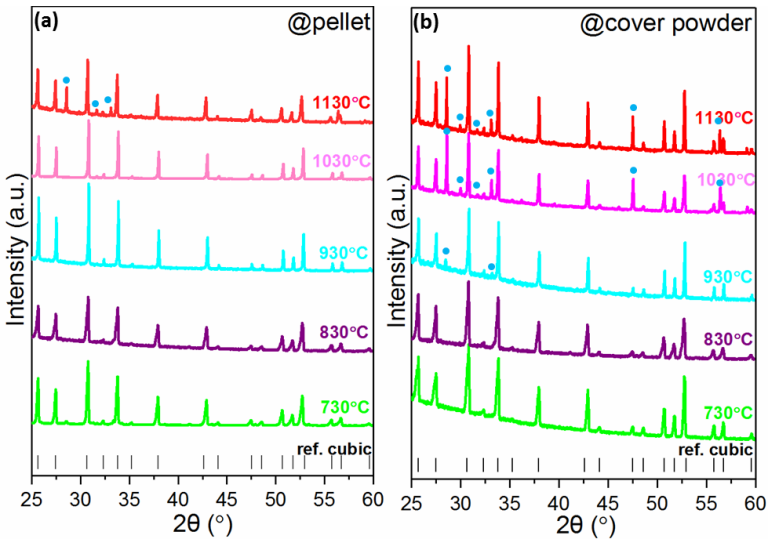

Figure S6.6. XRD patterns (Cu $K_{\alpha 1}$) of the ground powder from the LLZFe0.16 pellet (a) and corresponding cover powder (b) at varying temperatures.

Table S6.2 Fitting result of the resistance of the LLZ and LLZFe0.16 pellets measured at varying temperature.

Sintering temperature	25 ℃		35 ℃		45 ℃		55 ℃		65 ℃	
Sample	LLZ	LLZFe0.16	LLZ	LLZFe0.16	LLZ	LLZFe0.16	LLZ	LLZFe0.16	LLZ	LLZFe0.16
Bulk resistance ($\Omega \cdot cm^2$)	1483	1198	1659	1198	1552	1017	1495	794	976	498
Interface resistance ($\Omega \cdot cm^2$)	17850	3832	14970	3715	12960	3427	11350	3019	10390	3026
Total resistance ($\Omega \cdot cm^2$)	19333	5030	16629	4913	14512	4444	12845	3813	11366	3524
χ^2	1.69E-2	8.89E-3	1.08E-2	6.85E-3	8.91E-3	1.01E-3	7.99E-3	2.05E-3	7.55E-3	6.90E-3
Ion conductivity (Scm^{-1})	4.58E-6	1.76E-5	5.32E-6	1.80E-5	6.10E-6	1.99E-5	6.89E-6	2.32E-5	7.79E-6	2.51E-5

References

[1] A. Yoshino, The Birth of the Lithium-Ion Battery, Angew. Chemie Int. Ed. 51 (2012) 5798–5800. doi:10.1002/anie.201105006.

[2] M. Armand, J.-M. Tarascon, Building better batteries, Nature. 451 (2008) 652–657. doi:10.1038/451652a.

[3] M.A. Hannan, M.S.H. Lipu, A. Hussain, A. Mohamed, A review of lithium-ion battery state of charge estimation and management system in electric vehicle applications : Challenges and recommendations, Renew. Sustain. Energy Rev. 78 (2017) 834–854. doi:10.1016/j.rser.2017.05.001.

[4] Y. Wang, J. Yi, Y. Xia, Recent progress in aqueous lithium-ion batteries, Adv. Energy Mater. 2 (2012) 830–840. doi:10.1002/aenm.201200065.

[5] W. Li, R. Long, H. Chen, J. Geng, A review of factors influencing consumer intentions to adopt battery electric vehicles, Renew. Sustain. Energy Rev. 78 (2017) 318–328. doi:10.1016/j.rser.2017.04.076.

[6] N. Barbieri, Investigating the impacts of technological position and European environmental regulation on green automotive patent activity, Ecol. Econ. 117 (2015) 140–152. doi:10.1016/j.ecolecon.2015.06.017.

[7] J. Lee, F.M. Veloso, D.A. Hounshell, E.S. Rubin, Forcing technological change: A case of automobile emissions control technology development in the US, Technovation. 30 (2010) 249–264. doi:10.1016/j.technovation.2009.12.003.

[8] H.E. Friedrich, V. Concepts, Vehicle concepts for tomorrow' s demand : a European research perspective, 2016 Int. Conf. Adv. Automot. Technol. (2016) http://elib.dlr.de/106636/1/ICAT%20Keynote%20SCHMI.

[9] G. Berckmans, M. Messagie, J. Smekens, N. Omar, L. Vanhaverbeke, J. Van Mierlo, Cost Projection of State of the Art Lithium-Ion Batteries for Electric Vehicles Up to 2030, Energies. 10 (2017) 1314. doi:10.3390/en10091314.

[10] N. Lutsey, The rise of electric vehicles: The second million, Int. Counc. Clean Transp. (2017).

[11] D. Larcher, J.-M. Tarascon, Towards greener and more sustainable batteries for electrical energy storage, Nat. Chem. 7 (2015) 19–29. doi:10.1038/nchem.2085.

[12] V. Das, S. Padmanaban, K. Venkitusamy, R. Selvamuthukumaran, F. Blaabjerg, P. Siano, Recent advances and challenges of fuel cell based power system architectures and control – A review, Renew. Sustain. Energy Rev. 73 (2017) 10–18. doi:10.1016/j.rser.2017.01.148.

[13] Q. Xu, F. Zhang, L. Xu, P. Leung, C. Yang, H. Li, The applications and prospect of fuel cells in medical field: A review, Renew. Sustain. Energy Rev. 67 (2017) 574–580. doi:10.1016/j.rser.2016.09.042.

[14] W.R.W. Daud, R.E. Rosli, E.H. Majlan, S.A.A. Hamid, R. Mohamed, T. Husaini, PEM fuel cell system control: A review, Renew. Energy. 113 (2017) 620–638. doi:10.1016/j.renene.2017.06.027.

[15] D. Bresser, K. Hosoi, D. Howell, H. Li, H. Zeisel, K. Amine, S. Passerini, Perspectives of automotive battery R&D in China, Germany, Japan, and the USA, J. Power Sources. 382 (2018) 176–178. doi:10.1016/j.jpowsour.2018.02.039.

[16] J.M. Tarascon, J.M. Tarascon, M. Armand, M. Armand, Issues and challenges facing rechargeable lithium batteries, Nature. 414 (2001) 359–367. doi:10.1038/35104644.

[17] K. Xu, Electrolytes and Interphases in Li-Ion Batteries and Beyond, Chem. Rev. 114 (2014) 11503–11618. doi:10.1021/cr500003w.

[18] S. Xin, Y. You, S. Wang, H. Gao, Y. Yin, Y. Guo, Solid-State Lithium Metal Batteries Promoted by Nanotechnology: Progress and Prospects, (2017). doi:10.1021/acsenergylett.7b00175.

[19] K.M. Diederichsen, H.G. Buss, B.D. McCloskey, The Compensation Effect in the Vogel–Tammann–Fulcher (VTF) Equation for Polymer-Based Electrolytes, Macromolecules. 50 (2017) 3831–3840. doi:10.1021/acs.macromol.7b00423.

[20] A. Vallée, S. Besner, J. Prud'Homme, Comparative study of poly(ethylene oxide) electrolytes made with $LiN(CF_3SO_2)_2$, $LiCF_3SO_3$ and $LiClO_4$: Thermal properties and conductivity behaviour, Electrochim. Acta. 37 (1992) 1579–1583. doi:10.1016/0013-4686(92)80115-3.

[21] N. Kamaya, K. Homma, Y. Yamakawa, M. Hirayama, R. Kanno, M. Yonemura, T. Kamiyama, Y. Kato, S. Hama, K. Kawamoto, A. Mitsui, A lithium superionic conductor., Nat. Mater. 10 (2011) 682–6. doi:10.1038/nmat3066.

[22] M.D. Bhatt, C. O'Dwyer, Recent progress in theoretical and computational investigations of Li-ion battery materials and electrolytes, Phys. Chem. Chem. Phys. 17 (2015) 4799–4844. doi:10.1039/C4CP05552G.

[23] Y. Seino, T. Ota, K. Takada, A. Hayashi, M. Tatsumisago, A sulphide lithium super ion conductor is superior to liquid ion conductors for use in rechargeable batteries, Energy Environ. Sci. 7 (2014) 627–631. doi:10.1039/c3ee41655k.

[24] Z. Ma, H.-G. Xue, S.-P. Guo, Recent achievements on sulfide-type solid electrolytes: crystal structures and electrochemical performance, J. Mater. Sci. 53 (2018) 3927–3938. doi:10.1007/s10853-017-1827-6.

[25] A. Manthiram, X. Yu, S. Wang, Lithium battery chemistries enabled by solid-state electrolytes, Nat. Rev. Mater. 2 (2017) 16103. doi:10.1038/natrevmats.2016.103.

[26] M. Faraday, IV. Experimental researches in electricity.—Third series, Philos. Trans. R. Soc. London. 123 (1833) 23–54. doi:10.1098/rstl.1833.0006.

[27] S. Chandra, H.B. Lal, K. Shahi, An electrochemical cell with solid, super-ionic Ag_4KI_5 as the electrolyte, J. Phys. D. Appl. Phys. 7 (1974) 327. doi:10.1088/0022-3727/7/1/327.

[28] P.M. and V.C. Huyghebaert, Conformal Deposition for 3D Thin-Film Batteries, ECS Trans. 58 (2013) 111–118. doi:10.1149/05810.0111ecst.

[29] J.M.P. and P.V.W. Fenton, D. E., Complexes of alkali metal ions with poly (ethylene oxide), Polymer (Guildf). 14 (1973) 589.

[30] H. Yamada, T. Ito, R. Hongahally Basappa, Sintering Mechanisms of High-Performance Garnet-type Solid Electrolyte Densified by Spark Plasma Sintering, Electrochim. Acta. 222 (2016) 648–656. doi:10.1016/j.electacta.2016.11.020.

[31] M. Nagao, A. Hayashi, M. Tatsumisago, T. Kanetsuku, T. Tsuda, S. Kuwabata, In situ SEM study of a lithium deposition and dissolution mechanism in a bulk-type solid-state cell with a Li_2S–P_2S_5 solid electrolyte, Phys. Chem. Chem. Phys. 15 (2013) 18600. doi:10.1039/c3cp51059j.

[32] J.B. Bates, N.J. Dudney, B. Neudecker, A. Ueda, C.D. Evans, Thin-film lithium and lithium-ion batteries, Solid State Ionics. 135 (2000) 33–45. doi:10.1016/S0167-2738(00)00327-1.

[33] R.C. Agrawal, G.P. Pandey, Solid polymer electrolytes: materials designing and all-solid-state battery applications: an overview, J. Phys. D. Appl. Phys. 41 (2008) 223001. doi:10.1088/0022-3727/41/22/223001.

[34] R. Kanno, M. Murayama, Lithium Ionic Conductor Thio-LISICON: The Li_2S-GeS_2-P_2S_5 System, J. Electrochem. Soc. 148 (2001) A742. doi:10.1149/1.1379028.

[35] J.B. Bates, N.J. Dudney, D.C. Lubben, G.R. Gruzalski, B.S. Kwak, X. Yu, R. a. Zuhr, Thin-film rechargeable lithium batteries, J. Power Sources. 54 (1995) 58–62. doi:10.1016/0378-7753(94)02040-A.

[36] A. Sakuda, A. Hayashi, M. Tatsumisago, Sulfide solid electrolyte with favorable mechanical property for all-solid-state lithium battery., Sci. Rep. 3 (2013) 2261. doi:10.1038/srep02261.

[37] A. Levasseur, J.-C. Brethous, M. Kbala, P. Hagenmuller, Synthesis and characterization of new amorphous solid electrolytes, Solid State Ionics. 5 (1981) 651–654. doi:10.1016/0167-2738(81)90338-6.

[38] Z.Z. and J.H. KENNEDY, Synthesis and characterization of the B_2S_3-Li_2S, the P_2S_5-Li_2S and the B_2S_3-P_2S_5-Li_2S glass systems, Solid State Ionics. 38 (1990) 217–224. doi:https://doi.org/10.1016/0167-2738(90)90424-P.

[39] S. Shiotani, K. Ohara, H. Tsukasaki, S. Mori, R. Kanno, Pair distribution function analysis of sulfide glassy electrolytes for all-solid-state batteries: Understanding the improvement of ionic conductivity under annealing condition, Sci. Rep. 7 (2017) 6972. doi:10.1038/s41598-017-07086-y.

[40] F. Mizuno, A. Hayashi, K. Tadanaga, M. Tatsumisago, New, Highly Ion-Conductive Crystals Precipitated from Li_2S-P_2S_5 Glasses, Adv. Mater. 17 (2005) 918–921. doi:10.1002/adma.200401286.

[41] K. Hayamizu, Y. Aihara, Lithium ion diffusion in solid electrolyte $(Li_2S)_7(P2S_5)_3$ measured by pulsed-gradient spin-echo ^{7}Li NMR spectroscopy, Solid State Ionics. 238 (2013) 7–14. doi:10.1016/j.ssi.2013.02.014.

[42] P. Knauth, Inorganic solid Li ion conductors: An overview, Solid State Ionics. 180 (2009) 911–916. doi:10.1016/j.ssi.2009.03.022.

[43] Y. Mo, S.P. Ong, G. Ceder, First Principles Study of the $Li_{10}GeP_2S_{12}$ Lithium Super Ionic Conductor Material, Chem. Mater. 24 (2012) 15–17. doi:10.1021/cm203303y.

[44] Y. Wang, W.D. Richards, S.P. Ong, L.J. Miara, J.C. Kim, Y. Mo, G. Ceder, Design principles for solid-state lithium superionic conductors, Nat. Mater. 14 (2015) 1026–1031. doi:10.1038/nmat4369.

[45] G. Sahu, Z. Lin, J. Li, Z. Liu, N. Dudney, C. Liang, Air-stable, high-conduction solid electrolytes of arsenic-substituted Li_4SnS_4, Energy Environ. Sci. 7 (2014) 1053–1058. doi:10.1039/C3EE43357A.

[46] S. Boulineau, J.-M. Tarascon, J.-B. Leriche, V. Viallet, Electrochemical properties of all-solid-state lithium secondary batteries using Li-argyrodite Li_6PS_5Cl as solid electrolyte, Solid State Ionics. 242 (2013) 45–48. doi:10.1016/j.ssi.2013.04.012.

[47] C. Yu, L. van Eijck, S. Ganapathy, M. Wagemaker, Synthesis, structure and electrochemical performance of the argyrodite Li_6PS_5Cl solid electrolyte for Li-ion solid state batteries, Electrochim. Acta. 215 (2016) 93–99. doi:10.1016/j.electacta.2016.08.081.

[48] T. Ohtomo, A. Hayashi, M. Tatsumisago, K. Kawamoto, Suppression of H_2S gas generation from the $75Li_2S{\cdot}25P_2S_5$ glass electrolyte by additives, J. Mater. Sci. 48 (2013) 4137–4142. doi:10.1007/s10853-013-7226-8.

[49] Y.S. Jung, D.Y. Oh, Y.J. Nam, K.H. Park, Issues and challenges for bulk-type all-solid-state rechargeable lithium batteries using sulfide solid electrolytes, Isr. J. Chem. 55 (2015) 472–485. doi:10.1002/ijch.201400112.

[50] B.R. Shin, Y.J. Nam, D.Y. Oh, D.H. Kim, J.W. Kim, Y.S. Jung, Comparative Study of TiS2/Li-In All-Solid-State Lithium Batteries Using Glass-Ceramic Li_3PS_4 and $Li_{10}GeP_2S_{12}$ Solid Electrolytes, Electrochim. Acta. 146 (2014) 395–402. doi:10.1016/j.electacta.2014.08.139.

[51] G. Oh, M. Hirayama, O. Kwon, K. Suzuki, R. Kanno, Bulk-Type All Solid-State Batteries with 5 V Class $LiNi_{0.5}Mn_{1.5}O_4$ Cathode and $Li_{10}GeP_2S_{12}$ Solid Electrolyte, Chem. Mater. 28 (2016) 2634–2640. doi:10.1021/acs.chemmater.5b04940.

[52] S. Wenzel, D.A. Weber, T. Leichtweiss, M.R. Busche, J. Sann, J. Janek, Interphase formation and degradation of charge transfer kinetics between a lithium metal anode and highly crystalline $Li_7P_3S_{11}$ solid electrolyte, Solid State Ionics. 286 (2016) 24–33. doi:10.1016/j.ssi.2015.11.034.

[53] J. Kasemchainan, P.G. Bruce, All-Solid-State Batteries and their Remaining Challenges, Johnson Matthey Technol. Rev. 62 (2018) 177–180. doi:10.1595/205651318X696747.

[54] Y. Deng, C. Eames, J.-N. Chotard, F. Lalère, V. Seznec, S. Emge, O. Pecher, C.P. Grey, C. Masquelier, M.S. Islam, Structural and Mechanistic Insights into Fast Lithium-Ion Conduction in Li_4SiO_4–Li_3PO_4 Solid Electrolytes, J. Am. Chem. Soc. 137 (2015) 9136–9145. doi:10.1021/jacs.5b04444.

[55] J.S. Thokchom, B. Kumar, The effects of crystallization parameters on the ionic conductivity of a lithium aluminum germanium phosphate glass–ceramic, J. Power Sources. 195 (2010) 2870–2876. doi:10.1016/j.jpowsour.2009.11.037.

[56] M. Yashima, M. Itoh, Y. Inaguma, Y. Morii, Crystal Structure and Diffusion Path in the Fast Lithium-Ion Conductor $La_{0.62}Li_{0.16}TiO_3$, J. Am. Chem. Soc. 127 (2005) 3491–3495. doi:10.1021/ja0449224.

[57] W.G. Wang, X.P. Wang, Y.X. Gao, G.L. Hao, W.Q. Ma, Q.F. Fang, Internal friction study on the lithium ion diffusion of $Li_5La_3M_2O_{12}$ (M = Ta, Nb) ionic conductors, Solid State Sci. 13 (2011) 1760–1764. doi:10.1016/j.solidstatesciences.2011.07.004.

[58] H. Hong, Crystal Structure and Ionic Conductivity of $Li_{14}Zn(GeO4)_4$ and other new Li^+ superionic conductors, Mater. Res. Bull. 13 (1978) 117–124. doi:10.5012/bkcs.2012.33.6.2083.

[59] Y.-W. Hu, Ionic Conductivity of Lithium Orthosilicate-Lithium Phosphate Solid Solutions, J. Electrochem. Soc. 124 (1977) 1240. doi:10.1149/1.2133537.

[60] H. Kim, Y. Ding, P.A. Kohl, LiSICON – ionic liquid electrolyte for lithium ion battery, J. Power Sources. 198 (2012) 281–286. doi:10.1016/j.jpowsour.2011.10.005.

[61] R. Chen, W. Qu, X. Guo, L. Li, F. Wu, The pursuit of solid-state electrolytes for lithium batteries: from comprehensive insight to emerging horizons, Mater. Horiz. (2016). doi:10.1039/C6MH00218H.

[62] J.B. Goodenough, H..-P. Hong, J.A. Kafalas, Fast Na^+-ion transport in skeleton structures, Mater. Res. Bull. 11 (1976) 203–220. doi:10.1016/0025-5408(76)90077-5.

[63] B. Kumar, D. Thomas, J. Kumar, Space-Charge-Mediated Superionic Transport in Lithium Ion Conducting Glass–Ceramics, J. Electrochem. Soc. 156 (2009) A506. doi:10.1149/1.3122903.

[64] V. Thangadurai, W. Weppner, Recent progress in solid oxide and lithium ion conducting electrolytes research, Ionics (Kiel). 12 (2006) 81–92. doi:10.1007/s11581-006-0013-7.

[65] X. Xu, Z. Wen, X. Yang, J. Zhang, Z. Gu, High lithium ion conductivity glass-ceramics in Li_2O-Al_2O_3-TiO_2-P_2O_5 from nanoscaled glassy powders by mechanical milling, Solid State Ionics. 177 (2006) 2611–2615. doi:10.1016/j.ssi.2006.04.010.

[66] B. Kumar, J.S. Thokchom, Space charge signature and its effects on ionic transport in heterogeneous solids, J. Am. Ceram. Soc. 90 (2007) 3323–3325. doi:10.1111/j.1551-2916.2007.01877.x.

[67] J.K. Feng, L. Lu, M.O. Lai, Lithium storage capability of lithium ion conductor $Li_{1.5}Al_{0.5}Ge_{1.5}(PO_4)_3$, J. Alloys Compd. 501 (2010) 255–258. doi:10.1016/j.jallcom.2010.04.084.

[68] Y. Liang, L. Ji, B. Guo, Z. Lin, Y. Yao, Y. Li, M. Alcoutlabi, Y. Qiu, X. Zhang, Preparation and electrochemical characterization of ionic-conducting lithium lanthanum titanate oxide/polyacrylonitrile submicron composite fiber-based lithium-ion battery separators, J. Power Sources. 196 (2011) 436–441. doi:10.1016/j.jpowsour.2010.06.088.

[69] Y. Inaguma, C. Liquan, M. Itoh, T. Nakamura, T. Uchida, H. Ikuta, M. Wakihara, High ionic conductivity in lithium lanthanum titanate, Solid State Commun. 86 (1993) 689–693. doi:10.1016/0038-1098(93)90841-A.

[70] R. Murugan, V. Thangadurai, W. Weppner, Fast Lithium Ion Conduction in Garnet-Type $Li_7La_3Zr_2O_{12}$, Angew. Chemie Int. Ed. 46 (2007) 7778–7781. doi:10.1002/anie.200701144.

[71] M. Xu, M.S. Park, J.M. Lee, T.Y. Kim, Y.S. Park, E. Ma, Mechanisms of Li^+ transport in garnet-type cubic Li_3La, Phys. Rev. B. 85 (2012) 052301. doi:10.1103/PhysRevB.85.052301.

[72] R. Murugan, W. Weppner, P. Schmid-Beurmann, V. Thangadurai, Structure and lithium ion conductivity of garnet-like $Li_5La_3Sb_2O_{12}$ and $Li_6SrLa_2Sb_2O_{12}$, Mater. Res. Bull. 43 (2008) 2579–2591. doi:10.1016/j.materresbull.2007.10.035.

[73] V. Thangadurai, W. Weppner, $Li_6ALa_2Ta_2O_{12}$ (A = Sr, Ba): Novel Garnet-Like Oxides for Fast Lithium Ion Conduction, Adv. Funct. Mater. 15 (2005) 107–112. doi:10.1002/adfm.200400044.

[74] T. Thompson, A. Sharafi, M.D. Johannes, A. Huq, J.L. Allen, J. Wolfenstine, J. Sakamoto, A Tale of Two Sites: On Defining the Carrier Concentration in Garnet-Based Ionic Conductors for Advanced Li Batteries, Adv. Energy Mater. 5 (2015) 1500096. doi:10.1002/aenm.201500096.

[75] S.-W. Baek, J.-M. Lee, T.Y. Kim, M.-S. Song, Y. Park, Garnet related lithium ion conductor processed by spark plasma sintering for all solid state batteries, J. Power Sources. 249 (2014) 197–206. doi:10.1016/j.jpowsour.2013.10.089.

[76] H. Xie, J.A. Alonso, Y. Li, M.T. Fernández-Díaz, J.B. Goodenough, Lithium Distribution in Aluminum-Free Cubic $Li_7La_3Zr_2O_{12}$, Chem. Mater. 23 (2011) 3587–3589. doi:10.1021/cm201671k.

[77] J. Wolfenstine, E. Rangasamy, J.L. Allen, J. Sakamoto, High conductivity of dense tetragonal $Li_7La_3Zr_2O_{12}$, J. Power Sources. 208 (2012) 193–196. doi:10.1016/j.jpowsour.2012.02.031.

[78] H. Buschmann, J. Dölle, S. Berendts, A. Kuhn, P. Bottke, M. Wilkening, P. Heitjans, A. Senyshyn, H. Ehrenberg, A. Lotnyk, V. Duppel, L. Kienle, J. Janek, Structure and dynamics of the fast lithium ion conductor "$Li_7La_3Zr_2O_{12}$," Phys. Chem. Chem. Phys. 13 (2011) 19378. doi:10.1039/c1cp22108f.

[79] R. Wagner, G.J. Redhammer, D. Rettenwander, A. Senyshyn, W. Schmidt, M. Wilkening, G. Amthauer, Crystal Structure of Garnet-Related Li-Ion Conductor $Li_{7-3x}Ga_xLa_3Zr_2O_{12}$: Fast Li-Ion Conduction Caused by a Different Cubic Modification?, Chem. Mater. 28 (2016) 1861–1871. doi:10.1021/acs.chemmater.6b00038.

[80] M. Rawlence, I. Garbayo, S. Buecheler, J.L.M. Rupp, On the chemical stability of post-lithiated garnet Al-stabilized $Li_7La_3Zr_2O_{12}$ solid state electrolyte thin films, Nanoscale. (2016) 14746–

14753. doi:10.1039/C6NR04162K.

[81] J. Awaka, N. Kijima, H. Hayakawa, J. Akimoto, Synthesis and structure analysis of tetragonal $Li_7La_3Zr_2O_{12}$ with the garnet-related type structure, J. Solid State Chem. 182 (2009) 2046–2052. doi:10.1016/j.jssc.2009.05.020.

[82] K. Meier, T. Laino, A. Curioni, Solid-State Electrolytes: Revealing the Mechanisms of Li-Ion Conduction in Tetragonal and Cubic LLZO by First-Principles Calculations, J. Phys. Chem. C. 118 (2014) 6668–6679. doi:10.1021/jp5002463.

[83] A. Kuhn, J.-Y. Choi, L. Robben, F. Tietz, M. Wilkening, P. Heitjans, Li Ion Dynamics in Al-Doped Garnet-Type $Li_7La_3Zr_2O_{12}$ Crystallizing with Cubic Symmetry, Zeitschrift Für Phys. Chemie. 226 (2012) 525–537. doi:10.1524/zpch.2012.0250.

[84] S. Stramare, V. Thangadurai, W. Weppner, Lithium Lanthanum Titanates: A Review, Chem. Mater. 15 (2003) 3974–3990. doi:10.1021/cm0300516.

[85] W.H. Meyer, Polymer Electrolytes for Lithium-Ion Batteries, Adv. Mater. 10 (1998) 439–448. doi:10.1002/(SICI)1521-4095(199804)10:6<439::AID-ADMA439>3.0.CO;2-I.

[86] Z. Gadjourova, Y.G. Andreev, D.P. Tunstall, P.G. Bruce, Ionic conductivity in crystalline polymer electrolytes., Nature. 412 (2001) 520–523. doi:10.1038/35087538.

[87] S.K. Chaurasia, R.K. Singh, S. Chandra, Ion–polymer complexation and ion-pair formation in a polymer electrolyte PEO:$LiPF_6$ containing an ionic liquid having same anion: A Raman study, Vib. Spectrosc. 68 (2013) 190–195. doi:10.1016/j.vibspec.2013.08.001.

[88] I. Osada, H. De Vries, B. Scrosati, S. Passerini, Ionic-Liquid-Based Polymer Electrolytes for Battery Applications, Angew. Chemie-Int. Ed. 55 (2016) 500–513. doi:10.1002/anie.201504971.

[89] P. V. Wright, Electrical conductivity in ionic complexes of poly(ethylene oxide), Br. Polym. J. 7 (1975) 319–327. doi:10.1002/pi.4980070505.

[90] F.B. Dias, L. Plomp, J.B.J. Veldhuis, Trends in polymer electrolytes for secondary lithium batteries, J. Power Sources. 88 (2000) 169–191. doi:10.1016/S0378-7753(99)00529-7.

[91] C. Zhang, K. Ueno, A. Yamazaki, K. Yoshida, H. Moon, T. Mandai, Y. Umebayashi, K. Dokko, M. Watanabe, Chelate Effects in Glyme/Lithium Bis(trifluoromethanesulfonyl)amide Solvate Ionic Liquids. I. Stability of Solvate Cations and Correlation with Electrolyte Properties, J. Phys. Chem. B. 118 (2014) 5144–5153. doi:10.1021/jp501319e.

[92] J. Mindemark, M.J. Lacey, T. Bowden, D. Brandell, Beyond PEO-Alternative host materials for Li^+ conducting solid polymer electrolytes, Prog. Polym. Sci. 81 (2018) 114–143. doi:10.1016/j.progpolymsci.2017.12.004.

[93] W. He, Z. Cui, X. Liu, Y. Cui, J. Chai, X. Zhou, Z. Liu, G. Cui, Carbonate-linked poly(ethylene oxide) polymer electrolytes towards high performance solid state lithium batteries, Electrochim. Acta. 225 (2017) 151–159. doi:10.1016/j.electacta.2016.12.113.

[94] Y. Wang, F. Fan, A.L. Agapov, T. Saito, J. Yang, X. Yu, K. Hong, J. Mays, A.P. Sokolov, Examination of the fundamental relation between ionic transport and segmental relaxation in polymer electrolytes, Polymer (Guildf). 55 (2014) 4067–4076. doi:10.1016/j.polymer.2014.06.085.

[95] J.-H. Choi, C.-H. Lee, J.-H. Yu, C.-H. Doh, S.-M. Lee, Enhancement of ionic conductivity of composite membranes for all-solid-state lithium rechargeable batteries incorporating tetragonal $Li_7La_3Zr_2O_{12}$ into a polyethylene oxide matrix, J. Power Sources. 274 (2015) 458–463. doi:10.1016/j.jpowsour.2014.10.078.

[96] C.-H. Lee, G. Park, J. Choi, C. Doh, D. Bae, J. Kim, S. Lee, Low temperature synthesis of garnet type solid electrolyte by modified polymer complex process and its characterization, Mater. Res. Bull. 83 (2016) 309–315. doi:10.1016/j.materresbull.2016.02.040.

[97] T. Yang, Y. Li, C.K. Chan, Enhanced lithium ion conductivity in lithium lanthanum titanate solid electrolyte nanowires prepared by electrospinning, J. Power Sources. 287 (2015) 164–169. doi:10.1016/j.jpowsour.2015.04.044.

[98] N.M. Asl, J. Keith, C. Lim, L. Zhu, Y. Kim, Inorganic solid/organic liquid hybrid electrolyte for use in Li-ion battery, Electrochim. Acta. 79 (2012) 8–16. doi:10.1016/j.electacta.2012.06.038.

[99] Y. Liu, J.Y. Lee, L. Hong, In situ preparation of poly(ethylene oxide)–SiO_2 composite polymer electrolytes, J. Power Sources. 129 (2004) 303–311. doi:10.1016/j.jpowsour.2003.11.026.

[100] J. Cao, L. Wang, X. He, M. Fang, J. Gao, J. Li, L. Deng, H. Chen, G. Tian, J. Wang, S. Fan, In situ prepared nano-crystalline TiO_2–poly(methyl methacrylate) hybrid enhanced composite polymer electrolyte for Li-ion batteries, J. Mater. Chem. A. 1 (2013) 5955. doi:10.1039/c3ta00086a.

[101] H.M.J.C. Pitawala, M.A.K.L. Dissanayake, V.A. Seneviratne, Combined effect of Al_2O_3 nano-fillers and EC plasticizer on ionic conductivity enhancement in the solid polymer electrolyte $(PEO)_9LiTf$, Solid State Ionics. 178 (2007) 885–888. doi:10.1016/j.ssi.2007.04.008.

[102] F. Langer, M.S. Palagonia, I. Bardenhagen, J. Glenneberg, F. La Mantia, R. Kun, Impedance Spectroscopy Analysis of the Lithium Ion Transport through the $Li_7La_3Zr_2O_{12}$/$P(EO)_{20}Li$ Interface, J. Electrochem. Soc. 164 (2017) A2298–A2303. doi:10.1149/2.0381712jes.

[103] X. Zhang, T. Liu, S. Zhang, X. Huang, B. Xu, Y. Lin, B. Xu, L. Li, C.-W. Nan, Y. Shen, Synergistic Coupling between $Li_{6.75}La_3Zr_{1.75}Ta_{0.25}O_{12}$ and Poly(vinylidene fluoride) Induces High Ionic Conductivity, Mechanical Strength, and Thermal Stability of Solid Composite Electrolytes, J. Am. Chem. Soc. 139 (2017) 13779–13785. doi:10.1021/jacs.7b06364.

[104] H. Zhai, P. Xu, M. Ning, Q. Cheng, J. Mandal, Y. Yang, A Flexible Solid Composite Electrolyte with Vertically Aligned and Connected Ion-Conducting Nanoparticles for Lithium Batteries, Nano Lett. 17 (2017) 3182–3187. doi:10.1021/acs.nanolett.7b00715.

[105] E. Quartarone, P. Mustarelli, Electrolytes for solid-state lithium rechargeable batteries: recent advances and perspectives, Chem. Soc. Rev. 40 (2011) 2525–2540. doi:10.1039/c0cs00081g.

[106] J. Zheng, M. Tang, Y.-Y. Hu, Lithium Ion Pathway within $Li_7La_3Zr_2O_{12}$-Polyethylene Oxide Composite Electrolytes, Angew. Chemie Int. Ed. 55 (2016) 12538–12542. doi:10.1002/anie.201607539.

[107] P. Knauth, Ionic conductor composites: theory and materials, J. Electroceramics. 5 (2000) 111–125. doi:10.1023/A:1009906101421.

[108] M.J. Saxton, Two-Dimensional Continuum Percolation Threshold for Diffusing Particles of Nonzero Radius, Biophys. J. 99 (2010) 1490–1499. doi:10.1016/j.bpj.2010.06.033.

[109] X. Yang, J. Hu, S. Chen, J. He, Understanding the Percolation Characteristics of Nonlinear Composite Dielectrics, Sci. Rep. 6 (2016) 30597. doi:10.1038/srep30597.

[110] R. Kali, A. Mukhopadhyay, Spark plasma sintered/synthesized dense and nanostructured materials for solid-state Li-ion batteries: Overview and perspective, J. Power Sources. 247 (2014) 920–931. doi:10.1016/j.jpowsour.2013.09.010.

[111] J. Wei, H. Kim, D.-C. Lee, R. Hu, F. Wu, H. Zhao, F.M. Alamgir, G. Yushin, Influence of annealing on ionic transfer and storage stability of Li_2S–P_2S_5 solid electrolyte, J. Power Sources. 294 (2015) 494–500. doi:10.1016/j.jpowsour.2015.06.074.

[112] H. Morimoto, H. Awano, J. Terashima, Y. Shindo, S. Nakanishi, N. Ito, K. Ishikawa, S. Tobishima, Preparation of lithium ion conducting solid electrolyte of NASICON-type $Li_{1+x}Al_xTi_{2-x}(PO_4)_3$ (x = 0.3) obtained by using the mechanochemical method and its application as surface modification materials of $LiCoO_2$ cathode for lithium cell, J. Power Sources. 240 (2013) 636–643. doi:10.1016/j.jpowsour.2013.05.039.

[113] F. Blanc, M. Leskes, C.P. Grey, In Situ Solid-State NMR Spectroscopy of Electrochemical Cells: Batteries, Supercapacitors, and Fuel Cells, Acc. Chem. Res. 46 (2013) 1952–1963. doi:10.1021/ar400022u.

[114] X. Qiu, J.W. Thompson, S.J.L. Billinge, PDFgetX2 : a GUI-driven program to obtain the pair distribution function from X-ray powder diffraction data, J. Appl. Crystallogr. 37 (2004) 678–678. doi:10.1107/S0021889804011744.

[115] S.J.L. Billinge, Nanoscale structural order from the atomic pair distribution function (PDF): There's plenty of room in the middle, J. Solid State Chem. 181 (2008) 1695–1700. doi:10.1016/j.jssc.2008.06.046.

[116] C.L. Farrow, P. Juhas, J.W. Liu, D. Bryndin, E.S. Boin, J. Bloch, T. Proffen, S.J.L. Billinge, PDFfit2 and PDFgui: Computer programs for studying nanostructure in crystals, J. Phys. Condens. Matter. 19 (2007). doi:10.1088/0953-8984/19/33/335219.

[117] L.J. Miara, S.P. Ong, Y. Mo, W.D. Richards, Y. Park, J.-M. Lee, H.S. Lee, G. Ceder, Effect of Rb and Ta Doping on the Ionic Conductivity and Stability of the Garnet $Li_{7+2x-y}(La_{3-x}Rb_x)(Zr_{2-y}Ta_y)O_{12}$ ($0 \le x \le 0.375$, $0 \le y \le 1$) Superionic Conductor: A First Principles Investigation, Chem. Mater. 25 (2013) 3048–3055. doi:10.1021/cm401232r.

[118] J.B. Goodenough, Y. Kim, Challenges for rechargeable Li batteries, Chem. Mater. 22 (2010)

587–603. doi:10.1021/cm901452z.

[119] J. Zhang, N. Zhao, M. Zhang, Y. Li, P.K. Chu, X. Guo, Z. Di, X. Wang, H. Li, Flexible and ion-conducting membrane electrolytes for solid-state lithium batteries: Dispersion of garnet nanoparticles in insulating polyethylene oxide, Nano Energy. 28 (2016) 447–454. doi:10.1016/j.nanoen.2016.09.002.

[120] Z. Lin, X. Guo, H. Yu, Amorphous modified silyl-terminated 3D polymer electrolyte for high-performance lithium metal battery, Nano Energy. 41 (2017) 646–653. doi:10.1016/j.nanoen.2017.10.021.

[121] K. (Kelvin) Fu, Y. Gong, J. Dai, A. Gong, X. Han, Y. Yao, C. Wang, Y. Wang, Y. Chen, C. Yan, Y. Li, E.D. Wachsman, L. Hu, Flexible, solid-state, ion-conducting membrane with 3D garnet nanofiber networks for lithium batteries, Proc. Natl. Acad. Sci. 113 (2016) 7094–7099. doi:10.1073/pnas.1600422113.

[122] F. Han, Y. Zhu, X. He, Y. Mo, C. Wang, Electrochemical Stability of $Li_{10}GeP_2S_{12}$ and $Li_7La_3Zr_2O_{12}$ Solid Electrolytes, Adv. Energy Mater. 6 (2016) 1501590. doi:10.1002/aenm.201501590.

[123] D. Lin, Y. Liu, Y. Cui, Reviving the lithium metal anode for high-energy batteries, Nat. Nanotechnol. 12 (2017) 194–206. doi:10.1038/nnano.2017.16.

[124] Q. Liu, Z. Geng, C. Han, Y. Fu, S. Li, Y. He, F. Kang, B. Li, Challenges and perspectives of garnet solid electrolytes for all solid-state lithium batteries, J. Power Sources. 389 (2018) 120–134. doi:10.1016/j.jpowsour.2018.04.019.

[125] W. Xu, J. Wang, F. Ding, X. Chen, E. Nasybulin, Y. Zhang, J.-G. Zhang, Lithium metal anodes for rechargeable batteries, Energy Environ. Sci. 7 (2014) 513–537. doi:10.1039/C3EE40795K.

[126] R.P. Rao, W. Gu, N. Sharma, V.K. Peterson, M. Avdeev, S. Adams, In Situ Neutron Diffraction Monitoring of $Li_7La_3Zr_2O_{12}$ Formation: Toward a Rational Synthesis of Garnet Solid Electrolytes., Chem. Mater. 27 (2015) 2903–2910. doi:10.1021/acs.chemmater.5b00149.

[127] S. Lobe, C. Dellen, M. Finsterbusch, H.-G. Gehrke, D. Sebold, C.-L. Tsai, S. Uhlenbruck, O. Guillon, Radio frequency magnetron sputtering of $Li_7La_3Zr_2O_{12}$ thin films for solid-state batteries, J. Power Sources. 307 (2016) 684–689. doi:10.1016/j.jpowsour.2015.12.054.

[128] Y. Kim, A. Yoo, R. Schmidt, A. Sharafi, H. Lee, J. Wolfenstine, J. Sakamoto, Electrochemical Stability of $Li_{6.5}La_3Zr_{1.5}M_{0.5}O_{12}$ (M = Nb or Ta) against Metallic Lithium, Front. Energy Res. 4 (2016) 1–7. doi:10.3389/fenrg.2016.00020.

[129] F. Capuano, Composite Polymer Electrolytes, J. Electrochem. Soc. 138 (1991) 1918. doi:10.1149/1.2085900.

[130] S. Liu, N. Imanishi, T. Zhang, A. Hirano, Y. Takeda, O. Yamamoto, J. Yang, Lithium Dendrite Formation in Li/Poly(ethylene oxide)–Lithium Bis(trifluoromethanesulfonyl)imide and N-Methyl-N-propylpiperidinium Bis(trifluoromethanesulfonyl)imide/Li Cells, J. Electrochem. Soc. 157 (2010) A1092. doi:10.1149/1.3473790.

[131] M. Rosso, C. Brissot, A. Teyssot, M. Dollé, L. Sannier, J.-M. Tarascon, R. Bouchet, S. Lascaud, Dendrite short-circuit and fuse effect on Li/polymer/Li cells, Electrochim. Acta. 51 (2006) 5334–5340. doi:10.1016/j.electacta.2006.02.004.

[132] W. Hua, W. Liu, M. Chen, S. Indris, Z. Zheng, X. Guo, M. Bruns, T.-H. Wu, Y. Chen, B. Zhong, S. Chou, Y.-M. Kang, H. Ehrenberg, Unravelling the growth mechanism of hierarchically structured $Ni_{1/3}Co_{1/3}Mn_{1/3}(OH)_2$ and their application as precursors for high-power cathode materials, Electrochim. Acta. 232 (2017) 123–131. doi:http://dx.doi.org/10.1016/j.electacta.2017.02.105.

[133] M. Keller, G. B. Appetecchi, G. Kim, V. Sharova, M. Schneider, J. Schuhmacher, A. Roters, S. Passerini, Electrochemical performance of a solvent-free hybrid ceramic-polymer electrolyte based on $Li_7La_3Zr_2O_{12}$ in $P(EO)_{15}$LiTFSI, J. Power Sources. 353 (2017) 287–297. doi:https://doi.org/10.1016/j.jpowsour.2017.04.014.

[134] T. Yang, J. Zheng, Q. Cheng, Y.-Y. Hu, C.K. Chan, Composite Polymer Electrolytes with $Li_7La_3Zr_2O_{12}$ Garnet-Type Nanowires as Ceramic Fillers: Mechanism of Conductivity Enhancement and Role of Doping and Morphology, ACS Appl. Mater. Interfaces. 9 (2017) 21773–21780. doi:10.1021/acsami.7b03806.

[135] J. Zheng, H. Dang, X. Feng, P.-H. Chien, Y.-Y. Hu, Li-ion transport in a representative ceramic–polymer–plasticizer composite electrolyte: $Li_7La_3Zr_2O_{12}$–polyethylene oxide–tetraethylene glycol dimethyl ether, J. Mater. Chem. A. 5 (2017) 18457–18463. doi:10.1039/C7TA05832B.

[136] P.A.R.. Jayathilaka, M.A.K.. Dissanayake, I. Albinsson, B.-E. Mellander, Effect of nano-porous Al_2O_3 on thermal, dielectric and transport properties of the $(PEO)_9$LiTFSI polymer electrolyte system, Electrochim. Acta. 47 (2002) 3257–3268. doi:10.1016/S0013-4686(02)00243-8.

[137] Myer Kutz, Applied Plastics Engineering Handbook: Processing, Materials, and Applications, 2011.

[138] S. Yu, R.D. Schmidt, R. Garcia-Mendez, E. Herbert, N.J. Dudney, J.B. Wolfenstine, J. Sakamoto, D.J. Siegel, Elastic Properties of the Solid Electrolyte $Li_7La_3Zr_2O_{12}$ (LLZO), Chem. Mater. 28 (2016) 197–206. doi:10.1021/acs.chemmater.5b03854.

[139] I. Morphological, E. Properties, C.R. Casaccia, S.M. Galeria, Characterization of PEO-Based Composite Cathodes, J. Electrochem. Soc. 147 (2000) 451–459. doi:10.1149/1.1646148.

[140] P. Buvana, K. Vishista, D. Shanmukaraj, R. Murugan, Lithium garnet oxide dispersed polymer composite membrane for rechargeable lithium batteries, Ionics (Kiel). 23 (2017) 541–548. doi:10.1007/s11581-016-1830-y.

[141] T. Yang, J. Zheng, Q. Cheng, Y.-Y. Hu, C.K. Chan, Composite Polymer Electrolytes with $Li_7La_3Zr_2O_{12}$ Garnet-Type Nanowires as Ceramic Fillers: Mechanism of Conductivity Enhancement and Role of Doping and Morphology, ACS Appl. Mater. Interfaces. 9 (2017) 21773–21780. doi:10.1021/acsami.7b03806.

[142] P.J. Kumar, K. Nishimura, M. Senna, A. Düvel, P. Heitjans, T. Kawaguchi, N. Sakamoto, N.

Wakiya, H. Suzuki, A novel low-temperature solid-state route for nanostructured cubic garnet $Li_7La_3Zr_2O_{12}$ and its application to Li-ion battery, RSC Adv. 6 (2016) 62656–62667. doi:10.1039/C6RA09695F.

[143] B.K. Choi, Y.W. Kim, Thermal history effects on the ionic conductivity of PEO-salt electrolytes, Mater. Sci. Eng. B. 107 (2004) 244–250. doi:http://dx.doi.org/10.1016/j.mseb.2003.09.047.

[144] F. Croce, G.B. Appetecchi, L. Persi, B. Scrosati, Nanocomposite polymer electrolytes for lithium batteries, Nature. 394 (1998) 456–458. doi:10.1038/28818.

[145] D. Wang, G. Zhong, W.K. Pang, Z. Guo, Y. Li, M.J. McDonald, R. Fu, J.X. Mi, Y. Yang, Toward Understanding the Lithium Transport Mechanism in Garnet-type Solid Electrolytes: Li^+ Ion Exchanges and Their Mobility at Octahedral/Tetrahedral Sites, Chem. Mater. 27 (2015) 6650–6659. doi:10.1021/acs.chemmater.5b02429.

[146] M. Galiński, A. Lewandowski, I. Stepniak, Ionic liquids as electrolytes, Electrochim. Acta. 51 (2006) 5567–5580. doi:10.1016/j.electacta.2006.03.016.

[147] Z. Xue, D. He, X. Xie, Poly(ethylene oxide)-based electrolytes for lithium-ion batteries, J. Mater. Chem. A. 3 (2015) 19218–19253. doi:10.1039/C5TA03471J.

[148] J. Zheng, Y.Y. Hu, New Insights into the Compositional Dependence of Li-Ion Transport in Polymer-Ceramic Composite Electrolytes, ACS Appl. Mater. Interfaces. 10 (2018) 4113–4120. doi:10.1021/acsami.7b17301.

[149] S. Chen, Y. Zhao, J. Yang, L. Yao, X. Xu, Hybrid solid electrolytes with excellent electrochemical properties and their applications in all-solid-state cells, Ionics (Kiel). 23 (2017) 2603–2611. doi:10.1007/s11581-016-1905-9.

[150] F. Chen, D. Yang, W. Zha, B. Zhu, Y. Zhang, J. Li, Y. Gu, Q. Shen, L. Zhang, D.R. Sadoway, Solid polymer electrolytes incorporating cubic $Li_7La_3Zr_2O_{12}$ for all-solid-state lithium rechargeable batteries, Electrochim. Acta. 258 (2017) 1106–1114. doi:10.1016/j.electacta.2017.11.164.

[151] J. Rolland, J. Brassinne, J.-P. Bourgeois, E. Poggi, A. Vlad, J.-F. Gohy, Chemically anchored liquid-PEO based block copolymer electrolytes for solid-state lithium-ion batteries, J. Mater. Chem. A. 2 (2014) 11839–11846. doi:10.1039/C4TA02327G.

[152] L. Yang, Z. Wang, Y. Feng, R. Tan, Y. Zuo, R. Gao, Y. Zhao, L. Han, Z. Wang, F. Pan, Flexible Composite Solid Electrolyte Facilitating Highly Stable "Soft Contacting" Li-Electrolyte Interface for Solid State Lithium-Ion Batteries, Adv. Energy Mater. 7 (2017) 1701437. doi:10.1002/aenm.201701437.

[153] G. Bieker, M. Winter, P. Bieker, Electrochemical in situ investigations of SEI and dendrite formation on the lithium metal anode, Phys. Chem. Chem. Phys. 17 (2015) 8670–8679. doi:10.1039/C4CP05865H.

[154] C.-Z. Zhao, X.-Q. Zhang, X.-B. Cheng, R. Zhang, R. Xu, P.-Y. Chen, H.-J. Peng, J.-Q. Huang, Q. Zhang, An anion-immobilized composite electrolyte for dendrite-free lithium metal anodes,

Proc. Natl. Acad. Sci. 114 (2017) 11069–11074. doi:10.1073/pnas.1708489114.

[155] W. Zhou, S. Wang, Y. Li, S. Xin, A. Manthiram, J.B. Goodenough, Plating a Dendrite-Free Lithium Anode with a Polymer/Ceramic/Polymer Sandwich Electrolyte, J. Am. Chem. Soc. 138 (2016) 9385–9388. doi:10.1021/jacs.6b05341.

[156] G. Tan, F. Wu, C. Zhan, J. Wang, D. Mu, J. Lu, K. Amine, Solid-State Li-Ion Batteries Using Fast, Stable, Glassy Nanocomposite Electrolytes for Good Safety and Long Cycle-Life, Nano Lett. 16 (2016) 1960–1968. doi:10.1021/acs.nanolett.5b05234.

[157] W. Cho, S.-M. Kim, J.H. Song, T. Yim, S.-G. Woo, K.-W. Lee, J.-S. Kim, Y.-J. Kim, Improved electrochemical and thermal properties of nickel rich $LiNi_{0.6}Co_{0.2}Mn_{0.}2O_2$ cathode materials by SiO_2 coating, J. Power Sources. 282 (2015) 45–50. doi:10.1016/j.jpowsour.2014.12.128.

[158] F. Langer, I. Bardenhagen, J. Glenneberg, R. Kun, Microstructure and temperature dependent lithium ion transport of ceramic–polymer composite electrolyte for solid-state lithium ion batteries based on garnet-type $Li_7La_3Zr_2O_{12}$, Solid State Ionics. 291 (2016) 8–13. doi:10.1016/j.ssi.2016.04.014.

[159] M. Matsui, K. Takahashi, K. Sakamoto, A. Hirano, Y. Takeda, O. Yamamoto, N. Imanishi, Phase stability of a garnet-type lithium ion conductor $Li_7La_3Zr_2O_{12}$, Dalt. Trans. 43 (2014) 1019–1024. doi:10.1039/C3DT52024B.

[160] C.H. Park, D.W. Kim, J. Prakash, Y.K. Sun, Electrochemical stability and conductivity enhancement of composite polymer electrolytes, Solid State Ionics. 159 (2003) 111–119. doi:10.1016/S0167-2738(03)00025-0.

[161] F. Lian, H. yan Guan, Y. Wen, X. rong Pan, Polyvinyl formal based single-ion conductor membranes as polymer electrolytes for lithium ion batteries, J. Memb. Sci. 469 (2014) 67–72. doi:10.1016/j.memsci.2014.05.065.

[162] Y. Zhang, Y. Zhao, D. Gosselink, P. Chen, Synthesis of poly(ethylene-oxide)/nanoclay solid polymer electrolyte for all solid-state lithium/sulfur battery, Ionics (Kiel). 21 (2014) 381–385. doi:10.1007/s11581-014-1176-2.

[163] L. Porcarelli, C. Gerbaldi, F. Bella, J.R. Nair, Super Soft All-Ethylene Oxide Polymer Electrolyte for Safe All-Solid Lithium Batteries, Sci. Rep. 6 (2016) 19892. doi:10.1038/srep19892.

[164] R. Na, C. Su, Y. Su, Y. Chen, Y. Chen, G. Wang, H. Teng, Solvent-free synthesis of an ionic liquid integrated ether-abundant polymer as a solid electrolyte for flexible electric double-layer capacitors, J. Mater. Chem. A. 5 (2017) 19703–19713. doi:10.1039/C7TA05358D.

[165] X.-X. Zeng, Y.-X. Yin, N.-W. Li, W.-C. Du, Y.-G. Guo, L.-J. Wan, Reshaping Lithium Plating/Stripping Behavior via Bifunctional Polymer Electrolyte for Room-Temperature Solid Li Metal Batteries, J. Am. Chem. Soc. 138 (2016) 15825–15828. doi:10.1021/jacs.6b10088.

[166] S.-H. Wang, S.-S. Hou, P.-L. Kuo, H. Teng, Poly(ethylene oxide)-co-Poly(propylene oxide)-Based Gel Electrolyte with High Ionic Conductivity and Mechanical Integrity for Lithium-Ion

Batteries, ACS Appl. Mater. Interfaces. 5 (2013) 8477–8485. doi:10.1021/am4019115.

[167] C. Liu, K. Rui, C. Shen, M.E. Badding, G. Zhang, Z. Wen, Reversible ion exchange and structural stability of garnet-type Nb-doped $Li_7La_3Zr_2O_{12}$ in water for applications in lithium batteries, J. Power Sources. 282 (2015) 286–293. doi:10.1016/j.jpowsour.2015.02.050.

[168] W. Zhang, J. Nie, F. Li, Z.L. Wang, C. Sun, A durable and safe solid-state lithium battery with a hybrid electrolyte membrane, Nano Energy. 45 (2018) 413–419. doi.org/10.1016/j.nanoen.2018.01.028.

[169] C. Tao, M.-H. Gao, B.-H. Yin, B. Li, Y.-P. Huang, G. Xu, J.-J. Bao, A promising TPU/PEO blend polymer electrolyte for all-solid-state lithium ion batteries, Electrochim. Acta. 257 (2017) 31–39. doi:10.1016/j.electacta.2017.10.037.

[170] B. Scrosati, F. Croce, L. Persi, Impedance Spectroscopy Study of PEO-Based Nanocomposite Polymer Electrolytes, J. Electrochem. Soc. 147 (2000) 1718. doi:10.1149/1.1393423.

[171] N. Nitta, F. Wu, J.T. Lee, G. Yushin, Li-ion battery materials: present and future, Mater. Today. 18 (2015) 252–264. doi:10.1016/j.mattod.2014.10.040.

[172] Q. Zhang, S.-Z. Huang, J. Jin, J. Liu, Y. Li, H.-E. Wang, L.-H. Chen, B.-J. Wang, B.-L. Su, Engineering 3D bicontinuous hierarchically macro-mesoporous $LiFePO_4$/C nanocomposite for lithium storage with high rate capability and long cycle stability, Sci. Rep. 6 (2016) 25942. doi:10.1038/srep25942.

[173] F. Wu, N. Chen, R. Chen, Q. Zhu, J. Qian, L. Li, "Liquid-in-Solid" and "solid-in-Liquid" Electrolytes with High Rate Capacity and Long Cycling Life for Lithium-Ion Batteries, Chem. Mater. 28 (2016) 848–856. doi:10.1021/acs.chemmater.5b04278.

[174] D. Zhou, R. Liu, Y.-B. He, F. Li, M. Liu, B. Li, Q.-H. Yang, Q. Cai, F. Kang, SiO_2 Hollow Nanosphere-Based Composite Solid Electrolyte for Lithium Metal Batteries to Suppress Lithium Dendrite Growth and Enhance Cycle Life, Adv. Energy Mater. 6 (2016) 1502214. doi:10.1002/aenm.201502214.

[175] H. Duan, Y.-X. Yin, X.-X. Zeng, J.-Y. Li, J.-L. Shi, Y. Shi, R. Wen, Y.-G. Guo, L.-J. Wan, In-situ plasticized polymer electrolyte with double-network for flexible solid-state lithium-metal batteries, Energy Storage Mater. 10 (2018) 85–91. doi:10.1016/j.ensm.2017.06.017.

[176] Y. Ma, L.B. Li, G.X. Gao, X.Y. Yang, Y. You, Effect of montmorillonite on the ionic conductivity and electrochemical properties of a composite solid polymer electrolyte based on polyvinylidenedifluoride/polyvinyl alcohol matrix for lithium ion batteries, Electrochim. Acta. 187 (2016) 535–542. doi:10.1016/j.electacta.2015.11.099.

[177] Z. Zhu, M. Hong, D. Guo, J. Shi, Z. Tao, J. Chen, All-Solid-State Lithium Organic Battery with Composite Polymer Electrolyte and Pillar[5]quinone Cathode, J. Am. Chem. Soc. 136 (2014) 16461–16464. doi:10.1021/ja507852t.

[178] K. Kimura, M. Yajima, Y. Tominaga, A highly-concentrated poly(ethylene carbonate)-based electrolyte for all-solid-state Li battery working at room temperature, Electrochem. Commun.

66 (2016) 46–48. doi:10.1016/j.elecom.2016.02.022.

[179] R. Tan, R. Gao, Y. Zhao, M. Zhang, J. Xu, J. Yang, F. Pan, Novel Organic–Inorganic Hybrid Electrolyte to Enable $LiFePO_4$ Quasi-Solid-State Li-Ion Batteries Performed Highly around Room Temperature, ACS Appl. Mater. Interfaces. 8 (2016) 31273–31280. doi:10.1021/acsami.6b09008.

[180] H. Choi, H.W. Kim, J.-K. Ki, Y.J. Lim, Y. Kim, J.-H. Ahn, Nanocomposite quasi-solid-state electrolyte for high-safety lithium batteries, Nano Res. 10 (2017) 3092–3102. doi:10.1007/s12274-017-1526-2.

[181] J.R. Nair, D. Cíntora-Juárez, C. Pérez-Vicente, J.L. Tirado, S. Ahmad, C. Gerbaldi, Truly quasi-solid-state lithium cells utilizing carbonate free polymer electrolytes on engineered $LiFePO_4$, Electrochim. Acta. 199 (2016) 172–179. doi:10.1016/j.electacta.2016.03.156.

[182] D. Zhou, Y. He, R. Liu, M. Liu, H. Du, B. Li, Q. Cai, Q.-H. Yang, F. Kang, In Situ Synthesis of a Hierarchical All-Solid-State Electrolyte Based on Nitrile Materials for High-Performance Lithium-Ion Batteries, Adv. Energy Mater. 5 (2015) 1500353. doi:10.1002/aenm.201500353.

[183] D. Rettenwander, P. Blaha, R. Laskowski, K. Schwarz, P. Bottke, M. Wilkening, C. a. Geiger, G. Amthauer, DFT Study of the Role of Al^{3+} in the Fast Ion-Conductor $Li_{7-3x}Al_{3+x}La_3Zr_2O_{12}$ Garnet, Chem. Mater. 26 (2014) 2617–2623. doi:10.1021/cm5000999.

[184] Y. Li, J.-T. Han, C.-A. Wang, H. Xie, J.B. Goodenough, Optimizing Li^+ conductivity in a garnet framework, J. Mater. Chem. 22 (2012) 15357. doi:10.1039/c2jm31413d.

[185] N. Bernstein, M.D. Johannes, K. Hoang, Origin of the Structural Phase Transition in $Li_7La_3Zr_2O_{12}$, Phys. Rev. Lett. 109 (2012) 205702. doi:10.1103/PhysRevLett.109.205702.

[186] Y. Zhang, F. Chen, R. Tu, Q. Shen, X. Zhang, L. Zhang, Effect of lithium ion concentration on the microstructure evolution and its association with the ionic conductivity of cubic garnet-type nominal $Li_7Al_{0.25}La_3Zr_2O_{12}$ solid electrolytes, Solid State Ionics. 284 (2016) 53–60. doi:10.1016/j.ssi.2015.11.014.

[187] S. Afyon, F. Krumeich, J.L.M. Rupp, 07. A shortcut to garnet-type fast Li-ion conductors for all-solid state batteries, J. Mater. Chem. A. 3 (2015) 18636–18648. doi:10.1039/C5TA03239C.

[188] D. Rettenwander, C.A. Geiger, M. Tribus, P. Tropper, R. Wagner, G. Tippelt, W. Lottermoser, G. Amthauer, The solubility and site preference of Fe^{3+} in $Li_{7-3x}Fe_xLa_3Zr_2O_{12}$ garnets, J. Solid State Chem. 230 (2015) 266–271. doi:10.1016/j.jssc.2015.01.016.

[189] A.A. Trofimov, C. Li, K.S. Brinkman, L.G. Jacobsohn, Luminescence investigation of Ce incorporation in garnet-type $Li_7La_3Zr_2O_{12}$, Opt. Mater. (Amst). 68 (2017) 7–10. doi:10.1016/j.optmat.2016.09.058.

[190] L.J. Miara, W.D. Richards, Y.E. Wang, G. Ceder, First-Principles Studies on Cation Dopants and Electrolyte|Cathode Interphases for Lithium Garnets, Chem. Mater. 27 (2015) 4040–4047. doi:10.1021/acs.chemmater.5b01023.

[191] M. Bitzer, T. Van Gestel, S. Uhlenbruck, Hans-Peter-Buchkremer, Sol-gel synthesis of thin solid $Li_7La_3Zr_2O_{12}$ electrolyte films for Li-ion batteries, Thin Solid Films. 615 (2016) 128–134. doi:10.1016/j.tsf.2016.07.010.

[192] R. Wagner, D. Rettenwander, G.J. Redhammer, G. Tippelt, G. Sabathi, M.E. Musso, B. Stanje, M. Wilkening, E. Suard, G. Amthauer, Synthesis, Crystal Structure, and Stability of Cubic $Li_{7-x}La_3Zr_{2-x}Bi_xO_{12}$, Inorg. Chem. 55 (2016) 12211–12219. doi:10.1021/acs.inorgchem.6b01825.

[193] M. Huang, A. Dumon, C.-W. Nan, Effect of Si, In and Ge doping on high ionic conductivity of $Li_7La_3Zr_2O_{12}$, Electrochem. Commun. 21 (2012) 62–64. doi:10.1016/j.elecom.2012.04.032.

[194] C. Shao, Z. Yu, H. Liu, Z. Zheng, N. Sun, C. Diao, Enhanced ionic conductivity of titanium doped $Li_7La_3Zr_2O_{12}$ solid electrolyte, Electrochim. Acta. 225 (2017) 345–349. doi:10.1016/j.electacta.2016.12.140.

[195] B. Yan, M. Kotobuki, J. Liu, Ruthenium doped cubic-garnet structured solid electrolyte $Li_7La_3Zr_{2-x}Ru_xO_{12}$, Mater. Technol. 31 (2016) 623–627. doi:10.1080/10667857.2016.1196033.

[196] Z.-Z. CAO, W. REN, J.-R. LIU, G.-R. LI, Y.-F. GAO, M.-H. FANG, W.-Y. HE, Microstructure and Ionic Conductivity of Sb-doped Li7La3Zr2O12 Ceramics, J. Inorg. Mater. 29 (2014) 220–224. doi:10.3724/SP.J.1077.2013.13428.

[197] S. Ohta, T. Kobayashi, T. Asaoka, High lithium ionic conductivity in the garnet-type oxide $Li_{7-X}La_3(Zr_{2-X},Nb_X)O_{12}$ (X=0–2), J. Power Sources. 196 (2011) 3342–3345. doi:10.1016/j.jpowsour.2010.11.089.

[198] D. Rettenwander, A. Welzl, L. Cheng, J. Fleig, M. Musso, E. Suard, M.M. Doeff, G.J. Redhammer, G. Amthauer, Synthesis, Crystal Chemistry, and Electrochemical Properties of $Li_{7-2x}La_3Zr_{2-x}Mo_xO_{12}$ (x=0.1–0.4): Stabilization of the Cubic Garnet Polymorph via Substitution of Zr^{4+} by Mo^{6+}, Inorg. Chem. 54 (2015) 10440–10449. doi:10.1021/acs.inorgchem.5b01895.

[199] Y. Li, Z. Wang, Y. Cao, F. Du, C. Chen, Z. Cui, X. Guo, W-Doped $Li_7La_3Zr_2O_{12}$ Ceramic Electrolytes for Solid State Li-ion Batteries, Electrochim. Acta. 180 (2015) 37–42. doi:10.1016/j.electacta.2015.08.046.

[200] R. Jalem, M.J.D. Rushton, W. Manalastas, M. Nakayama, T. Kasuga, J.A. Kilner, R.W. Grimes, Effects of Gallium Doping in Garnet-Type $Li_7La_3Zr_2O_{12}$ Solid Electrolytes, Chem. Mater. 27 (2015) 2821–2831. doi:10.1021/cm5045122.

[201] J. Wolfenstine, J. Ratchford, E. Rangasamy, J. Sakamoto, J.L. Allen, Synthesis and high Li-ion conductivity of Ga-stabilized cubic $Li_7La_3Zr_2O_{12}$, Mater. Chem. Phys. 134 (2012) 571–575. doi:10.1016/j.matchemphys.2012.03.054.

[202] H. El Shinawi, J. Janek, Stabilization of cubic lithium-stuffed garnets of the type "$Li_7La_3Zr_2O_{12}$" by addition of gallium, J. Power Sources. 225 (2013) 13–19. doi:10.1016/j.jpowsour.2012.09.111.

[203] R. Wagner, G.J. Redhammer, D. Rettenwander, G. Tippelt, A. Welzl, S. Taibl, J. Fleig, A. Franz, W. Lottermoser, G. Amthauer, Fast Li-Ion-Conducting Garnet-Related $Li_{7-3x}Fe_xLa_3Zr_2O_{12}$ with

Uncommon $I\bar{4}3d$ Structure, Chem. Mater. 28 (2016) 5943–5951. doi:10.1021/acs.chemmater.6b02516.

[204] Y. Chen, E. Rangasamy, C. Liang, K. An, Origin of High Li^+ Conduction in Doped $Li^7La^3Zr^2O^{12}$ Garnets, Chem. Mater. 27 (2015) 5491–5494. doi:10.1021/acs.chemmater.5b02521.

[205] R. Inada, S. Yasuda, M. Tojo, K. Tsuritani, T. Tojo, Y. Sakurai, Development of Lithium-Stuffed Garnet-Type Oxide Solid Electrolytes with High Ionic Conductivity for Application to All-Solid-State Batteries, Front. Energy Res. 4 (2016) 1–12. doi:10.3389/fenrg.2016.00028.

[206] V. Thangadurai, D. Pinzaru, S. Narayanan, A.K. Baral, Fast Solid-State Li Ion Conducting Garnet-Type Structure Metal Oxides for Energy Storage, J. Phys. Chem. Lett. 6 (2015) 292–299. doi:10.1021/jz501828v.

[207] K. Takada, N. Ohta, Y. Tateyama, Recent Progress in Interfacial Nanoarchitectonics in Solid-State Batteries, J. Inorg. Organomet. Polym. Mater. 25 (2015) 205–213. doi:10.1007/s10904-014-0127-8.

[208] Y. Li, B. Xu, H. Xu, H. Duan, X. L??, S. Xin, W. Zhou, L. Xue, G. Fu, A. Manthiram, J.B. Goodenough, Hybrid Polymer/Garnet Electrolyte with a Small Interfacial Resistance for Lithium-Ion Batteries, Angew. Chemie-Int. Ed. 56 (2017) 753–756. doi:10.1002/anie.201608924.

[209] H. Duan, Y.-X. Yin, Y. Shi, P.-F. Wang, X.-D. Zhang, C.-P. Yang, J.-L. Shi, R. Wen, Y.-G. Guo, L.-J. Wan, Dendrite-Free Li-Metal Battery Enabled by a Thin Asymmetric Solid Electrolyte with Engineered Layers, J. Am. Chem. Soc. 140 (2018) 82–85. doi:10.1021/jacs.7b10864.

[210] B. Liu, Y. Gong, K. Fu, X. Han, Y. Yao, G. Pastel, C. Yang, H. Xie, E.D. Wachsman, L. Hu, Garnet Solid Electrolyte Protected Li-Metal Batteries, ACS Appl. Mater. Interfaces. 9 (2017) 18809–18815. doi:10.1021/acsami.7b03887.

[211] T. Thompson, J. Wolfenstine, J.L. Allen, M. Johannes, A. Huq, I.N. David, J. Sakamoto, Tetragonal vs. cubic phase stability in Al – free Ta doped $Li_7La_3Zr_2O_{12}$ (LLZO), J. Mater. Chem. A. 2 (2014) 13431–13436. doi:10.1039/c4ta02099e.

[212] F. Tietz, T. Wegener, M.T. Gerhards, M. Giarola, G. Mariotto, Synthesis and Raman micro-spectroscopy investigation of $Li_7La_3Zr_2O_{12}$, Solid State Ionics. 230 (2013) 77–82. doi:10.1016/j.ssi.2012.10.021.

[213] P.M. Kouotou, Z.-Y. Tian, H. Vieker, A. Beyer, A. Gölzhäuser, K. Kohse-Höinghaus, Selective synthesis of α-Fe_2O_3 thin films and effect of the deposition temperature and lattice oxygen on the catalytic combustion of propene, J. Mater. Chem. A. 1 (2013) 10495. doi:10.1039/c3ta11354j.

[214] D. Rettenwander, G. Redhammer, F. Preishuber-Pflügl, L. Cheng, L. Miara, R. Wagner, A. Welzl, E. Suard, M.M. Doeff, M. Wilkening, J. Fleig, G. Amthauer, Structural and Electrochemical Consequences of Al and Ga Cosubstitution in $Li_7La_3Zr_2O_{12}$ Solid Electrolytes,

Chem. Mater. 28 (2016) 2384–2392. doi:10.1021/acs.chemmater.6b00579.

[215] R.D. Shannon, Revised effective ionic radii and systematic studies of interatomic distances in halides and chalcogenides, Acta Crystallogr. Sect. A. 32 (1976) 751–767. doi:10.1107/S0567739476001551.

[216] L. Sangaletti, L.E. Depero, B. Allieri, P. Nunziante, E. Traversa, An X-ray study of the trimetallic $La_xSm_{1-x}FeO_3$ orthoferrites, J. Eur. Ceram. Soc. 21 (2001) 719–726. doi:10.1016/S0955-2219(00)00267-3.

[217] J. Fergus, X. Zhang, Processing of Aluminum-Doped Lithium Lanthanum Zirconate Garnet-Type Solid Electrolyte Materials, ECS Trans. 73 (2016) 179–182. doi:10.1149/07301.0179ecst.

[218] X. Huang, C. Shen, K. Rui, J. Jin, M. Wu, X. Wu, Z. Wen, Influence of $La_2Zr_2O_7$ Additive on Densification and Li^+ Conductivity for Ta-Doped $Li_7La_3Zr_2O_{12}$ Garnet, JOM. 68 (2016) 2593–2600. doi:10.1007/s11837-016-2065-0.

[219] J. Awaka, A. Takashima, K. Kataoka, N. Kijima, Y. Idemoto, J. Akimoto, Crystal Structure of Fast Lithium-ion-conducting Cubic $Li_7La_3Zr_2O_{12}$, Chem. Lett. 40 (2011) 60–62. doi:10.1246/cl.2011.60.

[220] H. Xie, C. Yang, K. (Kelvin) Fu, Y. Yao, F. Jiang, E. Hitz, B. Liu, S. Wang, L. Hu, Flexible, Scalable, and Highly Conductive Garnet-Polymer Solid Electrolyte Templated by Bacterial Cellulose, Adv. Energy Mater. 8 (2018) 1703474. doi:10.1002/aenm.201703474.

[221] K. Kataoka, H. Nagata, J. Akimoto, Lithium-ion conducting oxide single crystal as solid electrolyte for advanced lithium battery application, Sci. Rep. 8 (2018) 9965. doi:10.1038/s41598-018-27851-x.

[222] M. Huang, T. Liu, Y. Deng, H. Geng, Y. Shen, Y. Lin, C.-W. Nan, Effect of sintering temperature on structure and ionic conductivity of $Li_{7-x}La_3Zr_2O1_{2-0.5x}$ (x=0.5~0.7) ceramics, Solid State Ionics. 204–205 (2011) 41–45. doi:10.1016/j.ssi.2011.10.003.

[223] C. Shao, H. Liu, Z. Yu, Z. Zheng, N. Sun, C. Diao, Structure and ionic conductivity of cubic $Li_7La_3Zr_2O_{12}$ solid electrolyte prepared by chemical co-precipitation method, Solid State Ionics. 287 (2016) 13–16. doi:10.1016/j.ssi.2016.01.042.

[224] L. Cheng, J.S. Park, H. Hou, V. Zorba, G. Chen, T. Richardson, J. Cabana, R. Russo, M. Doeff, Effect of microstructure and surface impurity segregation on the electrical and electrochemical properties of dense Al-substituted $Li_7La_3Zr_2O_{12}$, J. Mater. Chem. A. 2 (2014) 172–181. doi:10.1039/C3TA13999A.

[225] G.T. Hitz, E.D. Wachsman, V. Thangadurai, Highly Li-Stuffed Garnet-Type $Li_{7+x}La_3Zr_{2x}Y_xO_{12}$, J. Electrochem. Soc. 160 (2013) A1248–A1255. doi:10.1149/2.088308jes.

[226] F. Du, N. Zhao, Y. Li, C. Chen, Z. Liu, X. Guo, All solid state lithium batteries based on lamellar garnet-type ceramic electrolytes, J. Power Sources. 300 (2015) 24–28. doi:10.1016/j.jpowsour.2015.09.061.

[227] R. Murugan, S. Ramakumar, N. Janani, High conductive yttrium doped $Li_7La_3Zr_2O_{12}$ cubic lithium garnet, Electrochem. Commun. 13 (2011) 1373–1375. doi:10.1016/j.elecom.2011.08.014.

[228] T. Liu, Y. Ren, Y. Shen, S.-X. Zhao, Y. Lin, C.-W. Nan, Achieving high capacity in bulk-type solid-state lithium ion battery based on $Li_{6.75}La_3Zr_{1.75}Ta_{0.25}O_{12}$ electrolyte: Interfacial resistance, J. Power Sources. 324 (2016) 349–357. doi:10.1016/j.jpowsour.2016.05.111.

[229] K. Liu, C.-A. Wang, Garnet-type $Li_{6.4}La_3Zr_{1.4}Ta_{0.6}O_{12}$ thin sheet: Fabrication and application in lithium–hydrogen peroxide semi-fuel cell, Electrochem. Commun. 48 (2014) 147–150. doi:10.1016/j.elecom.2014.09.006.

[230] M. Botros, R. Djenadic, O. Clemens, M. Möller, H. Hahn, Field assisted sintering of fine-grained $Li_{7-3x}La_3Zr_2Al_xO_{12}$ solid electrolyte and the influence of the microstructure on the electrochemical performance, J. Power Sources. 309 (2016) 108–115. doi:10.1016/j.jpowsour.2016.01.086.

[231] X. Zhang, J.W. Fergus, The Fabrication of Garnet-Type $Li_7La_3Zr_2O_{12}$ Solid Electrolyte Materials, ECS Trans. 72 (2016) 133–137. doi: 10.1149/07207.0133ecst.

[232] K. Fu, Y. Gong, G.T. Hitz, D.W. McOwen, Y. Li, S. Xu, Y. Wen, L. Zhang, C. Wang, G. Pastel, J. Dai, B. Liu, H. Xie, Y. Yao, E.D. Wachsman, L. Hu, Three-dimensional bilayer garnet solid electrolyte based high energy density lithium metal-sulfur batteries, Energy Environ. Sci. 10 (2017) 1568–1575. doi:10.1039/c7ee01004d.

[233] L. Dhivya, N. Janani, B. Palanivel, R. Murugan, Li^+ transport properties of W substituted $Li_7La_3Zr_2O_{12}$ cubic lithium garnets, AIP Adv. 3 (2013) 082115. doi:10.1063/1.4818971.

[234] W. Gu, M. Ezbiri, R. Prasada Rao, M. Avdeev, S. Adams, Effects of penta-and trivalent dopants on structure and conductivity of $Li_7La_3Zr_2O_{12}$, Solid State Ionics. 274 (2015) 100–105. doi:10.1016/j.ssi.2015.03.019.

[235] A. Düvel, A. Kuhn, L. Robben, M. Wilkening, P. Heitjans, Mechanosynthesis of Solid Electrolytes: Preparation, Characterization, and Li Ion Transport Properties of Garnet-type Al-doped $Li_7La_3Zr_2O_{12}$ Crystallizing with Cubic Symmetry, J. Phys. Chem. C. 116 (2012) 15192–15202. doi:10.1021/jp301193r.

[236] A. Raskovalov, E.A. Il'ina, B. Antonov, Structure and transport properties of $Li_7La_3Zr_{2-0.75x}Al_xO_{12}$ superionic solid electrolytes, J. Power Sources. 238 (2013) 48–52. doi:10.1016/j.jpowsour.2013.03.049.

[237] D. Rettenwander, J. Langer, W. Schmidt, C. Arrer, K.J. Harris, V. Terskikh, G.R. Goward, M. Wilkening, G. Amthauer, Site Occupation of Ga and Al in Stabilized Cubic $Li_{7-3(x+y)}Ga_xAl_yLa_3Zr_2O_{12}$ Garnets As Deduced from 27 Al and 71 Ga MAS NMR at Ultrahigh Magnetic Fields, Chem. Mater. 27 (2015) 3135–3142. doi:10.1021/acs.chemmater.5b00684.

[238] M.A. Howard, O. Clemens, E. Kendrick, K.S. Knight, D.C. Apperley, P.A. Anderson, P.R. Slater, Effect of Ga incorporation on the structure and Li ion conductivity of $La_3Zr_2Li_7O_{12}$, Dalt.

Trans. 41 (2012) 12048. doi:10.1039/c2dt31318a.

[239] D. Rettenwander, C.A. Geiger, M. Tribus, P. Tropper, G. Amthauer, A Synthesis and Crystal Chemical Study of the Fast Ion Conductor $Li_{7-3x}Ga_xLa_3Zr_2O_{12}$ with x = 0.08 to 0.84, Inorg. Chem. 53 (2014) 6264–6269. doi:10.1021/ic500803h.

[240] L. Buannic, B. Orayech, J.-M. López Del Amo, J. Carrasco, N.A. Katcho, F. Aguesse, W. Manalastas, W. Zhang, J. Kilner, A. Llordés, Dual Substitution Strategy to Enhance Li^+ Ionic Conductivity in $Li_7La_3Zr_2O_{12}$ Solid Electrolyte, Chem. Mater. 29 (2017) 1769–1778. doi:10.1021/acs.chemmater.6b05369.

[241] Y. Xia, L. Ma, H. Lu, X.-P. Wang, Y.-X. Gao, W. Liu, Z. Zhuang, L.-J. Guo, Q.-F. Fang, Preparation and enhancement of ionic conductivity in Al-added garnet-like $Li_{6.8}La_3Zr_{1.8}Bi_{0.2}O_{12}$ lithium ionic electrolyte, Front. Mater. Sci. 9 (2015) 366–372. doi:10.1007/s11706-015-0308-6.

[242] Y.X. Gao, X.P. Wang, H. Lu, L.C. Zhang, L. Ma, Q.F. Fang, Mechanism of lithium ion diffusion in the hexad substituted $Li_7La_3Zr_2O_{12}$ solid electrolytes, Solid State Ionics. 291 (2016) 1–7. doi:10.1016/j.ssi.2016.04.017.

Acknowledgments

I would like to acknowledge my supervisor Prof. Dr. Helmut Ehrenberg, and group leader Dr. Frieder Scheiba, for the chance to the research about this interesting and difficult theme, for the kind help and smart advices in these three years. I also thank them very much for the professional guidance through this thesis. I appreciate the freedom and opportunities in our nice group Energy Storage Systems (IAM-ESS) in KIT.

It is pleasure to acknowledge the generous financial supports in Germany by the China Scholarship Council (No. 201506880029).

I appreciate the scientific support and helpful discussions with my colleagues. This work would be not possible without the support and contribution from my colleagues, I would like to thanks again to the whole team, and especially to:

Almut Kriese (administrative support), Dr. Michael Knapp (beam support), Liuda Mereacre (TGA, FT-IR, Raman), Dr. Lukas Pfaffmann (SEM), Dr. Andy Fiedler (Raman&beer training), Geethu Balachandran (TGA), Lihua Zhu (Raman), Qiang Fu (XRD refinement), Dr. Dominique Moock (experimental support), Florian Sigel (experimental support), Weibo Hua (NCM cathode), Lars Esmezjan (SEM), Dr. Angelina Sarapulova (beam support), Dr. Murat Yavuz (PDF refinement), Bettina Hunzinger (SEM&safety training), Udo Geckle (SEM), Dr. Tatiana Zinkevich (NMR), Vanessa Trouillet (XPS), Dr. Sylvio Indris (Mössbauer), Dr. Müller Marcus (Ion beam polishing), Heinz-Robert Goebel (equipment support), Richard Hans Schneider (IT support), Mayer Marcus (equipment support), Elke Herrmann and Jessica Pfisterer (Germany checking)…

I am also grateful to the technical support from Dr. Venkata Sai Kiran Chakravadhanula from INT-KIT (TEM), Shouliang Nie form ITCP (stress tension test), Martin Etter and Jozef Bednarcik from P02.1 PETRA III, DESY.

I would like to thank my thesis committee members: Prof. Dr. Stefano Passerini, Prof. Dr. Patrick Theato, and Prof. Dr. Rolf Schuster, for all of their guidance and valuable discussion.

Finally, I would like to especially thank douban.fm, my families and my wife Zijian Zhao for their never-ending support, accompany and love whenever I needed. Thank you all again.